

## A CHARA Array Survey of Circumstellar Disks around Nearby Be-type Stars

Y. Touhami<sup>1</sup>, D. R. Gies<sup>1</sup>, G. H. Schaefer<sup>2</sup>, H. A. McAlister<sup>1</sup>, S. T. Ridgway<sup>3</sup>, N. D. Richardson<sup>4</sup>, R. Matson<sup>1</sup>, E. D. Grundstrom<sup>5</sup>, T. A. ten Brummelaar<sup>2</sup>, P. J. Goldfinger<sup>2</sup>,  
L. Sturmann<sup>2</sup>, J. Sturmann<sup>2</sup>, N. H. Turner<sup>2</sup>, C. Farrington<sup>2</sup>

yamina@chara.gsu.edu, gies@chara.gsu.edu, schaefer@chara-array.org,  
hal@chara.gsu.edu, ridgway@noao.edu, richardson@astro.umontreal.ca,  
rmatson@chara.gsu.edu, erika.grundstrom@vanderbilt.edu,  
theo@chara-array.org, pj@chara-array.org, sturmann@chara-array.org,  
judit@chara-array.org, nils@chara-array.org, farrington@chara-array.org

### ABSTRACT

We report on a high angular resolution survey of circumstellar disks around 24 northern sky Be stars. The  $K$ -band continuum survey was made using the CHARA Array long baseline interferometer (baselines of 30 – 331 m). The interferometric visibilities were corrected for the flux contribution of stellar companions in those cases where the Be star is a member of a known binary or multiple system. For those targets with good  $(u, v)$  coverage, we used a four-parameter Gaussian elliptical disk model to fit the visibilities and to determine the axial ratio, position angle,  $K$ -band photospheric flux contribution, and angular diameter of the disk's major axis. For the other targets with relatively limited  $(u, v)$  coverage, we constrained the axial ratio, inclination angle, and/or disk position

---

<sup>1</sup>Center for High Angular Resolution Astronomy, Georgia State University, P.O. Box 3969, Atlanta, GA 30302-3969, USA

<sup>2</sup>The CHARA Array, Mount Wilson Observatory, Mount Wilson, CA 91023, USA

<sup>3</sup>National Optical Astronomy Observatory, P.O. Box 26732, Tucson, AZ 85726-6732, USA

<sup>4</sup>Département de physique and Centre de Recherche en Astrophysique du Québec (CRAQ), Université de Montréal, CP 6128 Succ. A., Centre-Ville, Montréal, Québec H3C 3J7, Canada

<sup>5</sup>Physics and Astronomy Department, Vanderbilt University, 6301 Stevenson Center, Nashville, TN 37235, USA

angle where necessary in order to resolve the degeneracy between possible model solutions. We also made fits of the ultraviolet and infrared spectral energy distributions to estimate the stellar angular diameter and infrared flux excess of each target. The mean ratio of the disk diameter (measured in  $K$ -band emission) to stellar diameter (from SED modeling) is 4.4 among the 14 cases where we reliably resolved the disk emission, a value which is generally lower than the disk size ratio measured in the higher opacity  $H\alpha$  emission line. We estimated the equatorial rotational velocity from the projected rotational velocity and disk inclination for 12 stars, and most of these stars rotate close to or at the critical rotational velocity.

*Subject headings:* stars: emission-line, Be — stars: rotation — circumstellar matter — infrared: stars — instrumentation: interferometers — techniques: high angular resolution

## 1. Introduction

Classical Be stars are non-supergiant, B-type stars that are surrounded by hot gaseous disks. This circumstellar gas is responsible for many observational characteristics such as hydrogen Balmer emission lines, IR flux excess, and short- and long-term flux variability (Porter & Rivinius 2003). Optical and infrared interferometry has become an important tool in characterizing Be stars and their disks (Stee 2011). The first interferometric survey of Be stars was made by Quirrenbach et al. (1997) to resolve the  $H\alpha$  emission in seven Be stars. Their survey showed that the emitting regions are flattened, which is strong observational evidence of a disk-like geometry. Quirrenbach et al. (1997) combined optical interferometry and spectropolarimetry to derive the disk position angle on the sky, and they found good agreement between these techniques. Tycner et al. (2004, 2005, 2006, 2008) used the Navy Precision Optical Interferometer (NPOI) to observe the  $H\alpha$  emission from the disks of seven Be stars. Their observations showed that a direct correlation exists between the disk sizes and the net  $H\alpha$  luminosities.

Infrared observations have begun to reveal the spatial properties of the continuum and line emission of Be star disks. Gies et al. (2007) made the first CHARA Array long-baseline interferometric observations in the  $K$ -band of four bright Be stars,  $\gamma$  Cas,  $\phi$  Per,  $\zeta$  Tau, and  $\kappa$  Dra, and they were able to resolve the disks and to constrain their geometrical and physical properties. Meilland et al. (2007) studied the geometry and kinematics of the Be star  $\kappa$  CMa in the  $Br\gamma$  emission line and in the nearby continuum using the VLTI/AMBER instrument. Meilland et al. (2011) observed the Be binary system  $\delta$  Sco using spectrally-

resolved interferometry with the VLTI/AMBER and CHARA/VEGA instruments. Their observations show that the disk varies in size from 4.8 mas in H $\alpha$ , to 2.9 mas in Br $\gamma$ , and to 2.4 mas in the  $K$ -band continuum. Meilland et al. (2012) completed a survey of eight Be stars with VLTI/AMBER and measured the disk extensions in the Br $\gamma$  line and the nearby continuum. Their study suggests that the disk kinematics are dominated by Keplerian rotation and that the central stars have a mean ratio of angular rotational to critical velocity of  $\Omega_{\text{rot}}/\Omega_{\text{crit}} = 0.95$ . In addition, Meilland et al. (2009) used the VLTI/MIDI instrument to determine the  $N$ -band (10  $\mu\text{m}$ ) disk angular size for seven Be stars.

Interferometry offers us the means to explore Be star disks in large numbers and to begin to understand their properties as a whole. Here we present results from such a survey that we conducted in the  $K$ -band continuum using the CHARA Array long-baseline interferometer. In Section 2, we list our sample stars, present our observational data sets, and describe the data reduction process. In Section 3, we describe a method that we implemented to correct the interferometric measurements for the flux of stellar companions. We discuss in Section 4 the spectral energy distributions and their use in estimating the stellar angular diameter and infrared excesses of Be stars. In Section 5, we present fits of the interferometric visibilities using simple geometrical models, and in Section 6, we discuss the results with a particular comparison of the  $K$ -band and H $\alpha$  disk sizes. Finally, we summarize our results and draw our conclusions in Section 7.

## 2. Observations and Reduction

We selected 24 Be stars as targets for this interferometric survey. The main selection criteria were that the stars are nearby and bright, well within the limiting magnitude of the CHARA Classic tip-tilt servo system ( $V < 11$ ) and the near-IR fringe detector ( $K < 8.5$ ). The selected Be stars had to have declinations north of about  $-15^\circ$  to be accessible with the interferometer at low air-mass values. Furthermore, most of the targets have recently shown hydrogen emission and a near-IR flux excess. We relied particularly on spectrophotometric and H $\alpha$  observations conducted by Tycner et al. (2006), Grundstrom (2007), Gies et al. (2007), and Touhami et al. (2010). The targets and their adopted stellar parameters are presented in Table 1. Columns 1 and 2 list the star names, columns 3 to 5 list the spectral classification from the compilation by Yudin (2001) and the stellar effective temperature  $T_{\text{eff}}$  and gravity  $\log g$  from Frémat et al. (2005) (see their Table 9 “Apparent parameters”). The stars HD 166014 and HD 202904 are not listed by Frémat et al. (2005), so we used the parameters for these two from Grundstrom (2007). Columns 6 and 7 list predictions for the position angle  $PA$  of the projected major axis of the disk that should be  $90^\circ$  different from

the intrinsic polarization angle (McDavid 1999; Yudin 2001) and for  $r$ , the ratio of the minor to major axis sizes according to the estimated stellar inclination from Frémat et al. (2005).

Measuring the instrumental transfer function of the CHARA Array interferometer is performed by observing calibrator stars with known angular sizes before and after each target observation. The calibrator stars are selected to be close to the targets in the sky, unresolved with the interferometer’s largest baseline, and without known spectroscopic or visual binary companions. We collected photometric data on each calibrator star in order to construct their spectral energy distribution (SED) and to determine their angular diameter. The collected *UBVRIJK* photometry (available from Touhami 2012) is transformed into calibrated flux measurements using procedures described by Colina et al. (1996) and Cohen et al. (2003). The stellar effective temperature  $T_{\text{eff}}$  and the gravity  $\log g$  (generally from the compilation of Soubiran et al. 2010) are used to produce a model flux distribution that is based on Kurucz stellar atmosphere models. Note that we generally used Johnson  $U$  magnitudes compiled by Karataş & Schuster (2006) and  $B, V$  magnitudes from Ammons et al. (2006), who list Tycho  $B$  and  $V$  magnitudes that are slightly different from Johnson  $B, V$  magnitudes. The photographic  $R$  and  $I$  magnitudes were collected from Monet et al. (2003), which are only slightly different from Johnson  $R, I$  magnitudes. The near-IR  $J, H, K$  photometry was collected from the 2MASS survey (Skrutskie et al. 2006). The use of non-standard photometry introduces errors in the best-fit, limb-darkened angular diameter of the calibrators that are comparable to or smaller than the estimated uncertainties given in Table 2. We also collected measurements of  $E(B - V)$  and applied a reddening correction to the model SED before fitting the SED of the calibrators. We then computed a limb-darkened angular diameter  $\theta_{LD}$  by direct comparison of the observed and model flux distributions. Based upon the limb-darkening coefficients given by Claret (2000), we transformed the limb-darkened angular diameter to an equivalent uniform-disk angular diameter  $\theta_{UD}$  assuming a projected baseline of 300 m.

Columns 1 and 2 of Table 2 list the calibrator star and its corresponding target, respectively, columns 3 and 4 list the calibrator effective temperature  $T_{\text{eff}}$  and reference source, columns 5 and 6 give the surface gravity  $\log g$  and reference source, column 7 gives the spectral classification, and columns 8 and 9 list the adopted interstellar reddening  $E(B - V)$  and the reference source, respectively. Column 10 of Table 2 lists the best-fit limb-darkened angular diameter  $\theta_{LD}$  derived from fitting the calibrator SED, and column 11 lists the corresponding uniform-disk angular diameter  $\theta_{UD}$ .

The observations were conducted between 2007 October and 2010 November using the CHARA Classic beam combiner operating in the  $K$ -band (effective wavelength = 2.1329  $\mu\text{m}$ ; ten Brummelaar et al. 2005). We need a minimum of two interferometer baselines at substantially different projected angles on the sky to map the circumstellar disks around our

targets, and we generally used the South-West baseline of length  $\sim 278$  m oriented at  $39^\circ$  west of north (S1/W1) and the South-East baseline of length  $\sim 330$  m oriented at  $22^\circ$  east of north (S1/E1). Each target and its calibrator were observed throughout a given night in series of 200 scans recorded with a near-IR detector on a single pixel at a frequency that ranged between 500 - 750 Hz, depending on the seeing conditions of each particular night of observation. The interferometric raw visibilities were then estimated by performing an integration of the fringe power spectrum. We used the CHARA Data Reduction Software (ReduceIR; ten Brummelaar et al. 2005) to extract and calibrate the target and the calibrator interferometric visibilities. Then the raw visibilities were calibrated by comparing them to the time-interpolated calibrator visibilities and rescaling them according to the predicted calibrator visibility for the given projected baseline and stellar angular diameter. The resulting calibrated visibilities are listed in Table 3 (given in full in the electronic version). Column 1 of Table 3 lists target HD number, column 2 lists the heliocentric Julian date of mid-observation, column 3 lists the telescope pair used in each observation, columns 4 and 5 list the  $u$  and  $v$  frequencies, respectively, column 6 lists the projected baseline, column 7 lists the effective baseline (see § 5.2), columns 8 and 9 list the calibrated visibility and its corresponding uncertainty, respectively, and lastly, columns 10 and 11 list the visibility measurements and uncertainties corrected for the flux of stellar companions for those cases with known binary parameters. We will discuss this correction in detail in the next section.

The internal uncertainties from fitting individual fringes are generally smaller than  $< 5\%$ . The scatter in the data depends mostly on the target magnitude and seeing conditions at the time of the observations, which usually varies with a Fried parameter in the range  $r_0 \simeq 2.5 - 14$  cm. The visibility uncertainties for the brightest targets range between 2% and 5%, while those for the faintest ones reach up to 8%.

Overall we obtained a relatively good set of observations at different hour angles for each star in our sample, with the exceptions of HD 58715 and HD 148184 where the position angle coverage was limited to only one projected baseline. Figure Set 1 shows the distribution of the observations in the  $(u, v)$  plane for our sample.

### 3. Correction for the Flux of Nearby Companions

#### 3.1. Influence of Binary Companions on Interferometric Measurements

Our measurements of the sizes and orientations of Be star disks are based upon the observed decline in visibility caused by the extended angular distribution of disk flux. However, a drop in visibility can also occur if a stellar companion is within the effective field of view of

the interferometer, and if the binary component is ignored, then the disk dimensions will be overestimated (in the extreme case apparently implying the presence of a large disk where none is present). Binary systems are relatively common among B-stars in general and Be stars in particular (Abt 1987; Mason et al. 1997; Gies 2001), so it is important to investigate what role they play in the interpretation of our interferometric measurements.

Fortunately, the signatures of binary companions in interferometric observations are well understood (Herbison-Evans et al. 1971; Armstrong et al. 1992; Dyck et al. 1995; Boden 2000), and given the projected separation and magnitude difference we can determine how the companion will affect our measurement. According to the van Cittert-Zernicke theorem, the complex visibility is related to the Fourier transform of the angular spatial distribution in the sky, and the measured fringe amplitude is proportional to the real part of the visibility (Dyck et al. 1995; Boden 2000). In the ideal case of a binary star consisting of two point sources, the visibility varies according to a cosinusoidal term with a frequency that depends on the projected separation and the baseline and wavelength of observation. The interferometric fringe observed will display an amplitude that depends on the real part of the visibility according to the projected separation and binary flux ratio. For observations like ours that record the flux over a wide filter band, the fringe pattern is only seen over a range in optical path delay that is related to the coherence length. Binaries with separations smaller than the coherence length will display the full amplitude variation expected from the visibility dependence on binary separation and flux ratio (Boden 2000; Raghavan et al. 2009), while those with separations larger than the coherence length will appear as separated fringe packets (Dyck et al. 1995; O’Brien et al. 2011; Raghavan et al. 2012).

Thus, there are several separation ranges that are key to this discussion. First, we may ignore those binary companions that are outside of the field of view of the interferometer ( $0.8 \times 0.8$  arcsec; §3.6) and separated by more than atmospheric seeing disk. Second, there are binary companions that are effectively within the field of view, but whose projected separations are large enough that the fringe packets of the components do not overlap ( $\gtrsim 9$  mas for an observation with a 300 m baseline). This is by far the most common case for our observations, and indeed the fringe packet of the companion is usually located far beyond the recorded scan. In this situation the flux of the companion will act to dilute the measured visibility of the fringe but will not change its morphology (§3.3). Third, there are binaries that have such small projected separations ( $\lesssim 9$  mas for an observation with a 300 m baseline) that their fringe packets overlap and create an oscillatory pattern in the observed visibility due to the interference between fringe packets (§3.3). This probably occurred in only a few cases among our observations (§3.7).

Ideally, we should model the fringe visibility in terms of the binary projected separation

and flux ratio together with a parametrization of the Be disk properties (§5.1). However, because this is a survey program, our observational results are generally too sparse in coverage of baseline and position angle range to attempt such a general solution. For example, most of the known companions have angular separations that are relatively large, and the fringe packet of a companion would have only been recorded in short baseline observations. However, such short baseline data would not resolve the Be disks, which is our primary scientific goal. There are a few cases where the projected separations are small and the binary creates oscillations in visibility with projected baseline, but again our baseline coverage is generally too sparse to measure these together with the disk properties. Consequently, we made the decision to rely solely on published data on the binary companions of our targets (§3.2) in order to perform the corrections to the measured visibility where it was necessary to do so (i.e., the known companion was sufficiently bright and close enough to influence our visibility measurements).

The visibility correction procedure we adopted is outlined in the following subsections. The method is built upon the scheme described by Dyck et al. (1995) and considers how a binary companion influences the appearance of the combined fringe packets. We use estimates of the flux ratio (§3.5, 3.6) and the orbital projected separation (§3.2) for each observation to build a numerical relation between the Be star visibility and net observed visibility. Then we interpolate within these relations to determine the Be star visibility alone (§3.3). We also extend this approach to correct the visibilities for two multiple star systems (§3.4).

### 3.2. Binary Stars in the Sample

Many Be stars in our sample are known binaries or multiple systems. We checked for evidence of the presence of companions through a literature search with frequent consultation of the Washington Double Star Catalog (Mason et al. 2001), the Fourth Catalog of Interferometric Measurements of Binary Stars (Hartkopf et al. 2001), and the Third Photometric Magnitude Difference Catalog<sup>6</sup>. We only considered those companions close enough to influence the interferometry results (i.e., those with separations less than a few arcsec). We show the binary search results in Table 4, which includes visual binaries (typical periods > 1 y) and spectroscopic binaries (typical periods < 1 y). Columns of Table 4 list the star name, number of components, reference code for speckle interferometric observations, and then in each row, the component designation, orbital period, angular semimajor axis, the

---

<sup>6</sup><http://www.usno.navy.mil/USNO/astrometry/optical-IR-prod/wds/dm3>

estimated  $K$ -band magnitude difference between the components  $\Delta K$ , a Y or N for whether or not a correction for the flux of companions was applied to the data, and a reference code for investigations on each system. Entries appended with a semi-colon in Table 4 indicate parameter values with large uncertainties. These include the single-lined spectroscopic binaries, where we simply assumed a primary mass from the spectral classification and  $1M_{\odot}$  for the companion to derive the semimajor axis  $a$ , which was transformed to an angular semimajor axis using the distance from *Hipparcos* (van Leeuwen 2007).

We find that ten of the 24 Be stars in our sample have no known companion, and five others have companions that are too faint (all single-lined spectroscopic binaries) to influence the interferometric measurements. Thus, no corrected visibilities are listed for these 15 targets in Table 3. However, the companions were bright enough ( $\Delta K < 3.2$ ) and close enough (separation  $< 1''$ ) for the remaining nine targets that we had to implement the corrections method outlined below.

We need to determine the companion’s separation and position angle at the time of each observation in order to find the angular separation projected along the baseline we used. This was done by calculating the binary relative separation for the time of observation from the astrometric orbital parameters using the method outlined by Raghavan et al. (2009). We show in Table 5 the adopted orbital parameters for those binaries where we made visibility corrections. Note that no entry is present for HD 166014, where only one published measurement exists (see Appendix), and we simply assumed that the projected separation was larger than the recorded scan length. There are four cases where we present new orbital elements that are based upon published astrometric measurements, and we caution that these are preliminary and used only to estimate the separations and position angles at the times of the CHARA Array observations. Details about these preliminary fits are given in the Appendix.

### 3.3. Fringe Visibility for Be Stars in Binaries

The changes in visibility caused by a binary companion can be described equivalently in terms of the real part of the complex visibility or the amplitude of interfering fringe packets (Dyck et al. 1995; Boden 2000). Here we develop a fringe packet approach to the problem that simulates the binary changes and that is directly applicable to the fringe amplitudes that we measure. We begin by considering how the fringe patterns of binaries overlap in order to assess the changes in visibility caused by a binary consisting of two unresolved stars, and then we extend the analysis to the situation where one star (Be plus disk) is partially resolved. The fringe packet for star  $i$  observed in an interferometric scan of changing optical



path length has the form

$$F_i = \frac{\sin x}{x} \cos(2\pi \frac{a}{\lambda} + \phi) \quad (1)$$

where  $x = \pi a / \Lambda_{coh}$ ,  $a$  is the scan position relative to the center of the fringe,  $\Lambda_{coh}$  is the coherence length given by  $\lambda^2 / \delta\lambda$  (equal to  $13 \mu\text{m}$  for the CHARA Classic  $K'$  filter), and  $\phi$  is a phase shift introduced by atmospheric fluctuations (O’Brien et al. 2011). If two stars are present in the field of view (§3.6) with a projected separation along the scan vector of  $x_2$ , then their fringe patterns may overlap and change the composite appearance of the fringe according to (Boden 2000)

$$F_{tot} = \frac{1}{1 + f_2/f_1} F_1 + \frac{f_2/f_1}{1 + f_2/f_1} F_2 \quad (2)$$

where  $f_1$  and  $f_2$  are the monochromatic fluxes of the stars. Then the fringe visibility is calculated by

$$V = \frac{\max(F_{tot}) - \min(F_{tot})}{2 + \max(F_{tot}) + \min(F_{tot})}. \quad (3)$$

In this discussion we will ignore the very small decline in fringe amplitude related to the angular diameters of the stars themselves, because their angular diameters are all very small (see Table 6 below).

We show a series of such combined fringe patterns in the panels of Figure 2 for an assumed flux ratio of  $f_2/f_1 = 0.5$ . In the top panel, the projected separation is zero, and the two patterns add to make the fringe pattern of a single unresolved star. The associated visibility that we would measure equals one in this case. However, in the second panel from the top, we show how a projected separation of  $1 \mu\text{m}$  results in a much lower visibility because the peaks associated with star 1 are largely eliminated by the troughs associated with star 2. In the third panel from the top, the separation is just large enough (comparable to the coherence length) that the fringe pattern of the companion emerges from the blend, and the lower panel shows a separated fringe packet in which both fringe patterns are clearly visible. Note that the relationship between the projected angular separation (mas = milli-arcsecond) and the separation of fringe centers ( $\mu\text{m}$ ) is given by

$$\rho_{\text{mas}} = \frac{206.265 \rho_{\mu\text{m}}}{B} \quad (4)$$

where  $B$  is the projected baseline in meters. For instance, using a 330 m baseline, the longest scan length is  $150 \mu\text{m}$ , which corresponds to a separation of  $\sim 94$  mas.

We show in Figure 3 the net visibility that would be measured as a function of projected separation  $x_2$ . This shows that in general the observed visibility will be less than that of a

single star. As expected, for very close separations the visibility varies cosinusoidally with  $x_2$  with a frequency of  $2\pi/\lambda$ . On the other hand, for projected separations larger than the coherence length  $\Lambda_{coh}$ , the visibility approaches the value  $1/(1 + f_2/f_1)$  equal to the semiamplitude of the flux diluted fringe pattern of the target.

Now suppose that star 1 is a Be star with a disk that is partially resolved, so that if it were observed alone, it would show a visibility  $V = V_c < 1$ . Consequently, its fringe pattern would have an semiamplitude given by  $V_c/(1 + f_2/f_1)$ . We show a selection of model binary fringe patterns in Figure 4 again for  $f_2/f_1 = 0.5$  and a specific separation of  $x_2 = 10 \mu\text{m}$ . The panels show from top to bottom the progressive appearance of the combined fringe patterns as  $V_c$  drops from 1 to 0.25. Now the visibility drops in tandem until  $V_c = 0.50$  where the maximum and minimum are set by the fringe pattern of the companion. We show the relationship between the Be star visibility  $V_c$  and the net observed visibility  $V_o$  in Figure 5 (solid line for  $x_2 = 10 \mu\text{m}$ ). At this separation, there is some slight destructive interference between the fringe patterns that decreases the maximum amplitude for star 2, and as  $V_c$  declines to zero, the net visibility attains the amplitude of star 2 alone  $(f_2/f_1)/(1 + f_2/f_1)$ . Figure 5 also shows the  $(V_c, V_o)$  relationship for two other separations. The dotted line shows the case of zero separation for maximum constructive interference, and here the visibility declines linearly to  $(f_2/f_1)/(1 + f_2/f_1)$  as  $V_c$  tends to zero. Finally, the dashed line shows the case for a very large separation in which the fringe pattern of star 2 falls beyond the recorded portion of the scan. Here the visibility starts at its diluted value of  $1/(1 + f_2/f_1)$  at  $V_c = 1$  and declines to near zero at  $V_c = 0$ .

Thus, to correct the observed visibilities for the presence of a companion, we need a diagram like Figure 5 for each observation of a target. We calculated the projected separation of the stars at the time of the observation from the dot product of the relative position vector (from the angular orbital elements given in Table 5) and the  $(u, v)$  spatial frequencies for the baseline used. Then we created an associated  $(V_c, V_o)$  diagram for each observation based upon the projected separation and effective flux ratio. The corrected visibility  $V_c$  was then found by interpolating in the relationship at the observed  $V_o$  value. In some rare circumstances, we encountered a double-valued  $(V_o, V_c)$  relation, so no correction was attempted because of this ambiguity.

### 3.4. Fringe Visibility for Be Stars in Multiple Systems

There are six systems in our sample with two or more close companions. Both companions of HD 5394 ( $\gamma$  Cas) are faint, so no correction was made. In the cases of HD 23862 (Pleione) and HD 200120 (59 Cyg), the inner companion is very faint, so corrections were

made for only the outer, brighter companion. The spectroscopic pair that comprises the B component of HD 4180 (*o* Cas) has such a small angular semimajor axis that it was treated as a single object, and thus this system was also corrected as a binary star (§3.3). This left two systems, HD 198183 (the triple  $\lambda$  Cyg) and HD 217675 (the quadruple *o* And), that required corrections for the flux of additional components. The very close B pair of *o* And was regarded as a single object (see Appendix), so both  $\lambda$  Cyg and *o* And were treated as triple star systems.

We made visibility corrections for these two systems in much the same way as for the binaries, except in this case the fringe normalizations were assigned by

$$F_{tot} = \frac{F_1}{1 + f_2/f_1 + f_3/f_1} + \frac{(f_2/f_1)F_2}{1 + f_2/f_1 + f_3/f_1} + \frac{(f_3/f_1)F_3}{1 + f_2/f_1 + f_3/f_1}. \quad (5)$$

Again, we formed model visibilities from the coaddition of the fringe patterns, determined the  $(V_c, V_o)$  relationships for the time and baseline configuration of each observation, and then used the inverted relation  $(V_o, V_c)$  to determine the corrected visibility.

Unfortunately, there are significant uncertainties surrounding both the magnitude differences and orbital elements for the companions of HD 198183 and HD 217675, and these introduce corresponding uncertainties in the amounts of visibility correction. Our results on these two systems must therefore be regarded as representative visibility solutions rather than definitive ones. However, the corrected interferometry visibilities are all close to one for these two Be stars, which suggests that their disks are only marginally resolved if at all. On the other hand, the much lower uncorrected visibilities of these two show that the influence of the companions is clearly present. Both targets will be important subjects for future, multiple baseline observations with the CHARA Array to determine their orbital properties.

### 3.5. *K*-band Magnitude Difference

Our visibility correction procedure requires a knowledge of both the projected separation of the stars (§3.2) and their monochromatic flux ratio. Unfortunately, the magnitude differences between the Be star primary and the companion are generally available only in the *V*-band, and we need to estimate the magnitude differences in the *K*-band. We must consider the color difference between the components and how much brighter the Be star plus disk appears in the *K*-band compared to the *V*-band. The predicted magnitude difference is given by

$$\Delta K_{\text{obs}} = -2.5 \log_{10} \frac{F_2}{F_1 + F_d} = -2.5 \log_{10} \frac{F_2}{F_1} + 2.5 \log_{10} \left( 1 + \frac{F_d}{F_1} \right) \quad (6)$$

where  $F_2$ ,  $F_1$ ,  $F_d$  are the monochromatic  $K$ -band fluxes for the Be companion, the Be star, and the Be disk, respectively. We can estimate the first term from the color differences of the Be star and companion using

$$\Delta K_{\text{bin}} = -2.5 \log_{10} \frac{F_2}{F_1} = \Delta V_{\text{bin}} + (V - K)_1 - (V - K)_2 \quad (7)$$

where we will assume that the disk contribution is negligible in the  $V$ -band so that  $\Delta V_{\text{bin}} = \Delta V_{\text{obs}}$ . In the absence of other information, we estimated the color differences  $(V - K)$  by assuming that both the Be star and companion are main sequence objects, and we used the relationship between  $(V - K)$  and magnitude difference from a primary star of effective temperature  $T_{\text{eff}}(\text{Be})$  (Frémat et al. 2005) for main sequence stars from Lejeune & Schaerer (2001) to find  $(V - K)$  for both stars.

We determined the infrared flux excess term  $(1 + F_d/F_1)$  from our observed estimate of  $E^*(V^* - K)$  (Touhami et al. 2011), which are related by

$$E^*(V^* - K) = 2.5 \log \frac{F_{\text{tot}}^K}{F_{\text{tot}}^V (F_1^K/F_1^V)} = 2.5 \log_{10} \frac{[1 + F_d/F_1 + F_2/F_1]^K}{[1 + F_d/F_1 + F_2/F_1]^V} \quad (8)$$

where the superscripts indicate the filter band. If we assume that the disk contributes no flux in the  $V$ -band, then we can rearrange this equation to find the  $K$ -band flux excess relative to that of the Be star alone. Then we can combine the results from the two equations above to predict the observed the  $K$ -band magnitude difference

$$\Delta K_{\text{obs}} = \Delta K_{\text{bin}} + E^*(V^* - K) + 2.5 \log_{10} (1 + 10^{-0.4\Delta V_{\text{bin}}} - 10^{-0.4(\Delta K_{\text{bin}} + E^*(V^* - K))}). \quad (9)$$

Our estimates for  $\Delta K_{\text{obs}}$  are listed in Tables 4 and 5. Note that there are several instances where we give a range for the magnitude difference; these are Be stars that are single-lined spectroscopic binaries with a companion of an unknown type. We consider two hypothetical cases. First, we assume that the companion is a main sequence star of one solar mass, and we use the Lejeune & Schaerer (2001) main sequence relation to obtain the magnitude and color differences of the companion. The second case is to assume that the companion is a hot subdwarf (similar to the case of  $\phi$  Per; see Gies et al. 1998) with a typical effective temperature of 30 kK and a stellar radius of  $1R_{\odot}$ . We then estimate  $\Delta K_{\text{obs}}$  by adopting the main sequence radius for the Be star according to its effective temperature and by using the Planck function for both stars in order to estimate the monochromatic  $K$ -band flux ratio. Table 4 lists those cases with a hyphen in the  $\Delta K$  column giving the magnitude difference range between that for a hot subdwarf (smaller) and for a solar-type companion (larger). However, we made no visibility corrections in most of these cases because the nature of the companion is so uncertain (with the exception of  $\phi$  Per where the companion’s spectrum was detected and characterized by Gies et al. 1998).

### 3.6. Seeing and Effective Flux Ratio

The CHARA Classic observations were recorded on a single pixel of the Near Infrared Observer camera (NIRO), and the physical size of the pixel corresponds to a square of dimensions  $0.8 \times 0.8$  arcsec on the sky. The flux of companions with separations small compared to 0.8 arcsec will be more or less completely included in the observations, but the flux of companions with larger separations from the central Be star may be only partially recorded according to the separation and seeing conditions at the time of observation. Therefore, we need to calculate the effective flux ratio of companion to target based upon the relative amounts of flux as recorded by this one pixel.

Seeing is usually computed in real time according to the CHARA tip-tilt measurements of the  $V$ -band flux of the targets. By assuming that the  $K$ -band seeing varies with wavelength by  $\lambda^{-1/5}$  (Young 1974), the  $K$ -band seeing disk is about  $\sim 0.76$  times that in  $V$ . The effective flux ratio is given by

$$f_2/f_1 = I_2/I_1 \quad (10)$$

where  $I_1$  and  $I_2$  are the net intensity contributions of the primary and secondary component, respectively, recorded by the pixel. We assume a Gaussian profile for the point spread function as projected on the detector,

$$I(x, x_0, y, y_0) = \frac{1}{2\pi\sigma^2} \exp \left[ -\frac{1}{2} \frac{(x - x_0)^2 + (y - y_0)^2}{\sigma^2} \right] \quad (11)$$

where  $(x_0, y_0)$  are the coordinates of the central position of the star on the detector chip, and  $\sigma$  is related to the seeing ( $\sigma = 2.355^{-1} \theta_{seeing}$ ). The intensity distributions of the primary and the secondary components integrated over one pixel on the detector are given by

$$I_1 = Q \int \int I(x, 0, y, 0) dx dy \quad (12)$$

$$I_2 = \int \int I(x, 0, y, \rho) dx dy \quad (13)$$

where  $\rho$  is the separation of the binary, and  $Q$  is the actual ratio of primary to secondary flux, which is derived from the magnitude difference of the two components in the  $K$ -band,

$$Q = 10^{0.4 \Delta K_{\text{obs}}}. \quad (14)$$

### 3.7. Visibility Corrections and Their Uncertainties

We used the visibility correction scheme described in §3.3 and 3.4 with the predicted projected angular separation (from the orbital elements in Table 5 and the observed  $(u, v)$  spatial frequencies in Table 3) and the effective flux ratio (§3.5 and 3.6) to derive estimates of the Be star visibility alone. The corrected visibilities and their corresponding uncertainties are listed in the last two columns of Table 3 for the nine cases with significant companions. These uncertainties do not include the contributions to the error budget from uncertainties in projected separation and flux ratio. In most cases the projected separations are much larger than the coherence length (typically 9 to 27 mas for 300 m to 100 m baselines), which corresponds to the separated fringe packet case (see lower panel of Fig. 2). Thus, the correction depends mainly on the flux dilution term,  $1/(1 + f_2/f_1)$ , and typical uncertainties of 0.2 mag for  $\Delta K_{\text{obs}}$  only amount to correction uncertainties of  $\approx 0.02$  in visibility, i.e., generally smaller than the measurement errors. On the other hand, binaries with projected separations less than the coherence length (mainly observations of  $\iota$  Cas and  $\phi$  Per; see Table 5) have corrections that reflect the fringe amplitude oscillation caused by beating between the fringe patterns of the components (Fig. 3). These corrections may amount to  $(f_2/f_1)/(1 + f_2/f_1)$  in visibility,  $\approx 0.10$  for the relatively faint companions considered here. Figure 3 shows that the full range of the correction varies over a projected separation difference of  $\Delta x_2 = \lambda/2$ , which corresponds to a projected angular separation difference of approximately 0.7 to 2.2 mas for 300 m and 100 m baselines, respectively. The predictive accuracy of the orbital separation probably has comparable uncertainties for the cases of  $\iota$  Cas and  $\phi$  Per, so it is possible that the uncertainties in the corrections may be similar to the corrections themselves in these close separation instances. Nevertheless, we found that implementing the corrections even in these close cases tended to reduce the scatter in the fit of the Be disk visibilities (§5.1), so we will adopt the corrected visibilities in the subsequent analysis of all nine targets with significant companions.

## 4. Spectral Energy Distributions

The spectral energy distributions (SEDs) of our sample stars can help us to estimate the photospheric angular diameter of the Be star and the IR flux excess (from a comparison of the observed and extrapolated stellar IR fluxes). The observed IR flux excess can thus be directly compared with the disk flux fraction derived from fits of the visibility measurements. One difficulty with this approach is that the IR flux excess is usually derived assuming that the disk contributes no flux in the optical range, so the stellar SED can be normalized to the optical flux. However, this may lead to an underestimate of the IR excess if the disk

flux emission is significant in the optical, which may be the case for stars with dense and large circumstellar disks. The disk flux fraction declines at lower wavelength because of the drop in free-free opacity, and the disk contribution is negligible in the ultraviolet (UV) part of the spectrum. Therefore, we decided to make fits of the UV flux to set the photospheric flux normalization, which will provide a more reliable estimate of the IR flux excess.

We collected UV spectra for all our targets from the archive of the *International Ultraviolet Explorer (IUE) Satellite*, maintained at the NASA Mikulski Archive for Space Telescopes at STScI<sup>7</sup>. In most cases, we used the available low dispersion, SWP (1150 - 1900 Å) and LWP/LWR (1800 - 3300 Å) spectra, and in cases where there were fewer than two each of these, we used high-dispersion spectra for these two spectral ranges. In the case of HD 217891, all but one of the spectra were made with the small aperture, so we formed an average spectrum and rescaled the flux to that measured by the TD-1 satellite (Thompson et al. 1978). In the case of HD 203467, there were no long-wavelength spectra available in the *IUE* archive, so we used a combination of *IUE* SWP spectra (1150 – 1900 Å), SKYLAB objective-prism spectrophotometry (1900 – 2300 Å; Henize et al. 1979), and OAO-2 spectral scans (2300 – 3200 Å; Meade & Code 1980). Fluxes from each spectrum were averaged into 10 Å bins from 1155 to 3195 Å, and then the fluxes from all the available spectra for a given target were averaged at each point in this wavelength grid.

We created model spectra to compare with the *IUE* observations by interpolating in the grid of model LTE spectra obtained from R. Kurucz. These models were calculated for solar abundances and a microturbulent velocity of 2 km s<sup>-1</sup>. The interpolation was made in effective temperature and gravity using estimates for these parameters (see Table 1) from the Be star compilation of Frémat et al. (2005). For those sample stars in binaries, we formed a composite model spectrum by adding a model spectrum for each companion that was scaled according to the *K*-band magnitude difference listed in Table 5.

We then made a non-linear, least-squares fit of the observed UV spectrum with a model spectrum transformed according to the extinction curve of Fitzpatrick (1999) and normalized by the stellar, limb-darkened angular diameter  $\theta_{LD}$ , and we assumed a standard ratio of total to selective extinction of  $R = 3.1$  for the interstellar extinction curve. Finally, we considered an extension of the fitted photospheric SED into the *K*-band, and we determined an IR flux excess from

$$E^*(UV - K) = 2.5 \log\left(1 + \frac{F_{tot}}{F_1} \frac{F_{obs} - F_{tot}}{F_{tot}}\right) \quad (15)$$

where the monochromatic *K*-band fluxes are  $F_1$  for the Be star component,  $F_{tot}$  for the sum

---

<sup>7</sup><http://archive.stsci.edu/iue/>

of the photospheric fluxes of the Be and all companions (if any), and  $F_{obs}$  is the observed flux from 2MASS (Cohen et al. 2003; Cutri et al. 2003).

Our results are listed in Table 6 that gives the HD number of the star, the derived reddening  $E(B - V)$  and its uncertainty, the limb darkened stellar angular diameter  $\theta_s$  and its uncertainty, and the infrared excess from the disk  $E^*(UV - K)$  and its uncertainty. The final columns list the photospheric fraction of flux  $c_p$  and its uncertainty that are related to the IR flux excess by

$$E^*(UV - K) = -2.5 \log c_p. \quad (16)$$

Our derived interstellar reddening values are generally smaller than those derived from the optical colors because the disk flux contribution increases with increasing wavelength through the optical band which mimics interstellar reddening (Dougherty et al. 1994). Furthermore, our derived angular diameters may be smaller in some cases from previous estimates because of the neglect of the flux of the companions in earlier work. Note that we have neglected the effects of rotation (oblateness and gravity darkening) on the SED, and these may influence the flux normalization (Frémat et al. 2005).

## 5. Gaussian Elliptical Fits

### 5.1. Method

Here we show how we can use the interferometric visibility measurements to estimate the stellar and disk flux contributions and to determine the spatial properties of the disk emission component. We used a two-component geometrical disk model to fit the CHARA Classic observations and to measure the characteristic sizes of the circumstellar disks. The model consists of a small uniform disk representing the central Be star and an elliptical Gaussian component representing the circumstellar disk (Quirrenbach et al. 1997; Tycner et al. 2004). Because the Fourier transform function is additive, the total visibility of the system is the sum of the visibility function of the central star and the disk,

$$V_{tot} = c_p V_s + (1 - c_p) V_d \quad (17)$$

where  $V_{tot}$ ,  $V_s$ , and  $V_d$  are the total, stellar, and disk visibilities, respectively, and  $c_p$  is the ratio of the photospheric flux contribution to the total flux of the system. The visibility for a uniform disk star of angular diameter  $\theta_s$  is

$$V_s = 2J_1(\pi x \theta_s) / (\pi x \theta_s) \quad (18)$$

where  $J_1$  is the first-order Bessel function of the first kind and  $x$  is the spatial frequency of the interferometric observation,  $x = \sqrt{u^2 + v^2}$ . The central Be star is usually mostly



unresolved even at the longest baseline of the interferometer, which brings its visibility close to unity,  $V_s \simeq 1$ . The disk visibility is given by a Gaussian elliptical distribution

$$V_d = \exp \left[ -\frac{(\pi\theta_{\text{maj}}s)^2}{4 \ln 2} \right] \quad (19)$$

where  $\theta_{\text{maj}}$  is the full-width at half-maximum (FWHM) of the spatial Gaussian distribution along the major axis and  $s$  is given by

$$s = \sqrt{r^2(u \cos PA - v \sin PA)^2 + (u \sin PA + v \cos PA)^2} \quad (20)$$

where  $r$  is the axial ratio and  $PA$  is the position angle of the disk major axis. Thus, the Gaussian elliptical model has four free parameters: the photospheric contribution  $c_p$ , the axial ratio  $r$ , the position angle  $PA$ , and the disk angular size  $\theta_{\text{maj}}$ .

## 5.2. The Effective Baseline

The brightness distribution of the disk projected onto the sky is a function of the inclination and position angle of the major axis. Interferometric observations with a given baseline  $B_p$  will sample the disk elliptical distribution according to the angle between the projection of the baseline on the sky and the position angle of the disk major axis. It is helpful to consider rescaling the baseline to account for the changes in the disk size with direction. For a flat disk inclined by an angle  $i$  and oriented with the major axis at a position angle  $PA$  (measured from north to east), we can rescale using the effective baseline  $B_{\text{eff}}$  (Tannirkulam et al. 2008)

$$B_{\text{eff}} = B_p \sqrt{\cos^2(\phi_{\text{obs}} - PA) + \cos^2 i \sin^2(\phi_{\text{obs}} - PA)} \quad (21)$$

where  $\phi_{\text{obs}}$  is the baseline position angle at the time of the observations. This new quantity, the effective baseline, takes into consideration the decrease in the interferometric resolution due to the inclination of the disk in the sky, and thus for the purposes of analysis, it transforms the projected brightness distribution of the disk into a nearly circularly symmetric brightness distribution. Thus, the disk part of the visibility can be considered as a function of  $B_{\text{eff}}$  alone, and below we will use this parameter to present the interferometric results. However, if there is also a stellar flux contribution, than its projection and visibility will be a function of the projected baseline  $B_p$  only (if the star appears spherical in the sky). Consequently, models with both stellar and disk contributions should be presented for both the major and minor axis directions in order to show the range in visibility with baseline direction in a single plot. Along the minor axis, for example,  $\phi_{\text{obs}} - PA = 90^\circ$ , so that the

relation becomes  $B_{\text{eff}} = B_p \cos i$ , and consequently for edge-on systems with  $i \sim 90^\circ$  a given  $B_{\text{eff}}$  may correspond to a  $B_p$  far larger than available with the Array. Such observations (if possible) would start to resolve the stellar disk and lead to low net visibility (see the dotted line in Fig. 8.3).

### 5.3. Model Degeneracy

The simple geometrical representation of the Be star system may in some cases present a solution family or degeneracy that exists between two fundamental parameters of the Gaussian elliptical model: the Gaussian full width at half maximum  $\theta_{\text{maj}}$  and the stellar photospheric contribution  $c_p$ . In order to explain the ambiguity in the model, we consider the case of a locus of  $(c_p, \theta_{\text{maj}})$  that produces the same visibility measurement at a particular baseline. We illustrate this relation in Figure 6, which shows an example of a series of  $(c_p, \theta_{\text{maj}})$  Gaussian elliptical visibility curves that all produce a visibility point  $V = 0.8$  at a projected baseline of 200 m (for  $\lambda = 2.1329 \mu\text{m}$  and a Be star angular diameter  $\theta_{\text{UD}} = 0.3 \text{ mas}$ ). The plot shows models for  $(c_p, \theta_{\text{maj}}) = (0.156, 0.6 \text{ mas})$  (solid line),  $(c_p, \theta_{\text{maj}}) = (0.719, 1.2 \text{ mas})$  (dotted line), and  $(c_p, \theta_{\text{maj}}) = (0.816, 2.4 \text{ mas})$  (dashed line). Figure 7 shows the relationship between the Gaussian elliptical full width at half maximum and the stellar photospheric contribution for the family of curves that go through the observed point  $V = 0.8$  at a 200 m baseline. Larger circumstellar disks are associated with larger stellar flux contributions, and vice-versa, which demonstrates that a single interferometric measurement does not discriminate between a bright small disk and a large faint one. Additional measurements at different baselines are necessary to resolve this ambiguity.

Note that if the interferometric observations are all located on one projected baseline in the  $(u, v)$  plane, then the disk properties are defined in only one dimension. Thus, in such circumstances it is not possible to estimate the axial ratio  $r$  or the position angle of the disk major axis  $PA$ . Only a lower limit for  $\theta_{\text{maj}}$  can be set in such cases.

### 5.4. Fitting Results

The circumstellar disk is modeled with a Gaussian elliptical flux distribution centered on the Be star. This disk model has four independent parameters ( $r, PA, c_p, \theta_{\text{maj}}$ ), and one assumed parameter, the stellar diameter  $\theta_s$  (Table 6). The fitting procedure consists of solving for the model parameters using the IDL non-linear least squares curve fitting routine MPFIT (Markwardt 2009), which provides a robust way to perform multi-parameter surface

fitting. Model parameters can be fixed or free depending on the  $(u, v)$  distribution of the observations.

For the cases with limited coverage in the  $(u, v)$  plane, setting some model parameters to fixed values was necessary in order to fit successfully the data. We adopted additional constraints on some model parameters that are well defined from studies such as inclination estimates from Frémat et al. (2005) and intrinsic polarization angles from McDavid (1999) and Yudin (2001). Also, we occasionally used values of the IR flux excess derived from the SEDs of Be stars to estimate the stellar photospheric contribution  $c_p$  when needed.

Our fitting results are summarized in Table 7, where the cases with a fixed parameter are identified by a zero value assigned to its corresponding uncertainty. Column 1 of Table 7 lists the HD number of the star, columns 2 and 3 list the axial ratio  $r$  and its uncertainty, columns 4 and 5 list the disk position angle along the major axis  $PA$  and its uncertainty, columns 6 and 7 list the photospheric contribution  $c_p$  and its uncertainty, columns 8 and 9 list the angular FWHM of the disk major axis  $\theta_{\text{maj}}$  and its uncertainty, column 10 lists the reduced  $\chi^2_\nu$  of the fit, columns 11 and 12 list the corrected photospheric contribution  $c_p(\text{corr})$  and its uncertainty (see § 5.5), respectively, columns 13 and 14 list the disk-to-star radius ratio  $R_d/R_s$  and its uncertainty, and finally, column 15 indicates the cases of fully resolved disks (Y), marginally resolved disks (M), and unresolved disks (N) in our Be star sample.

Plots of the best-fit solutions showing the visibility curves of the system disk-plus-star as a function of the effective baseline in meters along with our interferometric data are presented in Figure Set 8. The solid lines in Figure Set 8 represent the best-fit visibility model of the disk along the major axis, the dotted lines represent the best-fit visibility model of the disk along the minor axis, and the star signs represent the interferometric data.

We find that the circumstellar disks of the four Be stars, HD 23630, HD 138749, HD 198183, and HD 217675 were unresolved at the time of our CHARA Array observations, while the circumstellar disks of HD 23862, HD 142926, HD 164284, HD 166014, HD 200120, and HD 212076 were only marginally resolved. Those are the cases where we had to fix  $r$ ,  $PA$ , and/or  $c_p$  in order to make Gaussian elliptical model fits to the data. On the other hand, we successfully resolved the circumstellar disks around the other 14 Be stars and were able to perform four-parameter Gaussian elliptical fits for most of them as listed in Table 7.

## 5.5. Corrections to the Gaussian Model

Modeling a circumstellar disk with an elliptical Gaussian intensity distribution is convenient but not completely realistic. The flux distribution in the model assumes that light

components from the circumstellar disk and the central star are summed and that no mutual obscuration occurs. It is important to note that in the case of small disks most of the model disk flux is spatially coincident with the photosphere of the star, so the assignment of the flux components becomes biased.

To illustrate this effect, we show in Figure 9 the model components for a case with a faint disk. The dotted line in Figure 9 shows the assumed form of the intensity of the uniform disk of the star (angular diameter of 0.68 mas), the dashed line shows the Gaussian distribution of the circumstellar disk along the projected major axis (FWHM = 0.55 mas), and the solid line shows the sum of the two intensity components. In the case where the FWHM of the circumstellar emission is similar to or smaller than the stellar diameter, most of the disk flux occurs over the stellar photosphere where the sum produces a distribution similar to that of a limb-darkened star.

The interpretation of the results obtained from the Gaussian elliptical fits must be regarded with caution in situations where the derived disk radius is smaller than the star’s radius and a significant fraction of the disk flux is spatially coincident with that of the star. Consequently, we decided to correct the Gaussian elliptical fitting results in two ways. First, the disk radius was set based upon the relative intensity decline from the stellar radius, and we adopted the disk radius to be that distance where the Gaussian light distribution along the major axis has declined to half its value at the stellar equator. The resulting ratio of disk radius to star radius is then given by

$$\frac{R_d}{R_s} = (1 + (\theta_{\text{maj}}/\theta_s)^2)^{1/2} \quad (22)$$

where  $\theta_{\text{maj}}$  is the Gaussian full-width at half maximum along the major axis derived from the fits, and  $\theta_s$  is the angular diameter of the central star. Secondly, the model intensity over the photosphere of the star from both the stellar and disk components was assigned to the flux from the star in an optically thin approximation. The fraction of the disk flux that falls on top of the star is  $f(1 - c_p)$ , where  $f$  is found by integrating over the stellar disk the Gaussian spatial distribution given by (Tycner et al. 2004)

$$I_{\text{env}}(x, y) = \frac{4 \ln 2}{\pi r \theta_{\text{maj}}^2} \exp \left[ -\frac{(x^2/r^2 + y^2)}{\theta_{\text{maj}}^2/4 \ln 2} \right] \quad (23)$$

where  $r$  is the axial ratio and  $(x, y)$  are the sky coordinates in the direction of the minor and major axes. Consequently, this fraction of the model disk flux should be reassigned to the star and removed from the disk contribution. Then the revised ratio of total disk to stellar flux is

$$\frac{F_d}{F_\star} = \frac{(1 - c_p)(1 - f)}{c_p + (1 - c_p)f} = \frac{1 - c_p(\text{corr})}{c_p(\text{corr})} \quad (24)$$

which is lower than the simple estimate of  $(1 - c_p)/c_p$ . We list in columns 11 to 14 of Table 7 the revised values of the stellar flux contribution  $c_p$  and the Be disk radius  $R_d/R_s$  (along with the corresponding uncertainties) obtained by applying this correction using the stellar angular diameters from Table 6.

## 6. Discussion

### 6.1. Comparison with Other Results

It is important to validate our results against other published data wherever possible. However, since this is the first large scale study of the  $K$ -band emission of northern Be stars, it is difficult to make direct comparisons. We list in Table 8 the available measurements of Gaussian elliptical model parameters of Be star disks for the stars in our sample (excluding the work of Gies et al. 2007 that is included in our analysis). There is only one other  $K$ -band measurement available by Pott et al. (2010), but even in this case a direct comparison of  $\theta_{\text{maj}}$  is difficult because of the different assumptions made about the remaining parameters. Measurements of the disk emission in other bands will likely yield different diameter estimates (§6.2). Nevertheless, we can compare our results on the geometry of the disks with previous work, and we can consider the parameter estimates resulting from other kinds of observations.

We begin by comparing the stellar and disk flux contributions that we derived from the Gaussian elliptical fits (Table 7) with those estimated from the IR-excess in the spectral energy distributions (Table 6). Among the 14 stars in our sample with reliable detections of disk emission, we fit for the stellar flux contribution in six cases. The corrected parameter  $c_p(\text{corr}) = F_s/(F_s + F_d)$  is plotted together with the SED estimate of this ratio in Figure 10. The uncertainties are significant, but these two estimates of stellar flux in the  $K$ -band appear to be consistent (perhaps surprisingly so, because of the known temporal flux variations and large time span between the 2MASS photometry and our interferometric observations).

Next we consider the disk axial ratio  $r$  that is related approximately to the disk normal inclination  $i$  by (Grundstrom & Gies 2006)

$$r \approx \cos i + 0.022 \sqrt{\frac{R_d}{R_s}} \sin i \quad (25)$$

where the second term accounts for the increase in the minor axis size caused by the increase in disk thickness with radius. We expect that the disk inclination will be the same as the stellar spin inclination because the disk is probably fed by equatorial mass loss. Frémat et al. (2005) estimated the stellar inclinations for most of our targets by comparing the projected rotational velocity  $V \sin i$  with the critical rotational velocity  $V_{\text{crit}}$ , for which the equatorial

centripetal and gravitational accelerations balance, and by assuming that Be stars as a class share a common ratio of angular rotational to critical velocity. The axial ratios derived from their estimates of spin inclination are given in the final column of Table 1. There are seven targets with fitted estimates of  $r$  among our 14 reliable detections, and we plot these values together with  $r(i)$  from the inclinations from Frémat et al. (2005) in Figure 11 (indicated by square symbols). Figure 11 includes other  $r$  estimates from previous interferometry (Table 8). With two exceptions ( $v$  Cyg = HD 202904 above and  $\gamma$  Cas = HD 5394 below), the estimates from interferometry and rotational line broadening are in broad agreement. Three of our targets have prior interferometric estimates of  $r$ , and our results agree within the uncertainties. Note that the increase in disk thickness with radius implies that  $r$  will appear larger in bands where the disk emission extends to larger radius ( $H\alpha$ ), and in two cases ( $\psi$  Per = HD 22192 and  $\zeta$  Tau = HD 37202)  $r(H\alpha)$  is larger than  $r(K\text{-band})$ , while they are the same in the third case ( $\gamma$  Cas = HD 5394).

The disk normal is expected to have the same position angle in the sky as that for the intrinsic polarization (from scattering in the inner disk; Quirrenbach et al. 1997). We show in Figure 12 a comparison of the position angles derived from interferometry with those from polarimetric studies (McDavid 1999; Yudin 2001). These generally agree within the uncertainties, but there are some exceptions ( $v$  Cyg = HD 202904 and several cases with large axial ratio  $r$  where it is difficult to determine position angle). Our results are fully consistent for four targets with previous interferometric estimates of  $PA$ . All these comparisons lend support to our strategy of fixing the  $c_p$ ,  $r$ , and  $PA$  parameters in those cases where there were ambiguities with the full four-parameter, Gaussian elliptical fit.

## 6.2. Disk Diameters

We clearly detected the visibility decline due to the disk in 14 stars in our sample. The ratio of disk to stellar radius (Table 7, column 13) varies from 1.5 to 10 with a mean value of 4.4 among this subsample, but our detections are probably biased towards those cases with larger and brighter disks. We compare these  $K$ -band diameters with those measured for  $H\alpha$  (Table 8) in Figure 13, and this demonstrates that in most cases the  $H\alpha$  disk diameters are much larger. Gies et al. (2007) attributed this difference to the larger opacity of  $H\alpha$  compared to the free-free and bound-free opacities that dominate the disk emission in the near-infrared. There are three targets that fall below the trend:  $v$  Cyg = HD 202904 (but with an uncertainty that may be consistent with the trend),  $\phi$  Per = HD 10516, and  $\kappa$  Dra = HD 109387. It is curious that the latter two are both short-period binaries, and it may be that the usually larger  $H\alpha$  emitting regions are truncated by tidal forces, so that their  $K$ -band and

H $\alpha$  disk sizes are comparable. After setting aside these three discrepant cases, the unweighted slope of the relation starting from an origin at  $(R_d(K\text{-band})/R_s, R_d(\text{H}\alpha)/R_s) = (1, 1)$  is  $\Delta R_d(\text{H}\alpha)/\Delta R_d(K\text{-band}) = 4.0 \pm 0.5$  (s.d. of the mean), and this slope is indicated by a dotted line in Figure 13. Such a correlation is helpful in predicting the size of the circumstellar disk in the  $K$ -band from H $\alpha$  observations, and vice-versa, especially since Be star disks are generally highly variable and simultaneous, multiwavelength observations are usually difficult to obtain.

Next, we consider the connection between disk size and brightness. If the disk gas near the central Be star has a temperature that is some fraction of the stellar temperature, then we might expect to find a correlation between the surface intensity  $I$  of the inner disk and star in the limit of high disk optical depth,

$$I_{\text{env}}(x = 0, y = \theta_s/2) = bI_s \quad (26)$$

for some constant  $b$ . We can explore this relationship by considering the Gaussian elliptical model prediction for the disk brightness at the stellar equator (Tycner et al. 2004),

$$I_{\text{env}}(x = 0, y = \theta_s/2) = (1 - c_p) \frac{4 \ln 2}{\pi r \theta_{\text{maj}}^2} 2^{-(\theta_s/\theta_{\text{maj}})^2}. \quad (27)$$

The mean stellar intensity in the model is

$$I_s = \frac{c_p(\text{CORR})}{\pi(\theta_s/2)^2}. \quad (28)$$

Then we can equate these with proportionality constant  $b$  to obtain

$$\frac{1 - c_p}{c_p(\text{CORR})} = br(\theta_{\text{maj}}/\theta_s)^2 2^{(\theta_{\text{maj}}/\theta_s)^2}. \quad (29)$$

This relation predicts that the disk to star flux ratio (left hand side) is approximately proportional to the ratio of disk to star projected area (right hand side).

The Gaussian elliptical parameters from Table 7 and the stellar angular diameters from Table 6 were used to calculate the terms on both sides of the equation, and they are plotted together in Figure 14 (where we assumed a minimum uncertainty of 5% for those cases where the formal uncertainties may be underestimated). We see that the Be stars with the largest disk to stellar flux ratio are often those with a large ratio of circumstellar to stellar angular diameter. However, a counter example is the case of  $\kappa$  Dra = HD 109387 that is plotted with a large but faint disk (lower right location in Fig. 14). The fit of the Gaussian elliptical model parameters in this case is constrained by a set of 100 m baseline measurements from Gies et al. (2007) (see Fig. 8.10), and if a fit was made from the new measurements alone,

then the disk size would be much smaller (as also suggested by the smaller H $\alpha$  disk size shown in Fig. 13). Given these uncertainties, our measurement for  $\kappa$  Dra may be set aside from consideration here. An unweighted, nonparametric, correlation test for the remaining 13 Be stars yields a Kendall’s statistic of  $\tau = 0.205$ , which has null rejection probability of 37%, i.e., a value which is not small enough to reject with confidence the null hypothesis of no correlation. We suspect that the poor correlation results from a break down among the faint disk stars of our simplifying assumption that the disks are optically thick, which may only be applicable to the brightest disk cases. We show for completeness in Figure 14 a linear fit of the sample of 13 stars that has a constant of proportionality of  $b = 0.18 \pm 0.04$  (s.d. of the mean). We caution again that such a relation may only hold for dense, optically thick disks and that our results may be biased against detection of fainter disks in general. We are planning to investigate further the question of disk surface intensity in another paper that will apply physical models and radiative transfer calculations to fit the observed visibilities.

### 6.3. Detection Limits

We found that the criterion for a confident detection of the circumstellar disk is usually a decline in visibility below  $V = 0.8$  at the longest baselines available. We can use this criterion to estimate the limitations on disk sizes that we can detect for Be stars at different distances. The visibility measured along baselines aligned with the projected major axis of the disk is a function of the photospheric flux fraction  $c_p$ , the ratio of disk to stellar radius  $R_d/R_s$ , and the stellar angular diameter  $\theta_s$  (eq. 17, 18, 19). Thus, given  $R_d/R_s$  and  $\theta_s$  we can find  $\theta_{\text{maj}}$ , and the remaining parameter to estimate is  $c_p$ . In practice this could be estimated from a simultaneous analysis of the SED of the Be star. However, for our purpose here, we adopted the relationship between the disk to star flux ratio and projected surface areas (eq. 29 and Fig. 14) to estimate  $c_p$  from  $r$  and  $R_d/R_s$ . This relationship is poorly defined for fainter disks ( $(1 - c_p)/c_p < 1$ ), where the disks become optically thin and the ratio of areas argument no longer applies.

The stellar angular diameter is found from the assumed stellar radius and distance, and we made estimates for two cases, B0 V and B8 V types for the Be star, and for three distances corresponding to visual magnitudes 3, 5, and 7. We used stellar radii and absolute magnitudes for these classifications from the compilation of Gray (2005), and we neglected any extinction in the calculation of distance from the magnitude difference. Figure 15 shows the resulting predicted visibilities for a  $K$ -band measurement with a projected baseline of 300 m as a function of  $R_d/R_s$  for these different cases. Each plot shows how the visibility at this baseline declines as the disk size increases, and we can use these to estimate the



smallest disk detectable. For example, we see in Figure 15a for a B0 V star of apparent magnitude 5 that the curve dips below  $V = 0.8$  at  $R_d/R_s = 3.4$  from which we would infer that only disks larger than this would be detected with the CHARA Array. As expected, we can detect smaller disks in nearer (brighter) Be stars. Figure 15b shows the case for a later B8 V type that is somewhat more favorable for detection of smaller disks. Note that at small disk radii we simply assume that all the flux is stellar, so the limiting visibility near  $R_d/R_s = 1$  corresponds to the stellar visibility.

#### 6.4. Rotational and Critical Velocities

Be stars are generally fast rotators, but it is difficult to determine the actual equatorial rotational velocity  $V_{\text{rot}}$  from the observed projected rotational velocity  $V \sin i$  (measured from the rotational Doppler broadening of the lines; Townsend et al. 2004) because of the unknown stellar inclination  $i$ . If we assume that the stellar spin and disk rotational axes are coaligned, then we can use the disk axial ratio to set the stellar inclination (eq. 25). We collected the seven  $r$  values derived from our fits (Table 7) together with estimates from previous work (Table 8) to find mean  $\sin i$  factors for 12 Be stars in our program. We adopted the projected photospheric rotational velocities  $V \sin i$  and the critical rotational velocities  $V_{\text{crit}}$  from Frémat et al. (2005), who derived these values after making corrections for the effects of gravity darkening. Then we divided  $V \sin i$  by  $\sin i$  to find the equatorial rotational velocity  $V_{\text{rot}}$ . Our results appear in Table 9 that lists the HD number of the star,  $V \sin i$  and  $V_{\text{crit}}$  (Frémat et al. 2005),  $V_{\text{rot}}$ , and two ratios,  $V_{\text{rot}}/V_{\text{crit}}$  and  $\Omega_{\text{rot}}/\Omega_{\text{crit}}$ . The ratio of angular rotational velocities is given for the Roche approximation using expressions from Ekström et al. (2008),

$$\frac{\Omega_{\text{rot}}}{\Omega_{\text{crit}}} = \frac{3}{2} \frac{V_{\text{rot}}}{V_{\text{crit}}} \left[ 1 - \frac{1}{3} \left( \frac{V_{\text{rot}}}{V_{\text{crit}}} \right)^2 \right]. \quad (30)$$

We find that most of the stars in this subsample are rotating very quickly, and two targets may have attained the critical rate ( $\gamma$  Cas = HD 5394 and 48 Lib = HD 142983). However, there are two targets with much more moderate rotational velocities,  $\beta$  Psc = HD 217891 and  $v$  Cyg = HD 202904. The former has a rather large axial ratio  $r = 0.70 \pm 0.15$ , and it is possible that the uncertainties would allow a small inclination and hence large rotational velocity. However, the case of  $v$  Cyg is more difficult to understand. Neiner et al. (2005) argue on the basis of the narrow lines in the spectrum that the axial ratio should be close to  $r \approx 0.9$  if it is actually a rapid rotator. This is much larger than the value we derive from the Gaussian elliptical fits,  $r = 0.26 \pm 0.13$ . Additional interferometric observations are needed to confirm or remove this discrepancy.

We find a mean angular velocity ratio of  $\Omega_{\text{rot}}/\Omega_{\text{crit}} = 0.88 \pm 0.17$  (s.d.) for the sample of 12 Be stars or  $0.95 \pm 0.04$  (s.d.) if we remove  $\beta$  Psc and  $v$  Cyg from the sample. These results support earlier Be star angular velocity ratio estimates of 0.88 (Frémat et al. 2005), 0.7 – 1.0 (Cranmer 2005), 0.8 – 1.0 (Huang et al. 2010), and  $0.95 \pm 0.02$  (Meilland et al. 2012). The consistency of these results suggests that rapid rotation in Be stars plays a key role in the Be phenomenon.

## 7. Conclusions

Our CHARA Array interferometric survey of northern sky Be stars has led to the resolution of extended  $K$ -band continuum emission from the disks of 14 stars among of our sample of 24 stars. We interpreted the visibility measurements with a simple geometrical model that assumes a Gaussian elliptical brightness distribution for the circumstellar disks. The model fits yield estimates of the disk angular diameter, axial ratio, position angle, and the photospheric and disk flux contributions in the  $K$ -band. We demonstrated that the results are consistent with earlier interferometric studies of the disk  $H\alpha$  emission and with other estimates for the disk parameters from spectroscopic and polarimetric studies.

We determined estimates for the stellar angular diameters and infrared flux excesses from fits of the ultraviolet and near-infrared spectral energy distributions. We find that the mean ratio of the  $K$ -band disk to stellar diameter is 4.4 with a range from 1.5 to 10 for the detected cases. The ratio is similar among both early- and late-type Be stars, which suggests that Be star disks tend to scale in size and flux with the properties of the central star (although we caution that fainter, smaller disks may have escaped detection). The diameters of the  $K$ -band emitting region are much smaller than those for the  $H\alpha$  emission in most cases, and the difference is probably due to the higher opacity of  $H\alpha$  that extends the emission to the lower density gas found at larger radii. The apparent axial ratio of the disk emission is related to the disk inclination, and we can reliably assign the derived inclination to the stellar spin axis also. We used the interferometrically observed axial ratios for a sub-sample of 12 Be stars to convert the projected rotational velocity from spectroscopy to the equatorial rotational velocity, and we found that these stars generally rotate close to their critical velocities.

We were surprised to find that so many of our targets (14 of 24) are members of binary and multiple star systems, and we developed methods to account for the influence of the flux of the companions on the interferometric visibilities. Some Be stars may have been spun up through mass transfer in a close binary system (Pols et al. 1991), and we have identified the spectral features of the hot, stripped-down, mass donor star in several cases

(Gies et al. 1998; Maintz et al. 2005; Peters et al. 2008). Tokovinin et al. (2006) has found that a large fraction of close, spectroscopic binaries among solar-type stars have distant third companions, and it is possible that the tertiary received the excess angular momentum from the natal cloud that needed to be removed from the central region in order to form a close binary during star formation. Thus, the presence of a wide companion around a Be star may indicate that the central object was originally a close binary that subsequently experienced interaction, mass transfer, and spin-up of the gainer. The derivation of orbits for these wide companions will be especially useful to measure masses of Be stars and to see, for example, if they are overluminous for their mass because of large scale internal mixing caused by mass transfer and fast rotation (Gies et al. 1998).

Our survey provides a first epoch of diameter measurements that will serve in future studies of the growth and dissipation of disks that are frequently observed in Be stars (Porter & Rivinius 2003). The Gaussian elliptical models provide a useful but first-order description of the disks, and it will be important to explore the development of disk asymmetries related to disk instabilities (such as one-armed spiral features; Carciofi et al. 2009). Such studies will require closure phase measurements in addition to interferometric visibility, and instruments at the CHARA Array like the Michigan Infrared Combiner (Monnier et al. 2010) and VEGA (Mourard et al. 2011) that use multiple telescopes and baselines will eventually allow us to reconstruct images of Be star disks. Such images will be vitally important to test physical models of the disks and to determine the nature of the companion stars.

We are grateful to Vincent Coudé du Foresto, William Hartkopf, Carol Jones, Robert Kurucz, Brian Mason, Rafael Millan-Gabet, John Monnier, David O’Brien, Deepak Raghavan, Lewis Roberts, Philippe Stee, and Christopher Tycner for important contributions to this work. This material is based upon work supported by the National Science Foundation under Grants AST-0606861 and AST-1009080 (Gies) and AST-0606958 and AST-0908253 (McAlister). STR acknowledges partial support from NASA grant NNH09AK731. Yamina Touhami also gratefully acknowledges the support of a Georgia Space Grant Consortium Fellowship and a NASA/NExScI visiting fellowship to the California Institute of Technology. Institutional support has been provided from the GSU College of Arts and Sciences and from the Research Program Enhancement fund of the Board of Regents of the University System of Georgia, administered through the GSU Office of the Vice President for Research and Economic Development. The *IUE* spectra presented in this paper were obtained from the Mikulski Archive for Space Telescopes (MAST) at STScI. STScI is operated by the Association of Universities for Research in Astronomy, Inc., under NASA contract NAS5-26555. Support for MAST for non-HST data is provided by the NASA Office of Space Science via grant NNX09AF08G and by other grants and contracts.

Facilities: CHARA Array

### A. Notes on Individual Stars

*HD 4180.* Koubský et al. (2010) present a single-lined spectroscopic orbit for HD 4180 plus interferometric observations from NPOI of the resolved system A,B. The components of this binary system are too close for speckle resolution, and the object appeared single in observations by Mason et al. (1997). Grundstrom (2007) observed spectral features corresponding to two similar late-B or early-A stars that showed Doppler shifts on a timescale of approximately 4 days, and these probably form in the close (Ba, Bb) system that was suspected by Koubský et al. (2010). We have estimated the  $K$ -band magnitude difference using the magnitude difference from NPOI  $\Delta R = 2.9$  mag (Koubský et al. 2010), the estimated spectral types from Koubský et al. (2010), the near-IR color calibration from Wegner (1994), and the flux excess  $E^*(V^* - K) = 0.13$  mag from Touhami et al. (2011).

*HD 5394.*  $\gamma$  Cas is a single-lined spectroscopic binary with a faint (undetected) companion (Harmanec et al. 2000; Miroshnichenko et al. 2002; Nemravová et al. 2012; Smith et al. 2012). Although this binary could be resolved in our CHARA visibility observations, the expected large magnitude difference makes detection very difficult. The distant and faint B companion (Roberts et al. 2007) will have no influence on our measurements. Smith et al. (2012) and Stee et al. (2012) discuss CHARA Array  $H$ -band and  $R$ -band measurements of the disk size and orientation.

*HD 10516.*  $\phi$  Per is a double-lined spectroscopic system with a hot subdwarf companion (Gies et al. 1998). We used the FUV flux ratio, temperatures, and gravities from Gies et al. (1998) and derived magnitude differences by scaling model spectral energy distributions from Lanz & Hubeny (2003).

*HD 22192.* No companion is evident in speckle data (Mason et al. 1997) nor in CHARA VEGA interferometric observations (Delaa et al. 2011).

*HD 23630.* Alcyone is a bright Pleiades member with seven visual components listed in the WDS, but all these components have separations greater than 79 arcsec. The star appears single in speckle (Mason et al. 1997) and AO observations (Roberts et al. 2007).

*HD 23862.* Pleione is a single-lined spectroscopic binary with a low mass companion, possibly a hot subdwarf or a M-dwarf (Nemravová et al. 2010). The next companion is CHARA 125 that has a separation of  $\rho \approx 0''.23$  (Mason et al. 1993; Roberts et al. 2007), but it is not always detected in speckle measurements, indicating a large magnitude difference of  $\Delta V \approx 3.5$

mag. Luthardt & Menchenkova (1994) present a radial velocity study that suggests that the orbital period is  $\approx 35$  y, and the eccentricity is found to be large. We assumed that the orbital period is the same as that associated with the spectroscopic shell episodes  $P = 34.5$  y (Sharov & Lyutyi 1988; Tanaka et al. 2007) and that speckle companion CHARA 125 is the companion in this orbit (Gies et al. 1990). We then made a preliminary orbital fit of the speckle data (Mason et al. 1993) to arrive at the elements presented in Table 5, although we caution that this is probably only one of a family of possible solutions. There are five other, fainter but wider ( $\rho > 4''.6$ ), visual companions in the WDS, which should not affect our measurements.

*HD 25940.* No companion is evident in the CHARA VEGA observations of Delaa et al. (2011). No speckle observations of this star are published.

*HD 37202.* Ruždjak et al. (2009) present an analysis of the single-lined spectroscopic orbit for  $\zeta$  Tau. No other components are found in speckle (Mason et al. 1993) or interferometric observations (Štefl et al. 2009; Schaefer et al. 2010). Interferometric observations of disk asymmetries are described by Štefl et al. (2009), Carciofi et al. (2009), and Schaefer et al. (2010).

*HD 58715.* Jarad et al. (1989) suggest that  $\beta$  CMi is a single-lined, spectroscopic binary with a period of 218 d, but this result has not yet been confirmed by other investigators. Interferometric studies by Meilland et al. (2009) and Kraus et al. (2012) show no evidence of a close companion. Furthermore, no companion is found in speckle data (Mason et al. 1993) and AO imaging (Janson et al. 2011). Eight faint and distant companions are listed in the WDS.

*HD 109387.* Saad et al. (2005) show that  $\kappa$  Dra is a single-lined, spectroscopic binary with a faint companion. Gies et al. (2007) found that the addition of a hot companion improved the fit of the  $K$ -band interferometry, but Jones et al. (2008) point out that density exponent derived by Gies et al. (2007) is significantly lower than that determined from  $H\alpha$  interferometry. This discrepancy casts some doubt about the detection of the companion. There are no published speckle measurements of this star.

*HD 138749.*  $\theta$  CrB has a companion whose separation has increased from  $0''.642$  in 1976 to  $0''.813$  in 2010 according to the WDS, but the position angle varied by only  $4^\circ$  over the same interval, and this suggests a large orbital eccentricity and/or an inclination  $\approx 90^\circ$ . The  $B, V$ -band magnitudes were measured by Fabricius & Makarov (2000), and these suggest that the system consists of a B6 Vne primary and a A2 V secondary. Assigning masses for these classifications and assuming that the semimajor axis is close to the smallest observed ( $a = 0''.5$ ), we have calculated a preliminary period that is given in Table 5. There are 28

measurements (from 1976 to 2010) of separation and position angle in the Fourth Catalog of Interferometric Measurements of Binary Stars (Hartkopf et al. 2001) that we used to derive the preliminary orbital elements that are given in Table 5. There are no obvious radial velocity variations indicative of a spectroscopic binary (Rivinius et al. 2006).

*HD 142926.* Koubský et al. (1997) present a single-lined spectroscopic orbit for 4 Her. They argue that the companion star must be a small and faint object since they see no evidence of its spectral features. No other companions are observed with speckle interferometry (Mason et al. 1997) nor are any companions listed in the WDS.

*HD 142983.* The spectrum of 48 Lib is dominated by shell features that vary on a timescale of a decade, and it is very difficult to study the photospheric spectrum of the star (B3: IV:e shell) to search for radial velocity variations (Rivinius et al. 2006; Štefl et al. 2012). Unfortunately, there are no published speckle observations, and there are no companions indicated in the WDS. We assume it is a single object. Recent *H*-band interferometric observations are discussed by Štefl et al. (2012).

*HD 148184.* Harmanec (1987) presents a preliminary single-lined orbit for  $\chi$  Oph with a period of 34.121 d. There are no available speckle observations, and no companion is indicated in the WDS. Tycner et al. (2008) obtained  $H\alpha$  interferometric observations, and they make no mention of evidence of a companion.

*HD 164284.* The visual companion of 66 Oph was first discovered by Mason et al. (2009) and confirmed by Tokovinin et al. (2010). We assumed that the current separation corresponds to the angular semimajor axis, and we estimated the orbital period by assigning masses assuming main sequence stars, the temperature from Frémat et al. (2005), and the measured  $\Delta V = 2.7$  mag (Tokovinin et al. 2010). There are only four measurements in the Fourth Catalog of Interferometric Measurements of Binary Stars (Hartkopf et al. 2001), but we used these to arrive at the preliminary orbital elements presented in Table 5. Floquet et al. (2002) discuss spectroscopy of the star and pulsational behavior, but no mention is made of a spectroscopic binary companion.

*HD 166014.* Tokovinin (1985) reported a marginal detection of a close companion to *o* Her at a separation of 60 mas, but this was not confirmed in later speckle observations by Mason et al. (2009). However, the interferometric measurements for this star showed lower visibilities at short baselines, which could not be fitted by the standard Gaussian elliptical model. Consequently, we assumed that this decreased visibility is due to the presence of the companion found by Tokovinin (1985). We applied the binary flux dilution correction to fit the data by assuming a companion that is 2.5 mag fainter than the Be star in the *K*-band. There is no known spectroscopic companion, and Grundstrom (2007) found no evidence of

radial velocity variability.

*HD 198183.* The  $\lambda$  Cyg system consists of at least four stars. Component C is distant and faint, so we ignored its flux. The AB system has a long period ( $\approx 462$  y; Baize 1983), and we used the orbital elements from Baize (1983) to estimate the position of A,B. Balega & Balega (1988) and Baize (1993) determined an astrometric orbit for the close pair MCA 63 Aa,Ab that apparently consists of similar magnitude stars. However, this close pair was not detected in recent speckle observations by Mason et al. (2009), presumably because their separation was too small at that time. Grundstrom (2007) notes the presence of some-short term line profile variability that might be explained as a composite spectrum consisting of the Be star (Aa) plus a single-lined spectroscopic binary, so it is possible that B or Ab has a companion. The magnitude difference of A,B was determined in the Tycho system by Fabricius & Makarov (2000), and we converted this to a Johnson  $\Delta V = 1.46 \pm 0.02$  mag using the formulae from Mamajek et al. (2002). The magnitude and color differences of A,B suggest that component B is a late B-type star, and we used  $\Delta V$ , the effective temperature of Aa from Huang & Gies (2008), and the main sequence relations from Lejeune & Schaerer (2001) to estimate the  $K$ -band magnitude difference. We encountered two problems related to the visibility correction for the inner companion Ab. First, the orbit from Baize (1993) predicted that the Aa and Ab fringe patterns would cross each other for the baseline orientations of observations from JD 2,455,365, and consequently, large visibility variations were predicted when none were observed. We suspect that the orbit needs revision, and for the purposes of the visibility correction, we altered the epoch of periastron from BY 1982.668 to BY 1981.526 so that the predicted, projected separations at the time of our observations were always larger than half the fringe scan length. The second problem concerned the flux contribution of Ab. W. Hartkopf (USNO) kindly retrieved his speckle data on the close Aa,Ab pair and derived an approximate magnitude difference of  $\Delta V = 0.4 \pm 0.3$  mag. Because we have no color information for the close pair, we simply assumed that  $K$ -band magnitude difference was the same. We found that with Ab this bright, the dilution correction was too large and led to corrected visibilities larger than one. By increasing this estimate to  $\Delta V = 0.4 + 1\sigma = 0.7$  mag, the mean of the corrected visibilities was approximately one. This indicates that the Be star disk was probably unresolved, unless the flux contributions of the companions are actually significantly lower than these estimates.

*HD 200120.* 59 Cyg has a nearby B companion (Mason et al. 2009) plus three other very distant and faint components. B. Mason (USNO) kindly provided us with a preliminary orbit for A,B (Table 5) that we used to estimate the position and separation at the times of our CHARA Array observations. The Be star is also a spectroscopic binary with a hot subdwarf companion (Maintz et al. 2005), and consequently we assume that the smaller  $\Delta K$  (brighter) estimate is more reliable in Table 4.

*HD 202904.*  $\nu$  Cyg has four faint and distant companions listed in the WDS, but there is no close companion detected in speckle interferometric observations (Mason et al. 1997). Neiner et al. (2005) discuss spectroscopic radial velocities that may be consistent with binary motion for a period of 11.4 y, but further measurements are required to verify their suggestion.

*HD 203467.* There are no companions of  $\delta$  Cep listed in the WDS, and, unfortunately, there are no published speckle observations of this star. Spectroscopic observations are discussed by Koubský et al. (2003) who show that the profiles vary with a 1.621 d cycle, a period that is probably related to pulsation or rotation.

*HD 209409.* There are no companions of  $\sigma$  Aqr listed in the WDS, and no companions were found by Oudmaijer & Parr (2010) using adaptive optics observations with VLT/NACO. Rivinius et al. (2006) discuss spectroscopy of this Be-shell star and note no evidence of a binary companion. Meilland et al. (2012) obtained preliminary  $K$ -band interferometry with VLTI/AMBER, but they did not resolve the disk in the continuum.

*HD 212076.* No companions of  $\gamma$  Peg are listed in the WDS. Rivinius et al. (2003) describe the short term spectroscopic variations related to pulsations, but there is no evidence of a spectroscopic companion.

*HD 217675.* Zhuchkov et al. (2010) present a re-analysis of all the existing plus new astrometric and radial velocity measurements for  $\sigma$  And. They show that the system has a 2 + 2 hierarchy and the pairs share a wide orbit with a period of 117 y. The A component is probably a spectroscopic binary consisting of the Be star and late-B star companion in a 5.7 y orbit, while the B component consists of a pair of similar late-B stars in a 33 d spectroscopic orbit. We treated the B component as a single object because the binary separation is so small, and then we corrected the visibilities using the orbits from Zhuchkov et al. (2010) and the magnitude differences of  $\Delta V(A, B) = 2.21$  (Zhuchkov et al. 2010) and  $\Delta V(Aa, Ab) = 1.90$  (Horch et al. 2004). The flux ratios in the  $K$ -band were estimated using the  $V - K$  color calibration from Wegner (1994) and spectral types from Zhuchkov et al. (2010).

*HD 217891.* No companions of  $\beta$  Psc are listed in the WDS and none were found in adaptive optics observations by Roberts et al. (2007). Dachs et al. (1986) discuss radial velocity measurements that appear to be relatively constant.

## REFERENCES

- Abt, H. A. 1987, in Physics of Be Stars, Proc. IAU Coll. 92, ed. A. Slettebak & T. P. Snow (Cambridge, UK: Cambridge Univ. Press), 470



- Allende Prieto, C., & Lambert, D. L. 1999, *A&A*, 352, 555
- Ammons, S. M., Robinson, S. E., Strader, J., et al. 2006, *ApJ*, 638, 1004
- Armstrong, J. T., Mozurkewich, D., Vivekanand, M., et al. 1992, *AJ*, 104, 241
- Baize, P. 1993, *A&AS*, 99, 205
- Baize, P. 1983, *A&AS*, 51, 479
- Balachandran, S. 1990, *ApJ*, 354, 310
- Balega, I. I., & Balega, Y. Y. 1988, *Sov. Astron. Lett.*, 14, 393
- Balega, I. I., Balega, Y. Y., Vasyuk, V. A., & McManus, J. J. 1992, in *IAU Colloq. 135: Complementary Approaches to Double and Multiple Star Research (ASP Conf. Ser. 32)*, ed. H. A. McAlister & W. I. Hartkopf (San Francisco: ASP), 469
- Boden, A. F. 2000, in *Principles of Long Baseline Stellar Interferometry (JPL Publ. 00-009)*, ed. P. R. Lawson (Pasadena: NASA JPL), 9
- Boesgaard, A. M., & Friel, E. D. 1990, *ApJ*, 351, 467
- Boesgaard, A. M., & Tripicco, M. J. 1986, *ApJ*, 303, 724
- Carciofi, A. C., Okazaki, A. T., le Bouquin, J.-B., et al. 2009, *A&A*, 504, 915
- Claret, A. 2000, *A&A*, 363, 1081
- Cohen, M., Wheaton, W. A., & Megeath, S. T. 2003, *AJ*, 126, 1090
- Colina, L., Bohlin, R., & Castelli, F. 1996, *HST Instrument Science Report CAL/SCS-008* (Baltimore: STScI)
- Cranmer, S. R. 2005, *ApJ*, 634, 585
- Cutri, R. M., Skrutskie, M. F., van Dyk, S., et al. 2003, *2MASS All-Sky Catalog of Point Sources* (Pasadena: Univ. Massachusetts and IPAC/California Inst. Tech.)
- da Silva, R., Milone, A. C., & Reddy, B. E. 2011, *A&A*, 526, A71
- Dachs, J., Hanuschik, R., Kaiser, D., Ballereau, D., & Bouchet, P. 1986, *A&AS*, 63, 87
- Delaa, O., Stee, Ph., Meilland, A., et al. 2011, *A&A*, 529, A87
- Dougherty, S. M., & Taylor, A. R. 1992, *Nature*, 359, 808

- Dougherty, S. M., Waters, L. B. F. M., Burki, G., et al. 1994, *A&A*, 290, 609
- Dyck, H. M., Benson, J. A., & Schloerb, F. P. 1995, *AJ*, 110, 1433
- Edvardsson, B., Andersen, J., Gustafsson, B., et al. 1993, *A&A*, 275, 101
- Ekström, S., Meynet, G., Chiappini, C., Hirschi, R., & Maeder, A., *A&A*, 489, 685
- Fabricius, C., & Makarov, V. V. 2000, *A&A*, 356, 141
- Fitzpatrick, E. L. 1999, *PASP*, 111, 63
- Floquet, M., Neiner, C., Janot-Pacheco, E., et al. 2002, *A&A*, 394, 137
- Frémat, Y., Zorec, J., Hubert, A.-M., & Floquet, M. 2005, *A&A*, 440, 305
- Fuhrmann, K. 1998, *A&A*, 338, 161
- Gerbaldi, M., Faraggiana, R., & Caffau, E. 2007, *A&A*, 472, 241
- Gies, D. R. 2001, in *The influence of binaries on stellar population studies* (ASSL Vol. 264), ed. D. Vanbeveren (Dordrecht: Kluwer), 95
- Gies, D. R., Bagnuolo, W. G., Jr., Baines, E. K., et al. 2007, *ApJ*, 654, 527
- Gies, D. R., Bagnuolo, W. G., Jr., Ferrara, E. C., et al. 1998, *ApJ*, 493, 440
- Gies, D. R., McKibben, W. P., Kelton, P. W., Opal, C. B., & Sawyer, S. 1990, *AJ*, 100, 1601
- Gray, D. F. 2005, *The Observation and Analysis of Stellar Photospheres*, 3rd Ed. (Cambridge UK: Cambridge Univ. Press)
- Gray, R. O., Napier, M. G., & Winkler, L. I. 2001, *AJ*, 121, 2148
- Grundstrom, E. D. 2007, Ph.D. dissertation, Georgia State Univ.
- Grundstrom, E. D., & Gies, D. R. 2006, *ApJ*, 651, L53
- Harmanec, P. 1987, in *Physics of Be Stars*, IAU Coll. 92, ed. A. Slettebak & T. P. Snow (Cambridge, UK: Cambridge Univ. Press), 339
- Harmanec, P., Habuda, P., Štefl, S., et al. 2000, *A&A*, 364, L85
- Hartkopf, W. I., Mason, B. D. & Worley, C. E. 2001, *AJ*, 122, 3472

- Henize, K. G., Wray, J. D., Parsons, S. B., & Benedict, G. F. 1979, Catalog of Far-Ultraviolet Objective-Prism Spectrophotometry: Skylab Experiment S-019, NASA Ref. Publ. 1031 (Washington, DC: NASA)
- Herbison-Evans, D., Hanbury Brown, R., Davis, J., & Allen, L. R. 1971, MNRAS, 151, 161
- Horch, E. P., Meyer, R. D., & van Altena, W. F. 2004, AJ, 127, 1727
- Huang, W., & Gies, D. R. 2008, ApJ, 683, 1045
- Huang, W., Gies, D. R., & McSwain, M. V. 2010, ApJ, 722, 605
- Janson, M., Bonavita, M., Klahr, H., et al. 2011, ApJ, 736, 89
- Jarad, M. M., Hilditch, R. W., & Skillen, I. 1989, MNRAS, 238, 1085
- Jones, C. E., Tycner, C., Sigut, T. A. A., Benson, J. A., & Hutter, D. J. 2008, ApJ, 687, 598
- Karataş, Y., & Schuster, W. J. 2006, MNRAS, 371, 1793
- Koubský, P., Harmanec, P., Kubát, J., et al. 1997, A&A, 328, 551
- Koubský, P., Hummel, C. A., Harmanec, P., et al. 2010, A&A, 517, A24
- Koubský, P., Yang, S., Floquet, M., et al. 2003, in Magnetic Fields in O, B and A Stars: Origin and Connection to Pulsation, Rotation and Mass Loss (ASP Conf. Ser. 305), ed. L. A. Balona, H. F. Henrichs, & R. Medupe (San Francisco: ASP), 295
- Kraus, S., Monnier, J. D., Che, X., et al. 2012, ApJ, 744, 19
- Lafrasse, S., Mella, G., Bonneau, D., et al. 2010, in Optical and Infrared Interferometry II, Proceedings of the SPIE, Vol. 7734, ed. W. C. Danchi, F. Delplancke, & J. K. Rajagopal (Bellingham, WA: SPIE), 4E
- Lanz, T., & Hubeny, I. 2003, ApJS, 146, 417
- Lejeune, T., & Schaerer, D. 2001, A&A, 366, 538
- Luthardt, R., & Menchenkova, E. V. 1994, A&A, 284, 118
- Maintz, M., Rivinius, Th., Stahl, O., Štefl, S., & Appenzeller, I. 2005, Publ. Astron. Inst. Cz. Acad. Sci., 93, 21
- Mamajek, E. E., Meyer, M. R., & Liebert, J. 2002, AJ, 124, 1670

- Markwardt, C. B. 2009, in *Astronomical Data Analysis Software and Systems XVIII* (ASP Conf. Ser. 411), ed. D. A. Bohlender, D. Durand, & P. Dowler (San Francisco: ASP), 251
- Masana E., Jordi C., & Ribas I. 2006, *A&A*, 450, 735
- Mason, B. D., Hartkopf, W. I., McAlister, H. A., & Sowell, J. R. 1993, *AJ*, 106, 637
- Mason, B. D., ten Brummelaar, T., Gies, D. R., Hartkopf, W. I., & Thaller, M. L. 1997, *AJ*, 114, 2112
- Mason, B. D., Wycoff, G. L., Hartkopf, W. I., Douglass, G. G., & Worley, C. E. 2001, *AJ*, 122, 3466
- Mason, B. D., Hartkopf, W. I., Gies, D. R., Henry, T. J., & Helsel, J. W. 2009, *AJ*, 137, 3358
- McDavid, D. 1999, *PASP*, 111, 494
- Meade, M. R., & Code, A. D. 1980, *ApJS*, 42, 283
- Meilland, A., Delaa, O., Stee, Ph., et al. 2011, *A&A*, 532, A80
- Meilland, A., Millour, F., Kanaan, S., et al. 2012, *A&A*, 538, A110
- Meilland, A., Millour, F., Stee, Ph., et al. 2007, *A&A*, 464, 73
- Meilland, A., Stee, Ph., Chesneau, O., & Jones, C. 2009, *A&A*, 505, 687
- Miroshnichenko, A. S., Bjorkman, K. S., & Krugov, V. D. 2002, *PASP*, 114, 1226
- Monet, D. G., Levine, S. E., Canzian, B., et al. 2003, *AJ*, 125, 984
- Monnier, J. D., Anderson, M., Baron, F., et al. 2010, in *Optical and Infrared Interferometry II*, Proceedings of the SPIE, Vol. 7734, ed. W. C. Danchi, F. Delplancke, & J. K. Rajagopal (Bellingham, WA: SPIE), 0G
- Mourard, D., Bério, Ph., Perraut, K., et al. 2011, *A&A*, 531, A110
- Neiner, C., Floquet, M., Hubert, A. M., et al. 2005, *A&A*, 437, 257
- Nemravová, J., Harmanec, P., Koubský, P., et al. 2012, *A&A*, 537, A59
- Nemravová, J., Harmanec, P., Kubát, J., et al. 2010, *A&A*, 516, A80

- O'Brien, D. P., McAlister, H. A., Raghavan, D., et al. 2011, *ApJ*, 728, 111
- Oudmaijer, R. D., & Parr, A. M. 2010, *MNRAS*, 405, 2439
- Peters, G. J., Gies, D. R., Grundstrom, E. D., & McSwain, M. V. 2008, *ApJ*, 686, 1280
- Philip, A. D., & Egret, D. 1980, *A&AS*, 40, 199
- Pols, O. R., Coté, J., Waters, L. B. F. M., & Heise, J. 1991, *A&A*, 241, 419
- Porter, J. M., & Rivinius, Th. 2003, *PASP*, 115, 1153
- Pott, J.-U., Woillez, J., Ragland, S., et al. 2010, *ApJ*, 721, 802
- Prugniel, Ph., & Soubiran, C. 2001, *A&A*, 369, 1048
- Quirrenbach, A., Bjorkman, K. S., Bjorkman, J. E., et al. 1997, *ApJ*, 479, 477
- Raghavan, D., Farrington, C. D., ten Brummelaar, T. A., et al. 2012, *ApJ*, 745, 24
- Raghavan, D., McAlister, H. A., Torres, G., et al. 2009, *ApJ*, 690, 394
- Rivinius, Th., Baade, D., & Štefl, S. 2003, *A&A*, 411, 229
- Rivinius, Th., Štefl, S., & Baade, D. 2006, *A&A*, 459, 137
- Roberts, L. C., Jr., Turner, N. H., & ten Brummelaar, T. A. 2007, *AJ*, 133, 545
- Ruždjak, D., Božić, H., Harmanec, P., et al. 2009, *A&A*, 506, 1319
- Saad, S. M., Kubát, J., Hadrava, P., et al. 2005, *Ap&SS*, 296, 173
- Schaefer, G. H., Gies, D. R., Monnier, J. D., et al. 2010, *AJ*, 140, 1838
- Schröder, C., Reiners, A., & Schmitt, J. H. M. M. 2009, *A&A*, 493, 1099
- Sharov, A. S., & Lyutyi, V. M. 1988, *Sov. Astron.*, 32, 303
- Skrutskie, M. F., Cutri, R. M., Stiening, R., et al. 2006, *AJ*, 131, 1163
- Smith, M. A., Lopes de Oliveira, R., Motch, C., et al. 2012, *A&A*, 540, A53
- Soubiran, C., Le Campion, J.-F., Cayrel de Strobel, G., & Caillo, A. 2010, *A&A*, 515, A111
- Starikova, G. A. 1982, *Sov. Astron. Lett.*, 8, 166

- Stee, Ph. 2011, in *Active OB stars: structure, evolution, mass loss, and critical limits*, IAU Symp. 272, ed. C. Neiner, G. Wade, G. Meynet, & G. Peters (Cambridge, UK: Cambridge Univ. Press), 313
- Stee, Ph., Delaa, O., Monnier, J. D., et al. 2012, *A&A*, 545, A59
- Štefl, S., Le Bouquin, J.-B., Carciofi, A. C., et al. 2012, *A&A*, 540, A76
- Štefl, S., Rivinius, Th., Carciofi, A. C., et al. 2009, *A&A*, 504, 929
- Tanaka, K., Sadakane, K., Narusawa, S.-Y., et al. 2007, *PASJ*, 59, L35
- Tannirkulam, A., Monnier, J. D., Millan-Gabet, R., et al. 2008, *ApJ*, 677, L51
- ten Brummelaar, T. A., McAlister, H. A., Ridgway, S. T., et al. 2005, *ApJ*, 628, 453
- Thompson, G. I., Nandy, K., Jamar, C., et al. 1978, *Catalogue of stellar ultraviolet fluxes (TD1): A compilation of absolute stellar fluxes measured by the Sky Survey Telescope (S2/68) aboard the ESRO satellite TD-1* (London: Science Research Council)
- Tokovinin, A. A. 1985, *A&AS*, 61, 483
- Tokovinin, A., Mason, B. D., & Hartkopf, W. I. 2010, *AJ*, 139, 743
- Tokovinin, A., Thomas, S., Sterzik, M., & Udry, S. 2006, *A&A*, 450, 681
- Touhami, Y. 2012, Ph.D. dissertation, Georgia State Univ.
- Touhami, Y., Gies, D. R., & Schaefer, G. H. 2011, *ApJ*, 729, 17
- Touhami, Y., Richardson, N. D., Gies, D. R., et al. 2010, *PASP*, 122, 379
- Townsend, R. H. D., Owocki, S. P., & Howarth, I. D. 2004, *MNRAS*, 350, 189
- Tycner, C., Gilbreath, G. C., Zavala, R. T., et al. 2006, *AJ*, 131, 2710
- Tycner, C., Hajian, A. R., Armstrong, J. T., et al. 2004, *AJ*, 127, 1194
- Tycner, C., Jones, C. E., Sigut, T. A. A., et al. 2008, *ApJ*, 689, 461
- Tycner, C., Lester, J. B., Hajian, A. R., et al. 2005, *ApJ*, 624, 359
- Valenti, J. A., & Fischer, D. A. 2005, *ApJS*, 159, 141
- van Leeuwen, F. 2007, *A&A*, 474, 653

Wegner, W. 1994, MNRAS, 270, 229

Wright, C. O., Egan, M. P., Kraemer, K. E., & Price, S. D. 2003, AJ, 125, 359

Young, A. T. 1974, ApJ, 189, 587

Yudin, R. V. 2001, A&A, 368, 912

Zhuchkov, R. Y., Malogolovets, E. V., Kiyeva, O. V., et al. 2010, Astron. Rep., 54, 1134

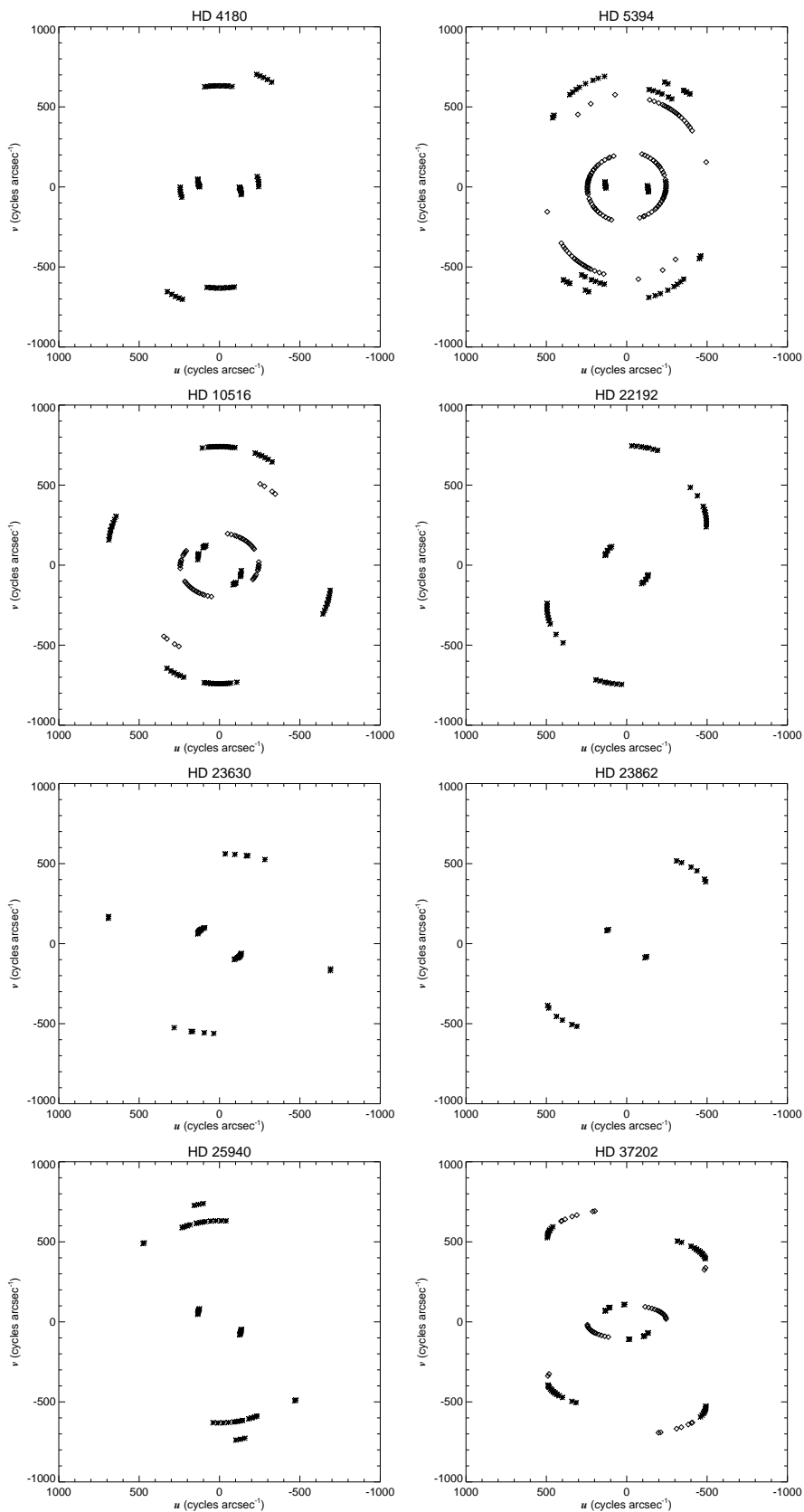


Fig. 1.— 1.1 – 1.8. Sampling of the frequency  $(u, v)$  plane for our Be star sample. Observations conducted in this survey are indicated by star symbols while archived measurements



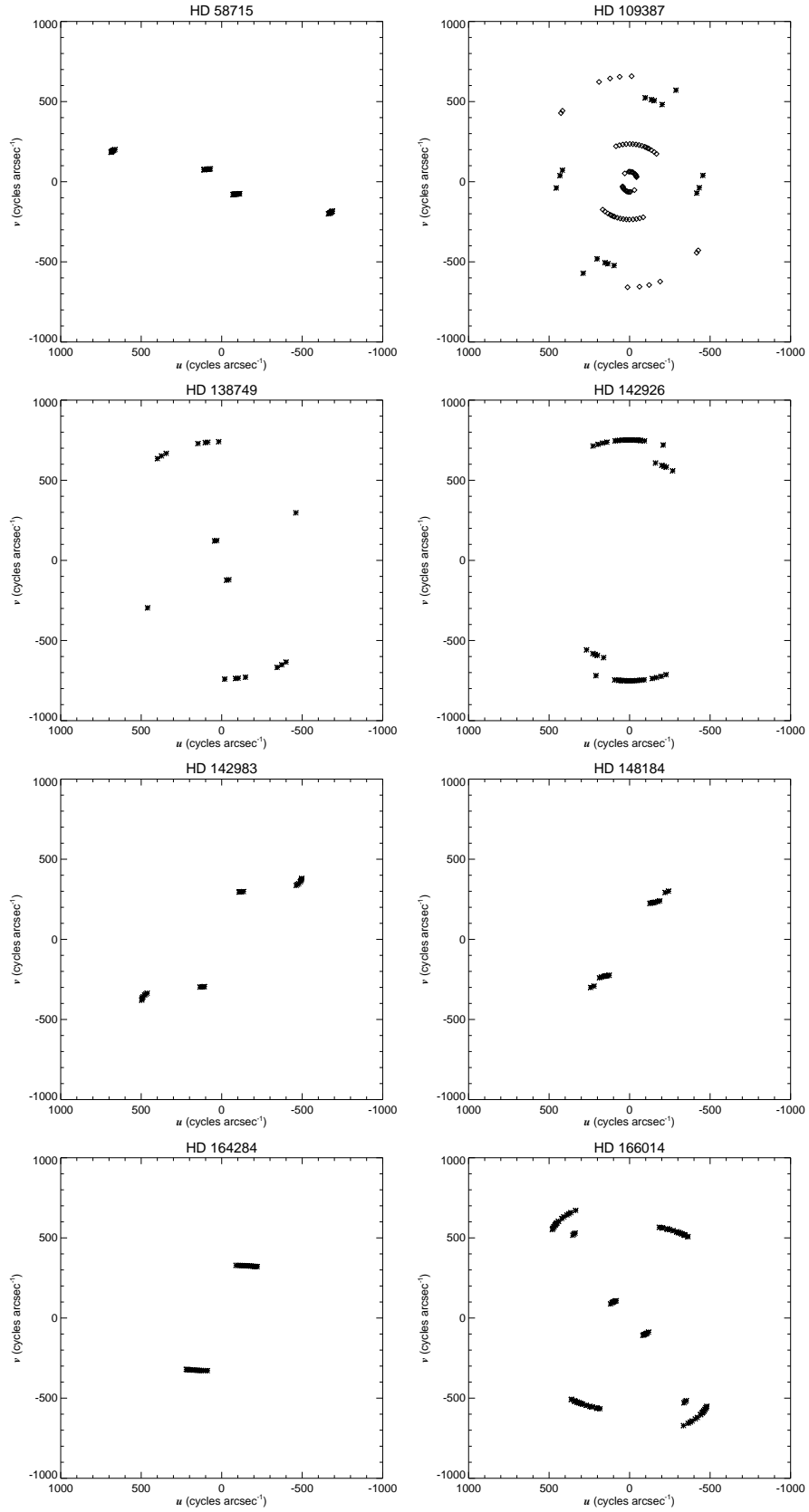


Fig. 1.— 1.9 – 1.16. Sampling of the frequency  $(u, v)$  plane for our sample stars.

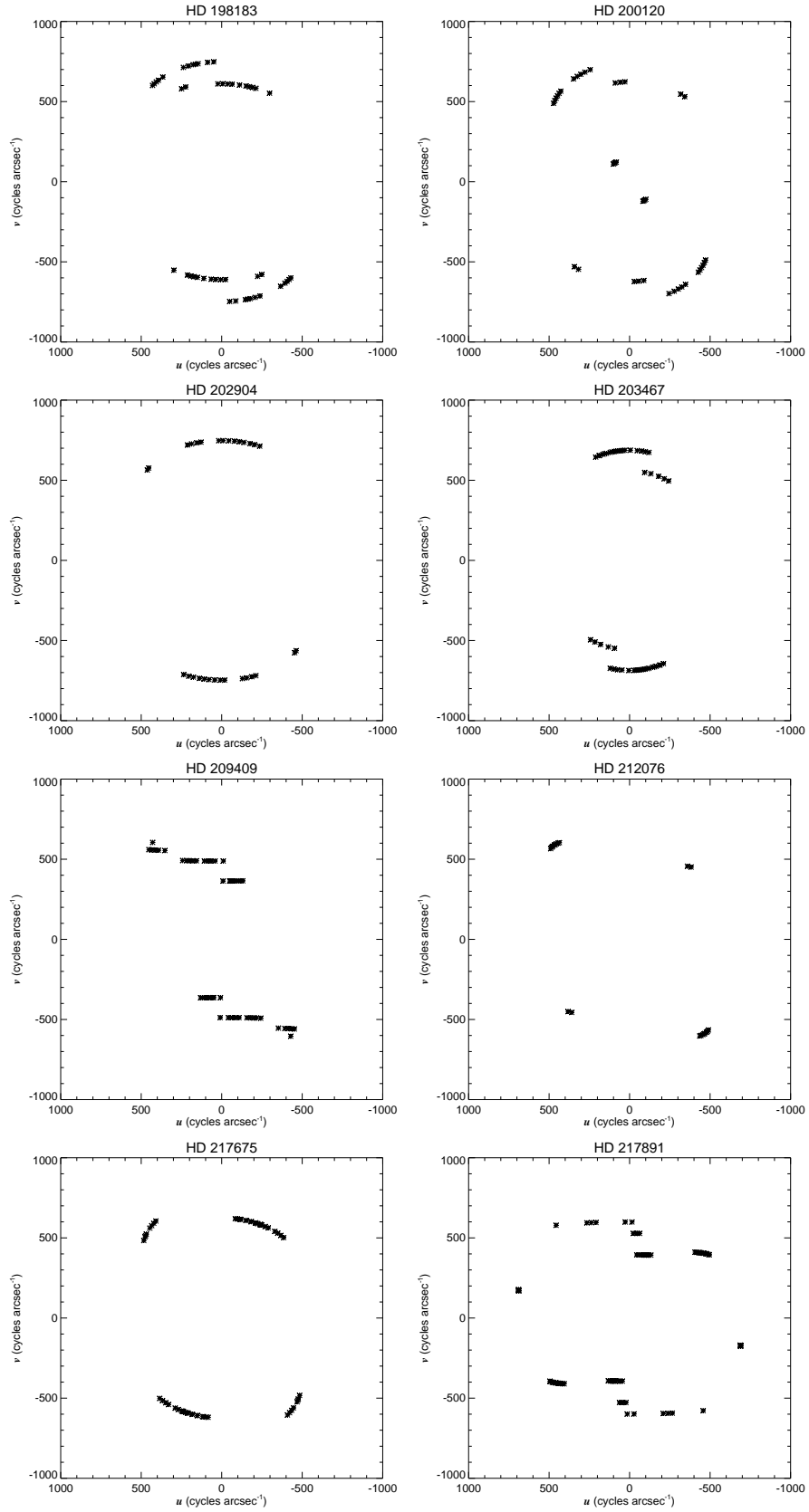


Fig. 1.— 1.17 – 1.24. Sampling of the frequency  $(u, v)$  plane for our sample stars.

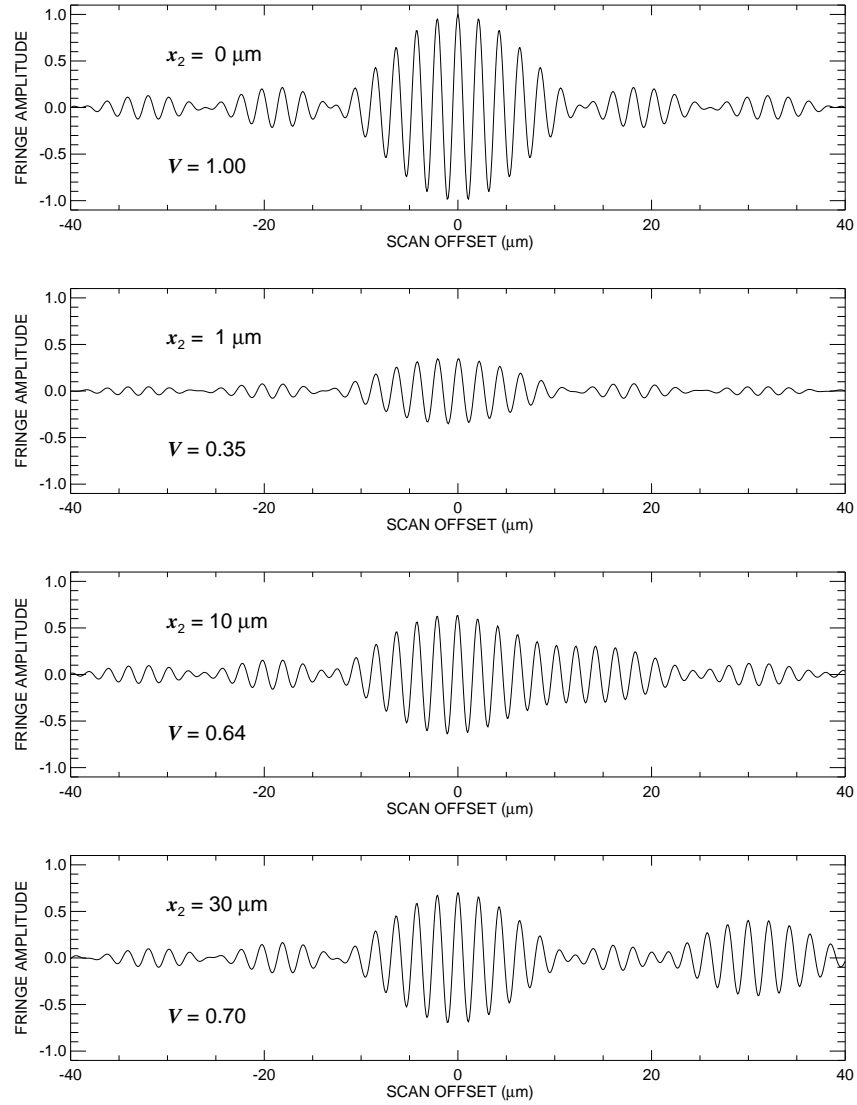


Fig. 2.— A series of combined fringe patterns for an assumed flux ratio of  $f_2/f_1 = 0.5$  and a projected separation of zero (upper panel),  $1 \mu\text{m}$  (second panel from the top),  $10 \mu\text{m}$  (third panel from the top), and  $30 \mu\text{m}$  (bottom panel). The  $30 \mu\text{m}$  separation would correspond to a projected angular separation of  $20.6 \text{ mas}$  for a  $300 \text{ m}$  baseline (see eq. 4).

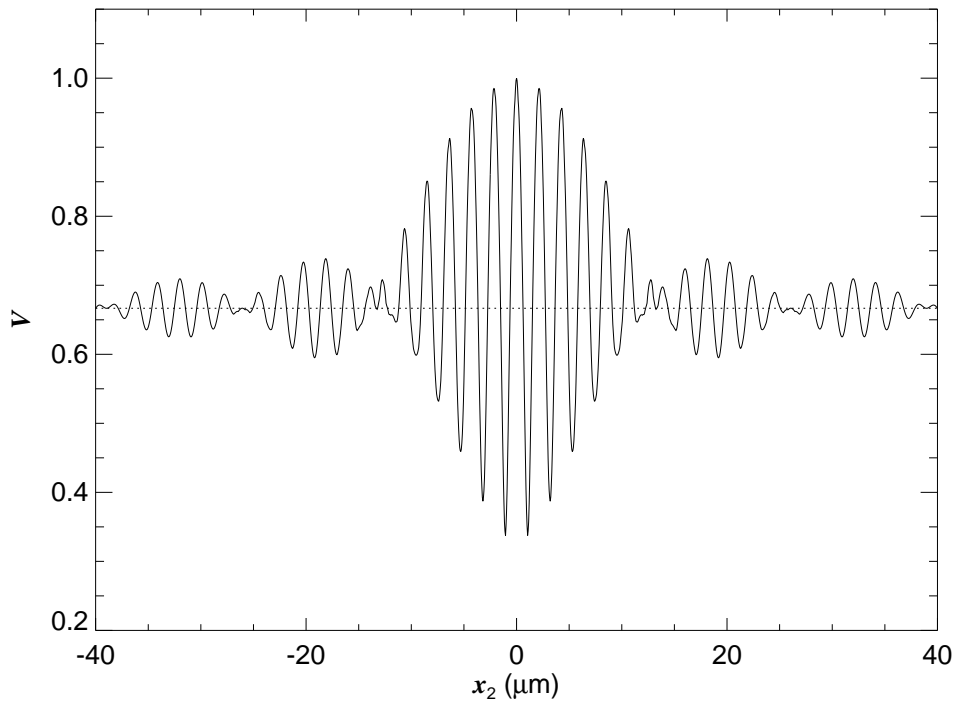


Fig. 3.— The net visibility as a function of the binary projected separation  $x_2$  for the fringe patterns shown in Fig. 2.

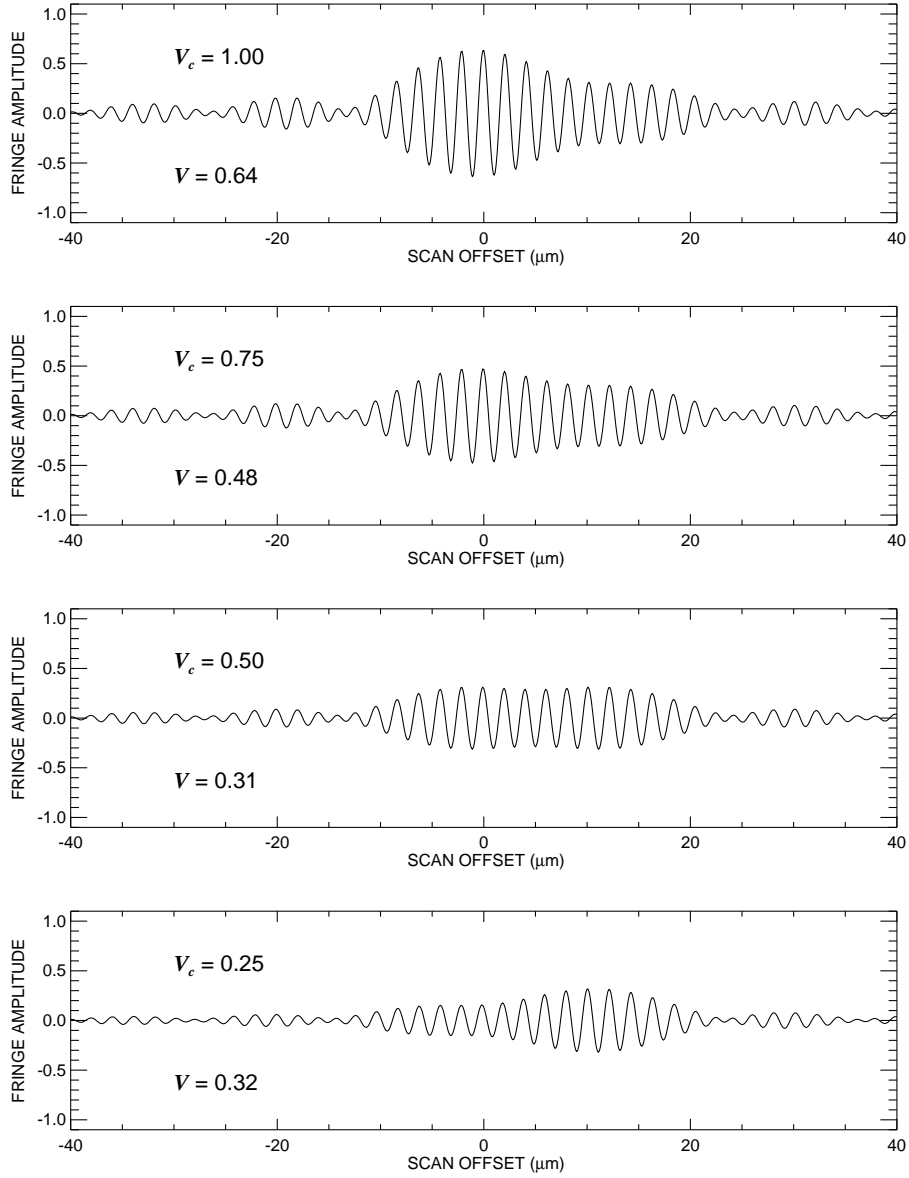


Fig. 4.— Model binary fringe patterns for  $f_2/f_1 = 0.5$  and a separation of  $10 \mu\text{m}$ . From top to bottom, the panels show the progressive appearance of the combined fringe patterns as the visibility of a star-plus-disk  $V_c$  drops from 1 to 0.25.

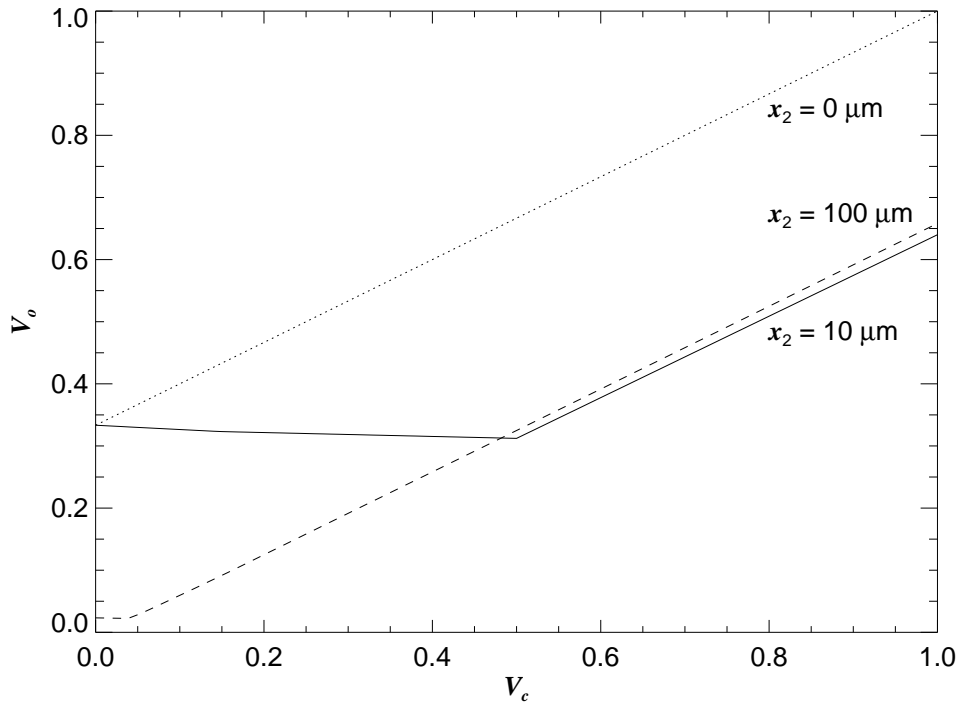


Fig. 5.— The relationship between the Be star visibility  $V_c$  and the net observed visibility  $V_o$ . The various lines show the predictions for three binary separation values  $x_2$  (see Fig. 4 for the  $x_2 = 10 \mu\text{m}$  case).

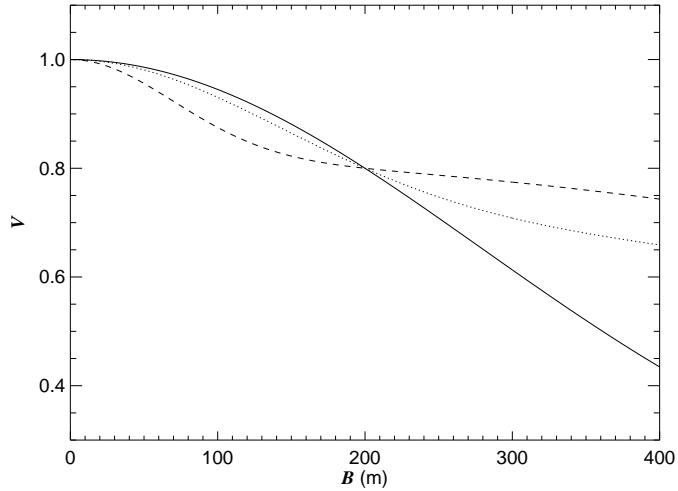


Fig. 6.— A set of three Gaussian elliptical models of different  $(c_p, \theta_{\text{maj}})$  that produce a visibility point  $V = 0.8$  at a 200 m projected baseline. The solid curve is for  $(c_p, \theta_{\text{maj}}) = (0.156, 0.6 \text{ mas})$ , the dotted curve is for  $(c_p, \theta_{\text{maj}}) = (0.719, 1.2 \text{ mas})$ , and the dashed curve is for  $(c_p, \theta_{\text{maj}}) = (0.816, 2.4 \text{ mas})$ .

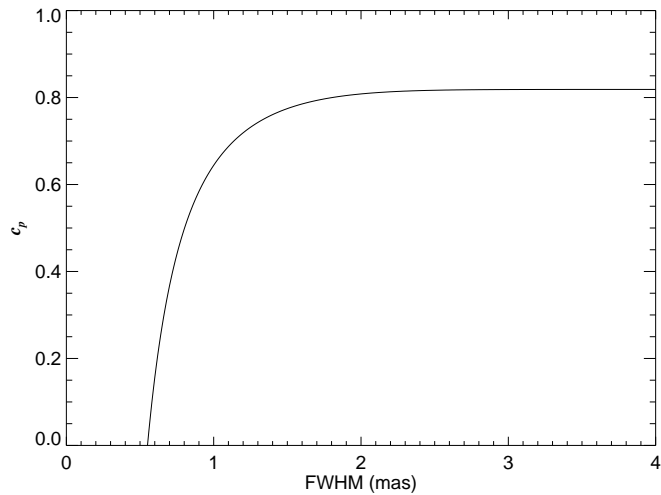


Fig. 7.— The relation between  $c_p$  and  $\theta_{\text{maj}} = \text{FWHM}$  for Gaussian elliptical visibility models that go through the same observed point of  $V = 0.8$  at a 200 m baseline.

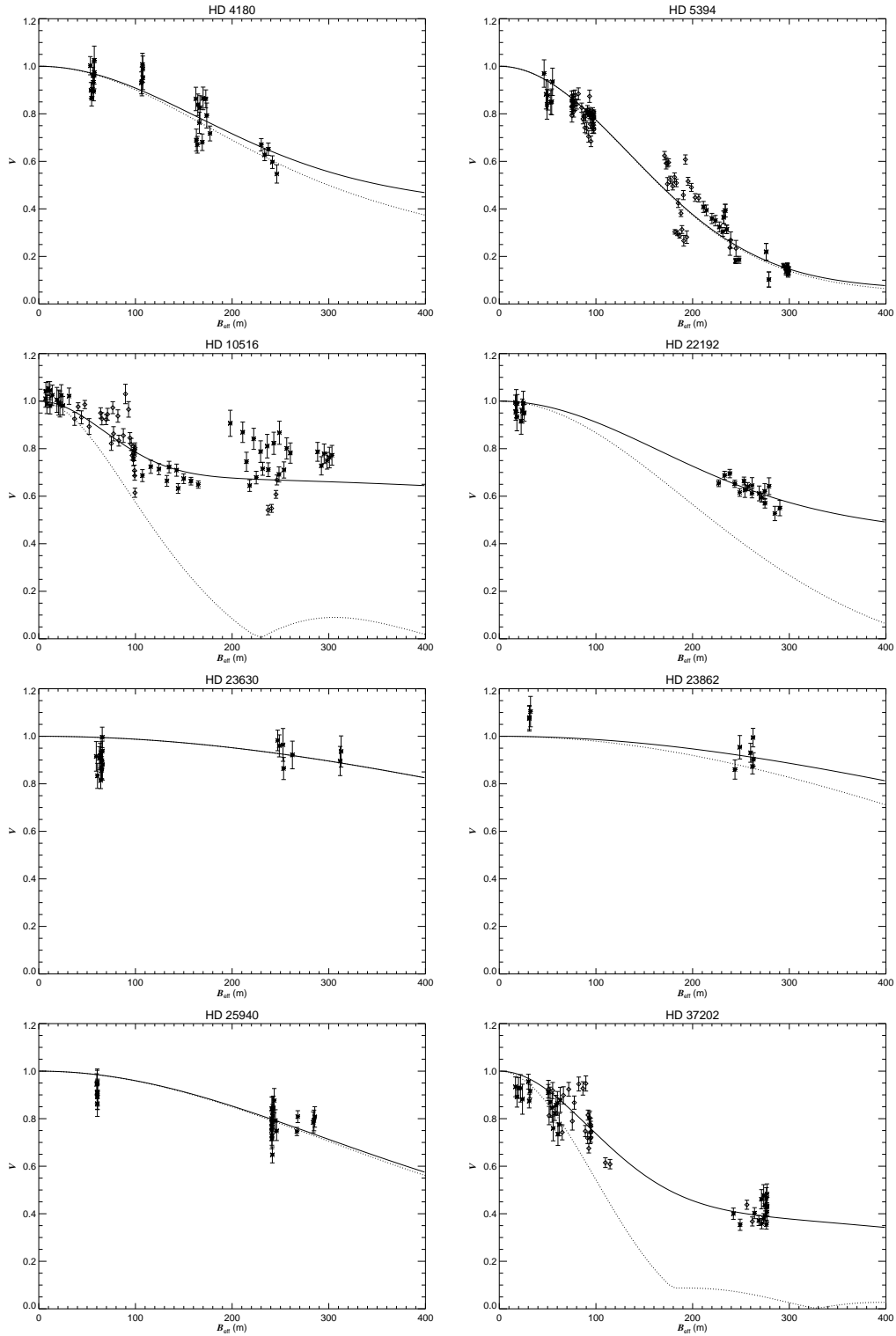


Fig. 8.— 8.1 – 8.8. Calibrated visibilities versus the effective baseline. The solid line and the dotted lines represent the Gaussian elliptical model along the major and minor axes, respectively, and the star signs represent the interferometric data.



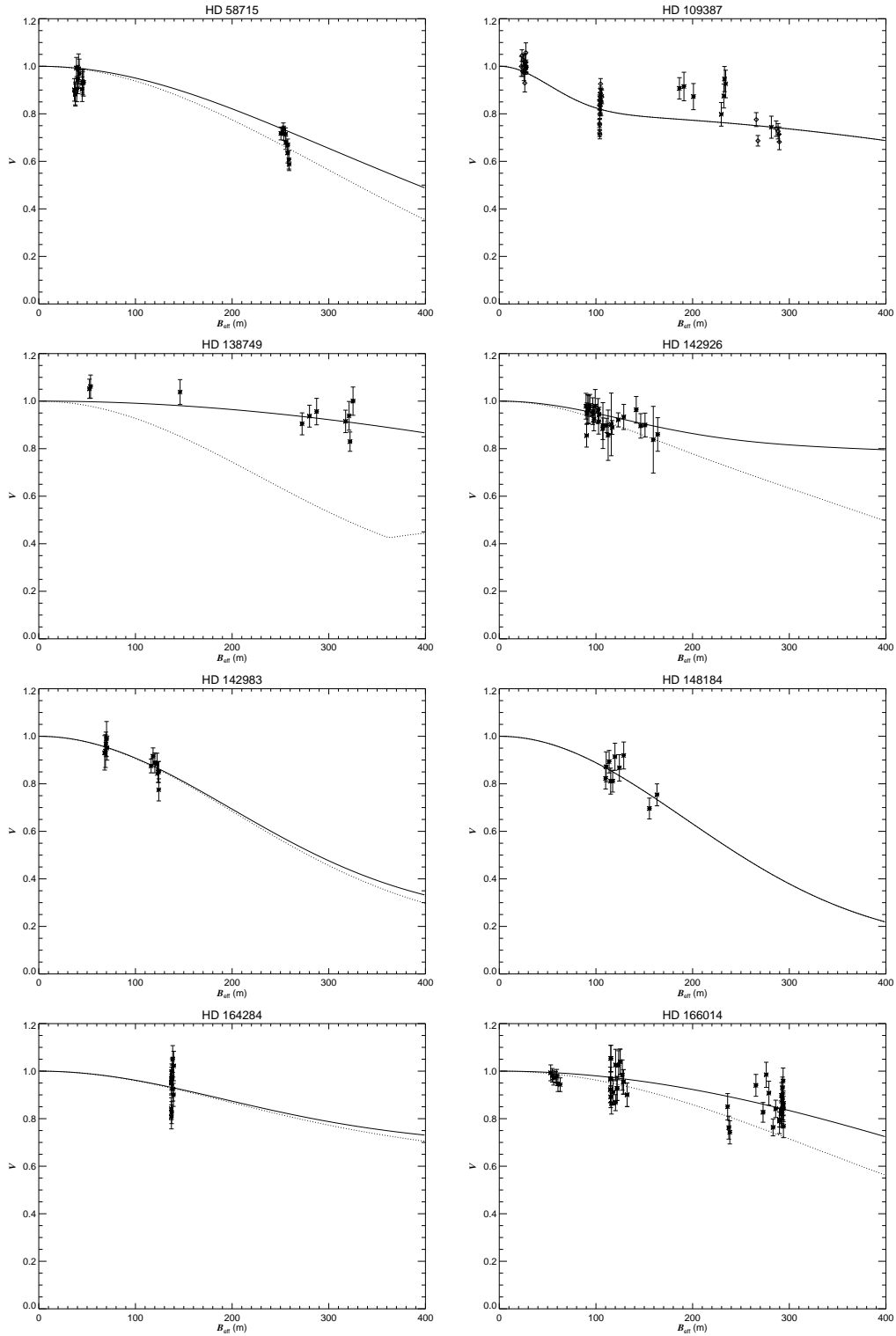


Fig. 8.— 8.9 – 8.16. Calibrated visibilities versus the effective baseline. The solid and the dotted lines represent the Gaussian elliptical model along the major and minor axes, respectively, and the star signs represent the interferometric data.

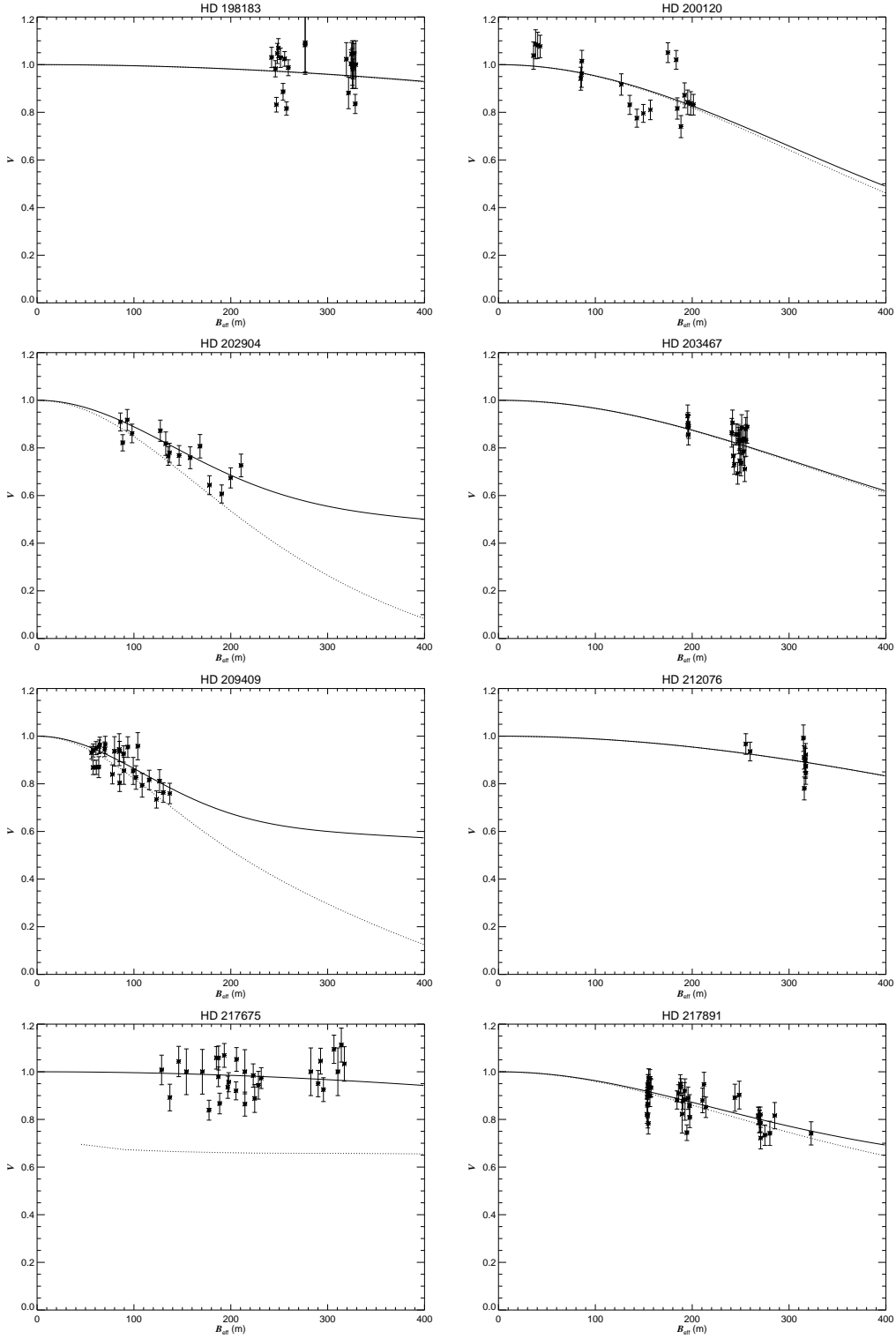


Fig. 8.— 8.17 – 8.24. Calibrated visibilities versus the effective baseline. The solid line and the dotted lines represent the Gaussian elliptical model along the major and minor axes, respectively, and the star signs represent the interferometric data.

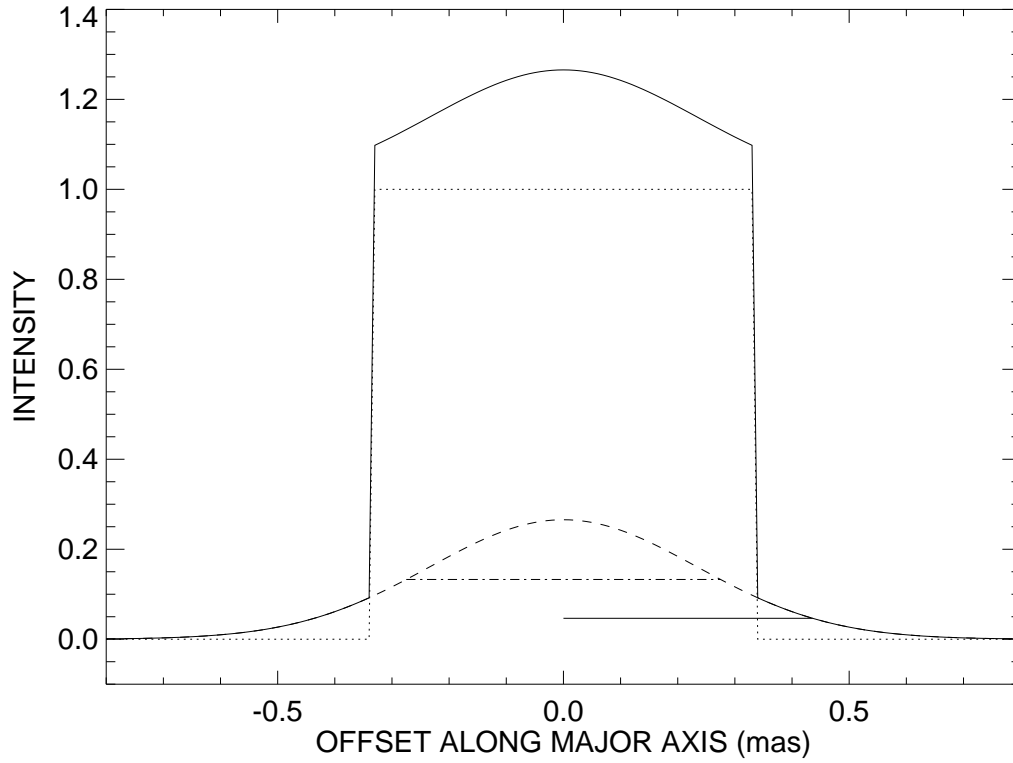


Fig. 9.— A set of intensity profiles for a faint disk case. The diagram shows the stellar (uniform disk) flux (dotted line), the Gaussian circumstellar disk flux (dashed line), and their sum (upper solid line). In this case the Gaussian FWHM (indicated by the dashed-dotted line) is smaller than the stellar diameter, and the revised circumstellar disk radius (from eq. 21) is shown as lower solid line on the right side.

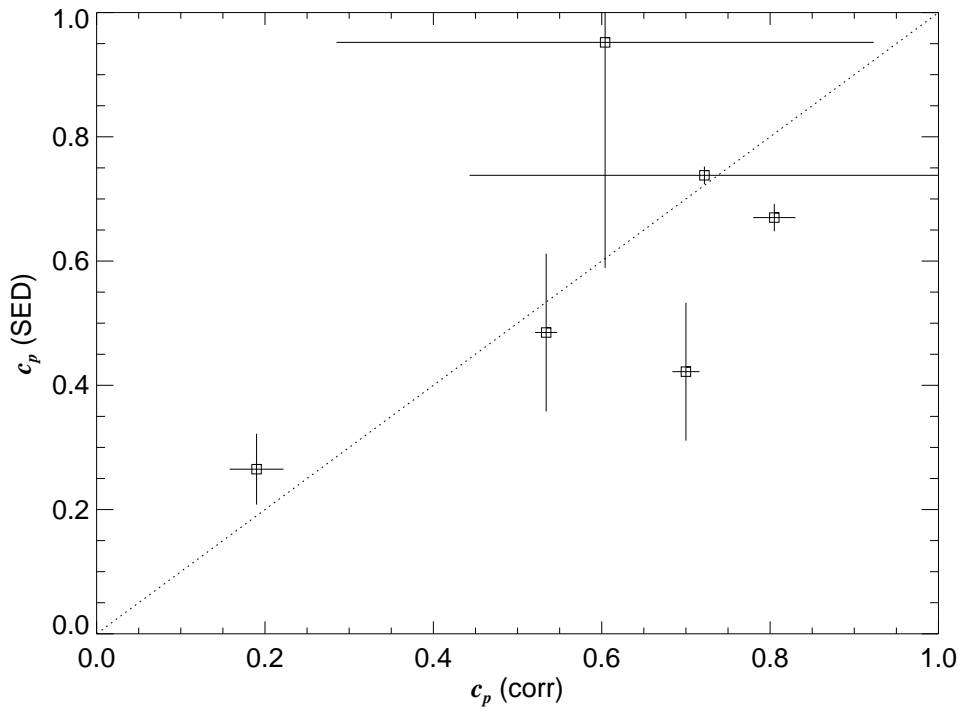


Fig. 10.— A comparison between the values of the  $K$ -band photospheric contribution  $c_p(\text{SED})$  derived from the SED fits and those from the Gaussian elliptical fits  $c_p(\text{corr})$ .

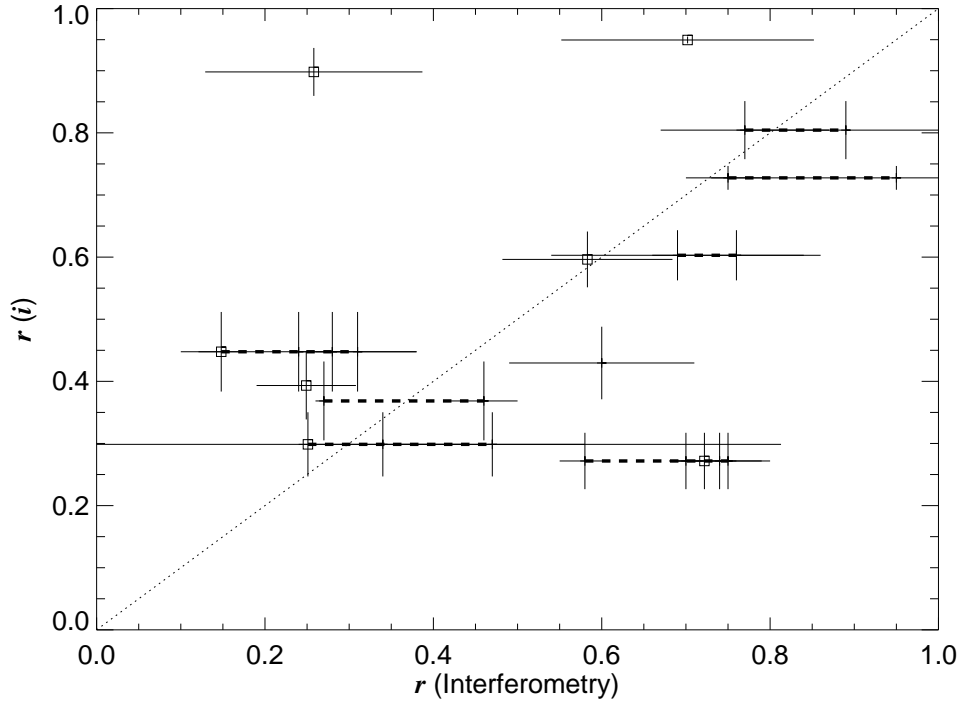


Fig. 11.— A comparison between the values of the disk axial ratio  $r(i)$  adopted from the stellar inclinations given by Frémat et al. (2005) and those derived from interferometry (our estimates are indicated by square symbols while the rest are from prior work listed in Table 8). Thick dashed lines connect the various estimates from interferometry for the same star.

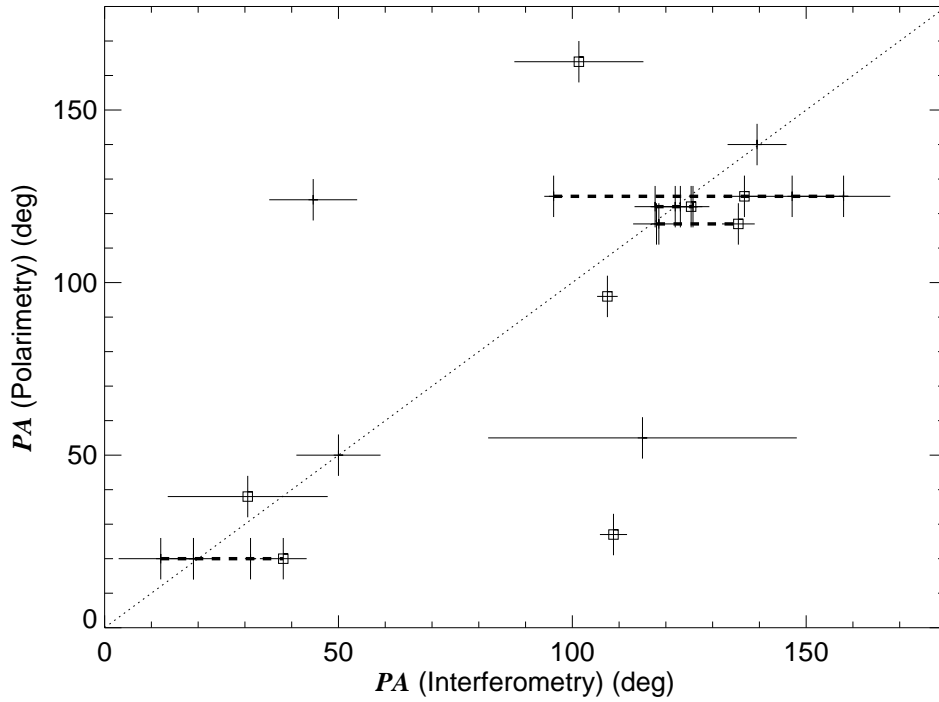


Fig. 12.— A comparison between the values of the disk long axis position angle  $PA$  adopted from the intrinsic polarization angle plus  $90^\circ$  (McDavid 1999; Yudin et al. 2001) and those derived from interferometry (our estimates are indicated by square symbols while the rest are from prior work listed in Table 8). Thick dashed lines connect the various estimates from interferometry for the same star.

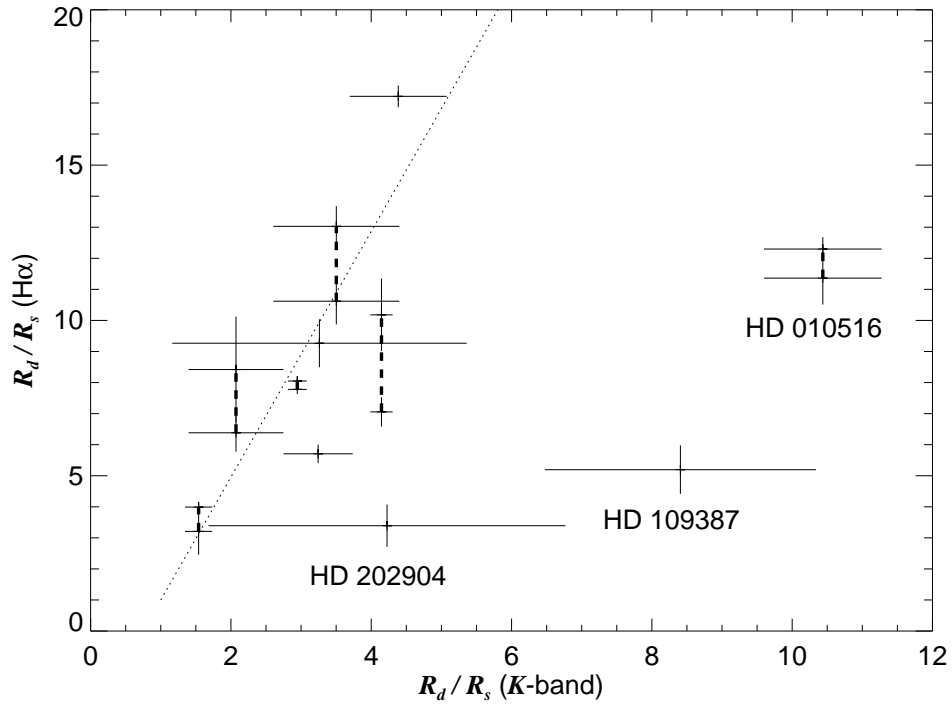


Fig. 13.— A comparison of the  $K$ -band disk sizes with the  $H\alpha$  disk sizes ( $R_d/R_s = \theta_{\text{maj}}/\theta_s$  with  $\theta_{\text{maj}}$  from Table 8 and  $\theta_s$  from Table 7). The dotted line represents a linear fit to the data with a slope of 4.0. Thick dashed lines connect multiple  $H\alpha$  measurements for the same star.

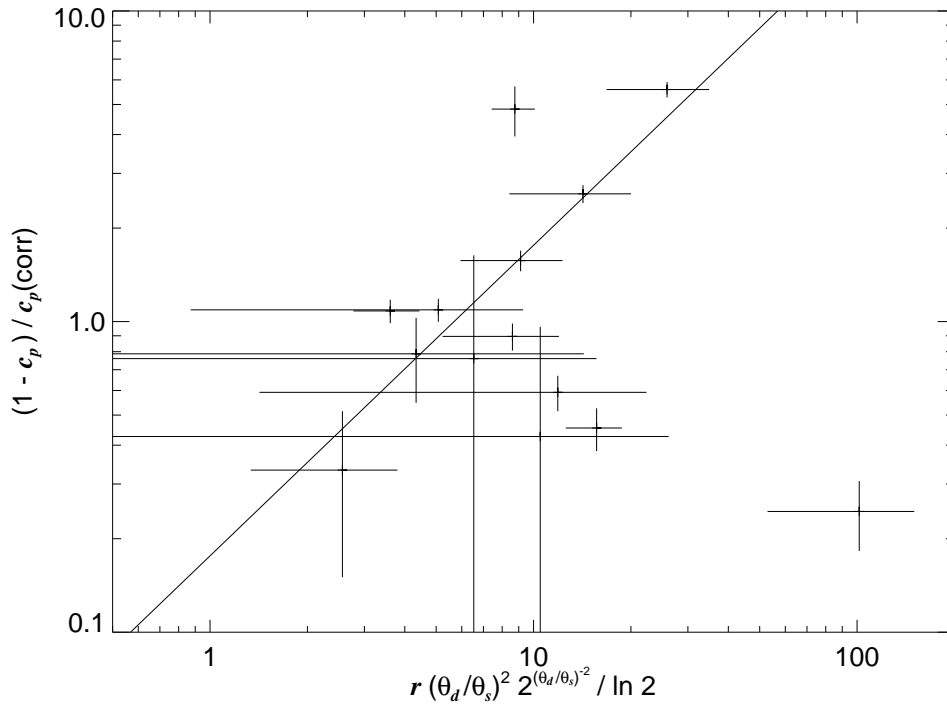


Fig. 14.— A plot of the approximate disk to star flux ratio  $F_d/F_s = (1 - c_p)/c_p(\text{corr})$  as a function of a product related to the projected disk to stellar area on the sky. A linear relationship (unit slope line) may exist for large optically thick disks. The scatter is largest among faint disk systems (the lower, right point represents  $\kappa$  Dra = HD 109387).



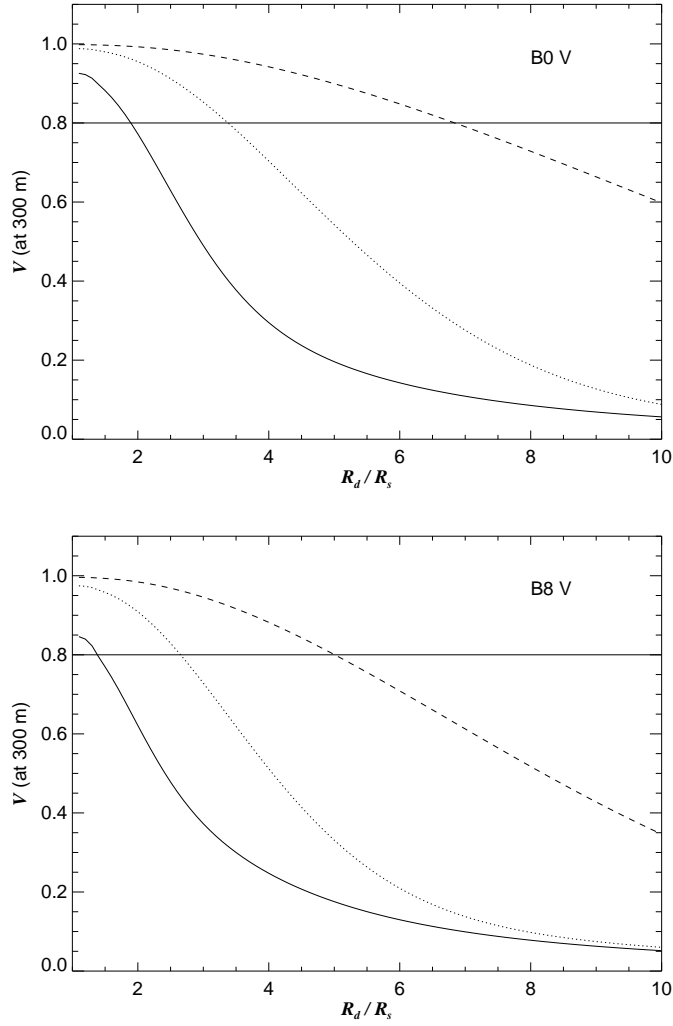


Fig. 15.— A plot of the expected calibrated visibility measured at a baseline of 300 m for a Be star of type B0 V (*above*) and B8 V (*below*) as a function of disk to stellar radius along the major axis. The thick solid, dotted, and dashed lines correspond to predictions for a star of visual magnitude 3, 5, and 7, respectively. The thin horizontal line marks the  $V = 0.8$  criterion, and if the visibility drops below this line then the disk is detected with some confidence.

Table 1. Adopted Stellar Parameters

HD Number	Star Name	Spectral Class.	$T_{\text{eff}}$ (K)	$\log g$ ( $\text{cm s}^{-2}$ )	$PA$ (deg)	$r$
HD 004180	<i>o</i> Cas	B2 Ve	14438	3.284	164	0.582
HD 005394	$\gamma$ Cas	B0 IVe	26431	3.800	20	0.764
HD 010516	$\phi$ Per	B0.5 IVe	25556	3.899	117	0.322
HD 022192	$\psi$ Per	B4.5 Ve	15767	3.465	125	0.280
HD 023630	$\eta$ Tau	B5 IIIe	12258	3.047	124	0.727
HD 023862	28 Tau	B8 Vpe	12106	3.937	159	0.438
HD 025940	48 Per	B4 Ve	16158	3.572	55	0.798
HD 037202	$\zeta$ Tau	B1 IVe	19310	3.732	122	0.071
HD 058715	$\beta$ CMi	B8 Ve	11772	3.811	140	0.779
HD 109387	$\kappa$ Dra	B6 IIIpe	13982	3.479	102	0.660
HD 138749	$\theta$ CrB	B6Vnne	14457	3.745	177	0.200
HD 142926	4 Her	B9 pe	12076	3.917	70	0.300
HD 142983	48 Lib	B3 IVe	15000	3.500	50	0.405
HD 148184	$\chi$ Oph	B1.5 Vpe	28783	3.913	20	0.947
HD 164284	66 Oph	B2 IV	21609	3.943	18	0.685
HD 166014	<i>o</i> Her	B9.5 III	9800	3.500	89	0.868
HD 198183	$\lambda$ Cyg	B5 Ve	13925	3.167	30	0.826
HD 200120	59 Cyg	B1.5 Ve	21750	3.784	95	0.310
HD 202904	<i>v</i> Cyg	B2.5 Vne	19100	3.900	27	0.887
HD 203467	6 Cep	B2.5 Ve	17087	3.377	76	0.799
HD 209409	<i>o</i> Aqr	B7 IVe	12942	3.701	96	0.364
HD 212076	31 Peg	B1.5 Vne	12942	3.701	148	0.955
HD 217675	<i>o</i> And	B6 IIIpe	14052	3.229	25	0.022
HD 217891	$\beta$ Psc	B5 Ve	14359	3.672	38	0.943

Table 2. Calibrator star angular diameters

Calibrator HD Number (1)	Object HD Number (2)	$T_{\text{eff}}$ (K) (3)	Ref. (4)	$\log g$ ( $\text{cm s}^{-2}$ ) (5)	Ref. (6)	Spectral Class. (7)	$E(B - V)$ (mag) (8)	Ref. (9)	$\theta_{\text{LD}}$ (mas) (10)	$\theta_{\text{UD}}$ (mas) (11)
HD 004222	HD 004180	8970	1	4.20	2	A2 V	0.009	3	$0.303 \pm 0.017$	$0.301 \pm 0.021$
HD 006210	HD 005394	6065	4	3.86	4	F6 V	0.009	5	$0.516 \pm 0.025$	$0.506 \pm 0.035$
HD 011151	HD 010516	6405	6	4.00	6	F5 V	0.003	7	$0.424 \pm 0.011$	$0.416 \pm 0.029$
HD 020675	HD 022192	6577	6	4.28	6	F6 V	0.006	7	$0.418 \pm 0.018$	$0.417 \pm 0.028$
HD 024167	HD 023630	8200	1	4.01	8	A5 V	0.016	8	$0.246 \pm 0.015$	$0.243 \pm 0.017$
HD 024357	HD 023862	6890	1	4.30	2	F4 V	0.008	8	$0.374 \pm 0.014$	$0.368 \pm 0.026$
HD 025948	HD 025940	6440	1	4.07	8	F5 V	0.008	7	$0.374 \pm 0.014$	$0.367 \pm 0.025$
HD 037147	HD 037202	7200	1	4.13	8	F0 V	0.003	8	$0.403 \pm 0.021$	$0.397 \pm 0.028$
HD 057006	HD 058715	6166	9	3.77	9	F8 V	0.001	7	$0.501 \pm 0.031$	$0.491 \pm 0.034$
HD 111456	HD 109387	6313	10	4.70	10	F6 V	0.000	7	$0.477 \pm 0.028$	$0.467 \pm 0.033$
HD 142640	HD 142983	6481	4	4.09	4	F6 V	0.005	7	$0.363 \pm 0.013$	$0.356 \pm 0.025$
HD 144585	HD 148184	5831	11	4.03	11	G5 V	0.005	7	$0.438 \pm 0.012$	$0.429 \pm 0.030$
HD 159139	HD 166014	9550	2	4.17	2	A1 V	0.023	8	$0.248 \pm 0.013$	$0.246 \pm 0.017$
HD 161941	HD 164284	10512	12	3.67	12	B9.5 V	0.180	3	$0.194 \pm 0.037$	$0.194 \pm 0.014$
HD 166233	HD 164284	6661	12	3.57	12	F2 V	0.003	7	$0.405 \pm 0.026$	$0.398 \pm 0.027$
HD 168914	HD 166014	7600	2	4.20	2	A7 V	0.000	13	$0.456 \pm 0.023$	$0.450 \pm 0.031$
HD 192455	HD 203467	6251	4	4.05	4	F5 V	0.003	7	$0.504 \pm 0.026$	$0.494 \pm 0.035$
HD 196629	HD 198183	6996	14	4.25	15	F0 V	0.007	8	$0.285 \pm 0.010$	$0.280 \pm 0.020$
HD 203454	HD 202904	6146	16	4.50	16	F8 V	0.001	8	$0.406 \pm 0.025$	$0.398 \pm 0.028$
HD 211575	HD 209409	6300	17	4.00	17	F3 V	0.006	7	$0.367 \pm 0.024$	$0.360 \pm 0.025$
HD 213617	HD 212076	7259	18	4.40	18	F1 V	0.017	8	$0.278 \pm 0.010$	$0.274 \pm 0.019$
HD 217877	HD 217891	5953	6	4.29	6	F8 V	0.003	7	$0.365 \pm 0.149$	$0.358 \pm 0.025$
HD 217926	HD 217891	6528	14	3.63	8	F2 V	0.005	7	$0.335 \pm 0.013$	$0.329 \pm 0.023$
HD 218470	HD 217675	6407	19	4.07	19	F5 V	0.004	7	$0.491 \pm 0.028$	$0.482 \pm 0.033$

References. — 1. Wright et al. (2003); 2. Lafrasse et al. (2010); 3. from  $B - V$  and spectral classification; 4. Balachandran (1990); 5. Karataş & Schuster (2006); 6. Valenti & Fischer (2005); 7. Ammons et al. (2006); 8. Philip & Egret (1980); 9. da Silva et al. (2011); 10. Schröder et al. (2009); 11. Edvardsson et al. (1993); 12. Prugniel & Soubiran (2001); 13. Gray et al. (2001); 14. Masana et al. (2006); 15. Allende Prieto & Lambert (1999); 16. Boesgaard & Friel (1990); 17. Boesgaard & Tripicco (1986); 18. Gerbaldi et al. (2007); 19. Fuhrmann (1998)

Table 3. Calibrated Visibilities

HD Number (1)	Date (HJD-2400000) (2)	Telescope Pair (3)	$u$ (cycles arcsec <sup>-1</sup> ) (4)	$v$ (cycles arcsec <sup>-1</sup> ) (5)	Baseline (m) (6)	Effective baseline (m) (7)	$V$ (8)	$\delta V$ (9)	$V_c$ (10)	$\delta V_c$ (11)
HD 004180	54756.622	S1/W1	-75.187	-627.643	278.114	162.970	0.705	0.042	0.689	0.046
HD 004180	54756.629	S1/W1	-44.906	-630.398	278.055	164.379	0.693	0.042	0.838	0.045
HD 004180	54756.637	S1/W1	-15.062	-631.747	278.024	166.438	0.821	0.047	0.826	0.051
HD 004180	54756.649	S1/W1	19.818	-631.622	278.027	169.637	0.736	0.044	0.865	0.048
HD 004180	54756.661	S1/W1	52.167	-629.866	278.067	173.303	0.767	0.048	0.793	0.053
HD 004180	54757.610	S1/W1	-91.896	-625.513	278.157	162.450	0.812	0.045	0.863	0.049
HD 004180	54757.626	S1/W1	-53.847	-629.731	278.070	163.890	0.569	0.032	0.670	0.035
HD 004180	54757.633	S1/W1	-21.944	-631.555	278.029	165.906	0.724	0.041	0.762	0.045
HD 004180	54757.645	S1/W1	11.396	-631.820	278.023	168.790	0.609	0.032	0.680	0.035
HD 004180	54757.657	S1/W1	44.336	-630.437	278.054	172.357	0.790	0.035	0.863	0.038
HD 004180	54757.665	S1/W1	77.830	-627.335	278.120	176.648	0.668	0.029	0.717	0.031
HD 004180	54759.958	S1/E1	230.947	-702.578	325.380	229.379	0.609	0.024	0.670	0.026
HD 004180	54759.965	S1/E1	251.849	-693.810	324.740	232.929	0.577	0.022	0.627	0.024
HD 004180	54759.973	S1/E1	273.565	-683.594	323.945	236.659	0.596	0.024	0.651	0.026
HD 004180	54759.985	S1/E1	297.619	-670.821	322.880	240.810	0.552	0.024	0.597	0.027
HD 004180	54759.993	S1/E1	324.424	-654.529	321.402	245.410	0.498	0.035	0.547	0.038
HD 004180	54767.629	E1/E2	122.971	0.450	54.103	53.424	0.948	0.035	1.002	0.038
HD 004180	54767.637	E1/E2	124.960	3.844	55.004	54.111	0.861	0.030	0.899	0.033
HD 004180	54767.641	E1/E2	126.845	7.417	55.902	54.758	0.837	0.030	0.865	0.033
HD 004180	54767.649	E1/E2	128.894	11.841	56.948	55.457	0.876	0.028	0.903	0.030
HD 004180	54767.657	E1/E2	130.759	16.587	57.990	56.086	0.934	0.032	0.961	0.035
HD 004180	54767.665	E1/E2	131.999	20.340	58.760	56.500	0.910	0.035	0.933	0.038
HD 004180	54767.668	E1/E2	133.025	24.046	59.475	56.838	0.875	0.035	0.893	0.039
HD 004180	54767.692	E1/E2	135.194	38.016	61.787	57.521	0.946	0.045	0.974	0.049
HD 004180	54767.700	E1/E2	135.336	42.509	62.411	57.550	0.990	0.055	1.025	0.060
HD 004180	54767.708	E1/E2	135.106	48.520	63.159	57.450	0.924	0.050	0.960	0.055
HD 004180	55130.751	W1/W2	-234.308	64.271	106.895	106.693	0.935	0.055	0.936	0.060
HD 004180	55130.766	W1/W2	-240.004	47.195	107.615	107.615	0.952	0.051	0.988	0.055
HD 004180	55130.778	W1/W2	-243.174	31.895	107.904	107.769	0.871	0.046	0.952	0.050
HD 004180	55130.794	W1/W2	-244.593	16.546	107.858	107.308	0.872	0.043	1.007	0.047
HD 004180	55130.805	W1/W2	-244.315	1.671	107.492	106.283	0.772	0.042	0.930	0.046
HD 005394	54754.703	S1/W1	139.084	-607.765	274.306	231.158	0.303	0.019	...	...
HD 005394	54754.711	S1/W1	165.175	-600.436	273.983	227.589	0.324	0.021	...	...

Table 3—Continued

HD Number (1)	Date (HJD-2400000) (2)	Telescope Pair (3)	$u$ (cycles arcsec <sup>-1</sup> ) (4)	$v$ (cycles arcsec <sup>-1</sup> ) (5)	Baseline (m) (6)	Effective baseline (m) (7)	$V$ (8)	$\delta V$ (9)	$V_c$ (10)	$\delta V_c$ (11)
HD 005394	54754.722	S1/W1	194.453	-590.507	273.525	223.502	0.350	0.022	...	...
HD 005394	54754.730	S1/W1	219.570	-580.451	273.038	219.937	0.360	0.022	...	...
HD 005394	54754.746	S1/W1	259.566	-561.204	272.040	214.171	0.394	0.022	...	...
HD 005394	54754.754	S1/W1	280.443	-549.397	271.385	211.130	0.408	0.023	...	...
HD 005394	54758.765	S1/E1	-354.366	-576.322	297.658	296.711	0.135	0.013	...	...
HD 005394	54758.773	S1/E1	-335.716	-592.279	299.530	297.903	0.145	0.011	...	...
HD 005394	54758.781	S1/E1	-314.532	-608.507	301.370	298.796	0.124	0.011	...	...
HD 005394	54758.789	S1/E1	-294.521	-622.229	302.876	299.257	0.132	0.010	...	...
HD 005394	54758.804	S1/E1	-255.926	-644.924	305.268	299.276	0.147	0.011	...	...
HD 005394	54758.968	S1/E1	235.831	-655.016	306.292	248.023	0.186	0.015	...	...
HD 005394	54758.976	S1/E1	256.817	-644.451	305.219	244.459	0.181	0.011	...	...
HD 005394	54760.816	S1/E1	-210.001	-666.447	307.424	298.080	0.163	0.010	...	...
HD 005394	54760.828	S1/E1	-177.144	-678.694	308.604	296.556	0.151	0.008	...	...
HD 005394	54760.840	S1/E1	-137.760	-690.286	309.689	294.109	0.161	0.010	...	...
HD 005394	54766.656	E1/E2	127.804	-7.489	56.326	48.422	0.969	0.058	...	...
HD 005394	54766.668	E1/E2	130.796	1.022	57.547	49.382	0.882	0.062	...	...
HD 005394	54766.672	E1/E2	131.950	5.101	58.097	50.392	0.840	0.062	...	...
HD 005394	54766.680	E1/E2	132.995	9.479	58.661	53.292	0.877	0.061	...	...
HD 005394	54766.699	E1/E2	134.968	22.648	60.211	54.232	0.848	0.050	...	...
HD 005394	54766.703	E1/E2	135.250	27.140	60.691	55.091	0.850	0.054	...	...
HD 005394	55116.718	S1/E1	-459.951	-432.035	277.633	276.146	0.219	0.036	...	...
HD 005394	55116.726	S1/E1	-453.050	-446.835	279.962	278.908	0.103	0.032	...	...
HD 005394	55153.031	E1/W1	-372.570	592.870	308.070	233.694	0.393	0.027	...	...
HD 005394	55153.039	E1/W1	-393.023	580.994	308.609	232.103	0.364	0.027	...	...
HD 005394	55154.023	E1/W1	-354.456	602.648	307.604	235.204	0.314	0.018	...	...
HD 010516	54759.000	S1/E1	222.132	-699.878	323.058	288.495	0.753	0.038	0.787	0.040
HD 010516	54759.008	S1/E1	244.525	-690.563	322.307	292.424	0.718	0.036	0.728	0.038
HD 010516	54759.012	S1/E1	262.220	-682.355	321.615	295.266	0.778	0.039	0.778	0.041
HD 010516	54759.020	S1/E1	282.941	-671.709	320.675	298.271	0.759	0.033	0.749	0.035
HD 010516	54759.032	S1/E1	302.160	-660.737	319.655	300.718	0.773	0.041	0.763	0.043
HD 010516	54759.040	S1/E1	327.099	-644.721	318.072	303.338	0.774	0.039	0.772	0.042
HD 010516	54759.907	S1/E1	-48.629	-738.941	325.810	218.245	0.661	0.023	0.645	0.025
HD 010516	54759.915	S1/E1	-27.475	-740.209	325.889	225.058	0.682	0.025	0.678	0.026

Table 3—Continued

HD Number (1)	Date (HJD-2400000) (2)	Telescope Pair (3)	$u$ (cycles arcsec <sup>-1</sup> ) (4)	$v$ (cycles arcsec <sup>-1</sup> ) (5)	Baseline (m) (6)	Effective baseline (m) (7)	$V$ (8)	$\delta V$ (9)	$V_c$ (10)	$\delta V_c$ (11)
HD 010516	54759.918	S1/E1	-6.288	-740.771	325.924	231.666	0.698	0.026	0.715	0.027
HD 010516	54759.926	S1/E1	13.171	-740.665	325.917	237.546	0.674	0.027	0.711	0.029
HD 010516	54759.930	S1/E1	31.856	-740.004	325.876	248.579	0.659	0.030	1.000	0.100
HD 010516	54759.938	S1/E1	51.441	-738.719	325.796	253.709	0.618	0.030	0.692	0.032
HD 010516	54759.946	S1/E1	70.139	-736.921	325.683	214.956	0.623	0.032	0.710	0.034
HD 010516	54760.899	S1/E1	-58.610	-738.096	325.757	222.431	0.748	0.038	0.745	0.040
HD 010516	54760.907	S1/E1	-35.711	-739.799	325.864	229.572	0.819	0.042	0.841	0.044
HD 010516	54760.915	S1/E1	-13.076	-740.667	325.917	236.415	0.743	0.043	0.788	0.045
HD 010516	54760.922	S1/E1	9.379	-740.733	325.921	243.200	0.740	0.047	0.811	0.049
HD 010516	54760.930	S1/E1	32.475	-739.973	325.874	248.976	0.733	0.044	0.823	0.047
HD 010516	54760.938	S1/E1	52.866	-738.602	325.789	256.563	0.767	0.046	0.867	0.049
HD 010516	54760.946	S1/E1	80.824	-735.640	325.602	260.335	0.708	0.042	0.801	0.045
HD 010516	54760.950	S1/E1	95.289	-733.607	325.472	263.227	0.698	0.040	0.781	0.043
HD 010516	54769.723	E1/E2	135.096	34.364	61.330	31.328	0.912	0.032	1.021	0.034
HD 010516	54769.755	E1/E2	134.101	54.703	63.720	24.895	0.874	0.037	0.981	0.039
HD 010516	54769.762	E1/E2	133.191	59.162	64.120	23.294	0.915	0.043	1.024	0.045
HD 010516	54769.766	E1/E2	132.223	62.922	64.424	21.893	0.882	0.052	0.988	0.055
HD 010516	54769.774	E1/E2	131.148	66.438	64.682	20.541	0.888	0.050	0.994	0.053
HD 010516	54769.782	E1/E2	129.555	70.870	64.970	18.783	0.900	0.049	1.005	0.052
HD 010516	55116.910	S1/E1	-107.331	-731.650	325.344	198.200	0.809	0.052	0.907	0.055
HD 010516	55116.922	S1/E1	-70.218	-736.912	325.683	211.070	0.774	0.041	0.869	0.043
HD 010516	55128.868	E1/E2	101.151	110.159	65.798	7.388	0.992	0.035	1.041	0.037
HD 010516	55128.883	E1/E2	90.130	118.704	65.574	11.468	0.995	0.036	1.044	0.038
HD 010516	55128.895	E1/E2	84.477	122.399	65.432	13.929	0.977	0.041	1.025	0.043
HD 010516	55131.856	E1/E2	102.124	109.303	65.813	7.150	0.954	0.034	1.010	0.036
HD 010516	55131.864	E1/E2	97.846	112.933	65.741	8.407	0.934	0.038	0.988	0.040
HD 010516	55131.872	E1/E2	94.108	115.844	65.665	9.815	0.997	0.028	1.053	0.030
HD 010516	55131.876	E1/E2	89.598	119.070	65.561	11.696	0.930	0.032	0.980	0.034
HD 010516	55152.739	E1/W1	688.207	157.539	310.617	164.924	0.610	0.014	0.649	0.015
HD 010516	55152.743	E1/W1	685.155	179.254	311.589	157.372	0.611	0.015	0.663	0.016
HD 010516	55152.751	E1/W1	681.154	199.973	312.330	149.851	0.610	0.019	0.674	0.020
HD 010516	55152.758	E1/W1	676.420	219.393	312.862	142.520	0.635	0.024	0.710	0.025
HD 010516	55152.762	E1/W1	670.547	239.335	313.245	134.708	0.643	0.023	0.722	0.024

Table 3—Continued

HD Number (1)	Date (HJD-2400000) (2)	Telescope Pair (3)	$u$ (cycles arcsec <sup>-1</sup> ) (4)	$v$ (cycles arcsec <sup>-1</sup> ) (5)	Baseline (m) (6)	Effective baseline (m) (7)	$V$ (8)	$\delta V$ (9)	$V_c$ (10)	$\delta V_c$ (11)
HD 010516	55153.754	E1/W1	677.482	215.359	312.765	144.065	0.564	0.019	0.633	0.021
HD 010516	55153.762	E1/W1	668.702	244.959	313.323	132.452	0.588	0.022	0.664	0.023
HD 010516	55153.766	E1/W1	661.393	265.109	313.495	124.181	0.639	0.022	0.714	0.023
HD 010516	55153.774	E1/W1	653.107	284.940	313.500	115.751	0.660	0.026	0.724	0.028
HD 010516	55153.782	E1/W1	643.799	304.566	313.344	107.126	0.644	0.024	0.687	0.025
HD 022192	54754.914	S1/W1	396.051	-484.932	275.466	274.850	0.570	0.020	...	...
HD 022192	54754.941	S1/W1	440.224	-432.862	271.628	271.425	0.594	0.019	...	...
HD 022192	54754.973	S1/W1	475.710	-367.638	264.512	261.392	0.612	0.019	...	...
HD 022192	54754.980	S1/W1	483.126	-346.949	261.689	257.091	0.640	0.017	...	...
HD 022192	54754.988	S1/W1	487.960	-329.929	259.152	253.183	0.664	0.017	...	...
HD 022192	54754.996	S1/W1	491.828	-312.155	256.290	248.755	0.616	0.016	...	...
HD 022192	54755.004	S1/W1	494.654	-293.205	252.989	243.655	0.652	0.015	...	...
HD 022192	54755.012	S1/W1	496.121	-275.144	249.595	238.433	0.695	0.018	...	...
HD 022192	54755.019	S1/W1	496.414	-257.767	246.093	233.080	0.687	0.017	...	...
HD 022192	54755.027	S1/W1	495.522	-239.275	242.098	227.029	0.654	0.014	...	...
HD 022192	54761.008	S1/E1	31.538	-744.865	328.007	254.144	0.626	0.031	...	...
HD 022192	54761.016	S1/E1	60.588	-742.831	327.904	261.564	0.645	0.033	...	...
HD 022192	54761.028	S1/E1	90.950	-739.309	327.721	268.924	0.612	0.031	...	...
HD 022192	54761.035	S1/E1	115.975	-735.302	327.505	274.676	0.620	0.033	...	...
HD 022192	54761.043	S1/E1	136.228	-731.306	327.283	279.113	0.642	0.035	...	...
HD 022192	54761.051	S1/E1	165.376	-724.320	326.875	285.138	0.527	0.030	...	...
HD 022192	54761.059	S1/E1	192.011	-716.593	326.397	290.248	0.550	0.032	...	...
HD 022192	54767.844	E1/E2	133.292	60.179	64.343	25.844	0.951	0.035	...	...
HD 022192	54767.852	E1/E2	132.335	63.837	64.643	24.805	0.992	0.050	...	...
HD 022192	54767.856	E1/E2	131.287	67.204	64.889	23.841	0.958	0.051	...	...
HD 022192	54767.864	E1/E2	129.725	71.458	65.160	22.626	0.915	0.055	...	...
HD 022192	54767.891	E1/E2	120.558	88.550	65.811	18.207	0.933	0.058	...	...
HD 022192	54767.899	E1/E2	118.209	91.831	65.857	17.569	0.989	0.059	...	...
HD 022192	55131.930	E1/E2	105.236	106.142	65.760	16.662	0.994	0.031	...	...
HD 022192	55131.934	E1/E2	101.202	109.690	65.662	17.098	0.954	0.035	...	...
HD 022192	55131.950	E1/E2	93.269	115.809	65.421	18.612	0.990	0.037	...	...
HD 023630	54756.825	S1/W1	167.341	-549.381	252.672	252.672	0.964	0.069	...	...
HD 023630	54756.868	S1/W1	282.276	-525.282	262.360	262.360	0.921	0.058	...	...

Table 3—Continued

HD Number (1)	Date (HJD-2400000) (2)	Telescope Pair (3)	$u$ (cycles arcsec <sup>-1</sup> ) (4)	$v$ (cycles arcsec <sup>-1</sup> ) (5)	Baseline (m) (6)	Effective baseline (m) (7)	$V$ (8)	$\delta V$ (9)	$V_c$ (10)	$\delta V_c$ (11)
HD 023630	54757.778	S1/W1	35.734	-560.721	247.197	247.197	0.982	0.043	...	...
HD 023630	54757.798	S1/W1	95.433	-557.466	248.832	248.832	0.960	0.046	...	...
HD 023630	54757.825	S1/W1	176.327	-548.027	253.285	253.285	0.864	0.046	...	...
HD 023630	54792.767	E1/E2	135.180	61.139	65.274	65.274	0.898	0.033	...	...
HD 023630	54792.779	E1/E2	134.040	66.114	65.756	65.756	0.938	0.042	...	...
HD 023630	54792.795	E1/E2	131.545	71.475	65.867	65.867	0.880	0.064	...	...
HD 023630	54792.822	E1/E2	124.778	79.887	65.185	65.185	0.857	0.035	...	...
HD 023630	54792.838	E1/E2	118.104	85.475	64.142	64.142	0.814	0.034	...	...
HD 023630	54793.806	E1/E2	128.331	76.037	65.628	65.628	0.995	0.043	...	...
HD 023630	54793.818	E1/E2	124.264	80.381	65.113	65.113	0.867	0.047	...	...
HD 023630	54793.834	E1/E2	119.532	84.406	64.379	64.379	0.931	0.046	...	...
HD 023630	54793.846	E1/E2	114.828	87.738	63.580	63.580	0.918	0.052	...	...
HD 023630	54793.853	E1/E2	110.004	90.682	62.722	62.722	0.907	0.049	...	...
HD 023630	54793.873	E1/E2	98.911	96.211	60.708	60.708	0.833	0.053	...	...
HD 023630	54793.885	E1/E2	92.072	98.996	59.480	59.480	0.915	0.062	...	...
HD 023630	55153.806	E1/W1	690.865	158.091	311.812	311.812	0.896	0.061	...	...
HD 023630	55153.814	E1/W1	690.464	169.092	312.756	312.756	0.936	0.066	...	...
HD 023862	54757.860	S1/W1	271.038	-528.484	261.309	261.988	0.752	0.035	...	...
HD 023862	54757.876	S1/W1	310.060	-516.946	265.211	262.910	0.759	0.027	0.873	0.031
HD 023862	54757.888	S1/W1	341.209	-505.860	268.456	262.534	0.790	0.024	0.902	0.028
HD 023862	54757.919	S1/W1	400.768	-478.212	274.511	260.014	0.872	0.034	0.994	0.039
HD 023862	54757.942	S1/W1	436.869	-454.827	277.464	248.860	0.818	0.035	0.930	0.040
HD 023862	54757.985	S1/W1	484.700	-402.299	277.134	243.847	0.836	0.043	0.954	0.049
HD 023862	54792.830	E1/E2	122.541	81.960	64.861	31.198	0.944	0.044	1.079	0.050
HD 023862	54793.826	E1/E2	123.236	81.343	64.966	31.107	0.939	0.046	1.074	0.052
HD 023862	54793.849	E1/E2	113.734	88.465	63.394	32.322	0.974	0.056	1.104	0.064
HD 025940	54756.711	S1/W1	-218.655	-593.974	278.471	241.216	0.761	0.042	...	...
HD 025940	54756.726	S1/W1	-182.276	-605.864	278.360	241.079	0.751	0.044	...	...
HD 025940	54756.746	S1/W1	-120.276	-620.573	278.110	241.444	0.779	0.045	...	...
HD 025940	54756.754	S1/W1	-89.8550	-625.449	278.000	241.913	0.811	0.049	...	...
HD 025940	54756.765	S1/W1	-55.292	-629.230	277.905	242.681	0.845	0.050	...	...
HD 025940	54756.777	S1/W1	-23.801	-631.092	277.855	243.593	0.876	0.051	...	...
HD 025940	54756.789	S1/W1	8.924	-631.455	277.845	244.748	0.792	0.046	...	...



Table 3—Continued

HD Number (1)	Date (HJD−2400000) (2)	Telescope Pair (3)	$u$ (cycles arcsec <sup>−1</sup> ) (4)	$v$ (cycles arcsec <sup>−1</sup> ) (5)	Baseline (m) (6)	Effective baseline (m) (7)	$V$ (8)	$\delta V$ (9)	$V_c$ (10)	$\delta V_c$ (11)
HD 025940	54756.797	S1/W1	9.953	−630.324	277.876	246.029	0.748	0.040	...	...
HD 025940	54757.703	S1/W1	−231.784	−589.029	278.493	241.323	0.841	0.050	...	...
HD 025940	54757.715	S1/W1	−201.126	−600.025	278.425	241.119	0.783	0.048	...	...
HD 025940	54757.734	S1/W1	−142.573	−616.044	278.200	241.223	0.715	0.042	...	...
HD 025940	54757.703	S1/W1	−231.784	−589.029	278.493	241.323	0.843	0.049	...	...
HD 025940	54757.715	S1/W1	−201.126	−600.025	278.425	241.119	0.800	0.049	...	...
HD 025940	54757.734	S1/W1	−142.573	−616.044	278.200	241.223	0.730	0.042	...	...
HD 025940	54757.746	S1/W1	−108.068	−622.708	278.064	241.609	0.648	0.034	...	...
HD 025940	54760.969	S1/E1	−157.314	−727.311	327.390	284.001	0.785	0.044	...	...
HD 025940	54760.977	S1/E1	−130.427	−733.384	327.725	284.706	0.792	0.043	...	...
HD 025940	54760.984	S1/E1	−101.866	−738.510	327.993	285.508	0.807	0.043	...	...
HD 025940	54794.775	E1/E2	135.242	46.831	62.968	60.035	0.944	0.044	...	...
HD 025940	54794.779	E1/E2	134.880	51.319	63.493	60.291	0.911	0.048	...	...
HD 025940	54794.786	E1/E2	134.312	55.403	63.922	60.470	0.949	0.055	...	...
HD 025940	54794.794	E1/E2	133.376	60.087	64.361	60.614	0.892	0.052	...	...
HD 025940	54794.802	E1/E2	132.198	64.546	64.725	60.691	0.907	0.055	...	...
HD 025940	54794.806	E1/E2	130.896	68.544	65.008	60.711	0.913	0.054	...	...
HD 025940	54794.814	E1/E2	129.250	72.798	65.264	60.684	0.892	0.054	...	...
HD 025940	54794.821	E1/E2	127.503	76.677	65.459	60.616	0.863	0.054	...	...
HD 025940	54794.829	E1/E2	125.009	81.470	65.648	60.474	0.947	0.062	...	...
HD 025940	55152.954	E1/W1	474.998	488.627	299.815	267.938	0.808	0.025	...	...
HD 025940	55153.954	E1/W1	468.329	493.237	299.244	267.042	0.746	0.017	...	...
HD 037202	54756.956	S1/W1	315.314	−504.611	261.789	242.145	0.400	0.024	...	...
HD 037202	54756.964	S1/W1	340.858	−496.489	264.961	249.143	0.354	0.024	...	...
HD 037202	54756.995	S1/W1	400.023	−472.348	272.327	264.031	0.402	0.023	...	...
HD 037202	54757.007	S1/W1	420.278	−461.613	274.658	268.510	0.371	0.021	...	...
HD 037202	54757.015	S1/W1	434.880	−452.671	276.174	271.435	0.358	0.022	...	...
HD 037202	54757.022	S1/W1	446.674	−444.449	277.230	273.545	0.380	0.021	...	...
HD 037202	54757.030	S1/W1	457.800	−435.568	278.014	275.251	0.390	0.022	...	...
HD 037202	54757.042	S1/W1	467.205	−426.849	278.424	276.385	0.354	0.019	...	...
HD 037202	54758.011	S1/W1	433.810	−453.368	276.069	271.232	0.461	0.040	...	...
HD 037202	54758.019	S1/W1	446.273	−444.747	277.198	273.478	0.477	0.045	...	...
HD 037202	54758.026	S1/W1	455.748	−437.307	277.889	274.962	0.435	0.040	...	...

Table 3—Continued

HD Number (1)	Date (HJD−2400000) (2)	Telescope Pair (3)	$u$ (cycles arcsec <sup>−1</sup> ) (4)	$v$ (cycles arcsec <sup>−1</sup> ) (5)	Baseline (m) (6)	Effective baseline (m) (7)	$V$ (8)	$\delta V$ (9)	$V_c$ (10)	$\delta V_c$ (11)
HD 037202	54758.038	S1/W1	466.863	−427.191	278.415	276.351	0.465	0.045	...	...
HD 037202	54758.042	S1/W1	473.745	−419.831	278.498	276.932	0.483	0.043	...	...
HD 037202	54758.054	S1/W1	481.449	−409.981	278.215	277.172	0.430	0.039	...	...
HD 037202	54758.062	S1/W1	486.635	−401.723	277.629	276.920	0.407	0.040	...	...
HD 037202	54758.065	S1/W1	490.242	−394.520	276.857	276.373	0.430	0.040	...	...
HD 037202	54759.831	S1/E1	−492.805	−525.895	317.086	63.133	0.879	0.053	...	...
HD 037202	54759.839	S1/E1	−492.697	−534.146	319.712	62.032	0.775	0.047	...	...
HD 037202	54759.847	S1/E1	−491.534	−542.350	322.031	60.727	0.735	0.047	...	...
HD 037202	54759.847	S1/E1	−490.830	−545.410	322.822	60.193	0.864	0.050	...	...
HD 037202	54759.855	S1/E1	−488.463	−552.947	324.604	58.782	0.857	0.041	...	...
HD 037202	54759.862	S1/E1	−485.327	−560.197	326.096	57.325	0.822	0.030	...	...
HD 037202	54759.890	S1/E1	−459.301	−593.680	330.240	50.643	0.910	0.034	...	...
HD 037202	54760.866	S1/E1	−481.087	−567.847	327.439	55.721	0.759	0.052	...	...
HD 037202	54760.870	S1/E1	−477.619	−573.084	328.221	54.610	0.846	0.061	...	...
HD 037202	54760.878	S1/E1	−469.439	−583.359	329.438	52.497	0.869	0.063	...	...
HD 037202	54794.060	E1/E2	18.406	108.120	48.253	21.920	0.928	0.058	...	...
HD 037202	54794.068	E1/E2	12.478	108.366	47.992	23.965	0.882	0.063	...	...
HD 037202	54794.853	E1/E2	133.543	67.679	65.868	31.835	0.915	0.028	...	...
HD 037202	54794.861	E1/E2	132.529	69.650	65.870	31.021	0.874	0.029	...	...
HD 037202	54794.869	E1/E2	131.329	71.550	65.799	30.160	0.956	0.031	...	...
HD 037202	54794.923	E1/E2	111.541	87.405	62.346	19.810	0.929	0.043	...	...
HD 037202	54794.931	E1/E2	108.236	89.064	61.669	18.368	0.891	0.043	...	...
HD 037202	54794.939	E1/E2	104.510	90.774	60.903	16.808	0.934	0.042	...	...
HD 058715	54793.003	E1/E2	111.322	74.499	58.933	46.343	0.932	0.057	...	...
HD 058715	54793.015	E1/E2	105.857	75.560	57.220	44.910	0.903	0.052	...	...
HD 058715	54793.046	E1/E2	82.961	76.871	49.760	38.982	0.993	0.044	...	...
HD 058715	54793.054	E1/E2	77.393	77.381	48.150	37.775	0.882	0.044	...	...
HD 058715	54794.007	E1/E2	107.874	75.186	57.851	45.434	0.928	0.048	...	...
HD 058715	54794.011	E1/E2	106.582	75.428	57.447	45.098	0.936	0.049	...	...
HD 058715	54794.039	E1/E2	90.678	77.888	52.592	41.179	0.989	0.063	...	...
HD 058715	54795.031	E1/E2	93.593	77.497	53.461	41.863	0.968	0.062	...	...
HD 058715	54795.043	E1/E2	87.086	78.339	51.536	40.361	0.944	0.060	...	...
HD 058715	54795.050	E1/E2	82.285	78.894	50.154	39.312	0.904	0.053	...	...

Table 3—Continued

HD Number (1)	Date (HJD−2400000) (2)	Telescope Pair (3)	$u$ (cycles arcsec <sup>−1</sup> ) (4)	$v$ (cycles arcsec <sup>−1</sup> ) (5)	Baseline (m) (6)	Effective baseline (m) (7)	$V$ (8)	$\delta V$ (9)	$V_c$ (10)	$\delta V_c$ (11)
HD 058715	54795.058	E1/E2	75.292	79.617	48.211	37.883	0.883	0.050	...	...
HD 058715	54795.066	E1/E2	69.955	80.106	46.791	36.881	0.901	0.047	...	...
HD 058715	55152.980	E1/W1	686.529	183.952	312.702	258.769	0.607	0.039	...	...
HD 058715	55152.983	E1/W1	682.963	187.829	311.635	257.515	0.635	0.042	...	...
HD 058715	55152.991	E1/W1	676.859	192.760	309.634	255.360	0.715	0.026	...	...
HD 058715	55152.999	E1/W1	670.171	197.000	307.326	252.998	0.735	0.026	...	...
HD 058715	55153.976	E1/W1	687.046	183.269	312.844	258.950	0.587	0.026	...	...
HD 058715	55153.984	E1/W1	683.049	187.747	311.662	257.545	0.668	0.026	...	...
HD 058715	55153.987	E1/W1	677.491	192.309	309.847	255.583	0.678	0.028	...	...
HD 058715	55153.995	E1/W1	671.522	196.209	307.798	253.474	0.718	0.030	...	...
HD 058715	55154.003	E1/W1	663.061	200.777	304.803	250.490	0.717	0.027	...	...
HD 109387	55009.693	S1/E2	96.843	−523.464	234.213	234.213	0.925	0.058	...	...
HD 109387	55009.709	S1/E2	135.285	−512.037	233.008	233.008	0.946	0.053	...	...
HD 109387	55009.717	S1/E2	152.810	−505.398	232.298	232.298	0.875	0.051	...	...
HD 109387	55009.740	S1/E2	202.086	−481.294	229.660	229.660	0.798	0.050	...	...
HD 109387	55044.685	S1/E1	288.533	−571.023	281.480	281.480	0.744	0.046	...	...
HD 109387	55340.800	S2/W1	454.859	−39.202	200.854	200.854	0.872	0.055	...	...
HD 109387	55340.831	S2/W1	432.543	37.965	191.026	191.026	0.915	0.060	...	...
HD 109387	55340.843	S2/W1	417.555	71.308	186.360	186.360	0.907	0.045	...	...
HD 138749	54976.937	E1/E2	44.376	121.248	56.805	52.440	0.937	0.036	1.052	0.041
HD 138749	54976.957	E1/E2	30.815	123.292	55.913	53.560	0.932	0.043	1.061	0.049
HD 138749	55340.890	S2/W1	460.737	−296.485	241.040	146.197	0.945	0.048	1.038	0.052
HD 138749	55368.678	S1/E1	−399.306	−634.859	329.970	272.403	0.864	0.044	0.904	0.046
HD 138749	55368.694	S1/E1	−373.597	−651.798	330.534	280.073	0.825	0.041	0.937	0.046
HD 138749	55368.706	S1/E1	−344.618	−667.870	330.650	287.443	0.899	0.052	0.956	0.056
HD 138749	55381.760	S1/E1	−102.050	−735.429	326.662	321.006	0.864	0.056	0.938	0.060
HD 138749	55381.787	S1/E1	−18.564	−740.805	326.029	325.092	0.932	0.056	1.000	0.060
HD 138749	55382.740	S1/E1	−147.357	−729.256	327.330	317.432	0.866	0.045	0.915	0.047
HD 138749	55382.763	S1/E1	−86.244	−737.030	326.478	322.023	0.828	0.040	0.830	0.041
HD 142926	54666.774	S1/E1	30.879	−750.619	330.524	107.198	0.897	0.096	...	...
HD 142926	54666.782	S1/E1	53.255	−749.322	330.506	112.612	0.857	0.106	...	...
HD 142926	54666.833	S1/E1	209.170	−719.762	329.770	159.389	0.837	0.140	...	...
HD 142926	55009.865	S1/E2	160.860	−607.210	276.365	128.805	0.933	0.053	...	...

Table 3—Continued

HD Number (1)	Date (HJD−2400000) (2)	Telescope Pair (3)	$u$ (cycles arcsec <sup>−1</sup> ) (4)	$v$ (cycles arcsec <sup>−1</sup> ) (5)	Baseline (m) (6)	Effective baseline (m) (7)	$V$ (8)	$\delta V$ (9)	$V_c$ (10)	$\delta V_c$ (11)
HD 142926	55009.884	S1/E2	200.328	−592.994	275.381	141.721	0.963	0.056	...	...
HD 142926	55009.888	S1/E2	214.384	−586.912	274.907	146.379	0.896	0.051	...	...
HD 142926	55009.896	S1/E2	227.778	−580.553	274.378	150.831	0.899	0.050	...	...
HD 142926	55009.920	S1/E2	267.352	−557.979	272.215	163.967	0.860	0.071	...	...
HD 142926	55367.771	S1/E1	−226.953	−713.827	329.549	102.526	0.913	0.051	...	...
HD 142926	55367.783	S1/E1	−195.798	−723.839	329.908	96.554	0.958	0.056	...	...
HD 142926	55367.791	S1/E1	−166.932	−731.570	330.137	92.492	0.964	0.059	...	...
HD 142926	55367.799	S1/E1	−141.225	−737.295	330.280	90.200	0.855	0.048	...	...
HD 142926	55367.818	S1/E1	−89.774	−745.697	330.448	89.627	0.979	0.054	...	...
HD 142926	55367.826	S1/E1	−62.982	−748.541	330.494	91.432	0.967	0.060	...	...
HD 142926	55367.846	S1/E1	−7.623	−751.234	330.533	99.191	0.979	0.069	...	...
HD 142926	55368.838	S1/E1	−22.053	−750.940	330.529	96.697	0.943	0.032	...	...
HD 142926	55368.846	S1/E1	12.878	−751.160	330.532	103.228	0.944	0.031	...	...
HD 142926	55368.857	S1/E1	46.772	−749.770	330.512	110.993	0.898	0.030	...	...
HD 142926	55368.865	S1/E1	69.455	−747.947	330.485	116.817	0.889	0.029	...	...
HD 142926	55368.873	S1/E1	92.188	−745.391	330.443	123.064	0.921	0.030	...	...
HD 142926	55381.829	S1/E1	65.757	−748.294	330.490	115.838	0.902	0.132	...	...
HD 142926	55382.779	S1/E1	−74.464	−747.447	330.477	90.489	0.948	0.045	...	...
HD 142926	55382.790	S1/E1	−42.888	−750.010	330.516	93.662	0.982	0.046	...	...
HD 142926	55382.802	S1/E1	−15.243	−751.115	330.531	97.836	0.924	0.049	...	...
HD 142926	55382.806	S1/E1	7.932	−751.231	330.532	102.205	0.962	0.049	...	...
HD 142926	55382.814	S1/E1	30.267	−750.645	330.525	107.057	0.884	0.045	...	...
HD 142983	55011.700	S1/W2	112.136	−295.380	139.006	70.132	0.988	0.074	...	...
HD 142983	55011.708	S1/W2	123.875	−296.626	141.428	69.030	0.938	0.069	...	...
HD 142983	55011.716	S1/W2	135.067	−297.955	143.929	68.210	0.930	0.072	...	...
HD 142983	55013.692	S1/W2	107.516	−294.930	138.111	70.632	0.950	0.051	...	...
HD 142983	55013.700	S1/W2	118.650	−296.054	140.324	69.490	0.967	0.050	...	...
HD 142983	55046.674	S1/W1	463.050	−336.457	251.826	116.205	0.875	0.029	...	...
HD 142983	55046.682	S1/W1	471.151	−342.022	256.149	118.248	0.916	0.035	...	...
HD 142983	55046.689	S1/W1	478.538	−348.018	260.328	120.081	0.888	0.042	...	...
HD 142983	55046.701	S1/W1	488.031	−358.161	266.333	122.365	0.882	0.046	...	...
HD 142983	55046.713	S1/W1	492.957	−366.121	270.157	123.481	0.850	0.043	...	...
HD 142983	55046.721	S1/W1	495.510	−373.100	272.895	124.000	0.850	0.044	...	...

Table 3—Continued

HD Number (1)	Date (HJD-2400000) (2)	Telescope Pair (3)	$u$ (cycles arcsec <sup>-1</sup> ) (4)	$v$ (cycles arcsec <sup>-1</sup> ) (5)	Baseline (m) (6)	Effective baseline (m) (7)	$V$ (8)	$\delta V$ (9)	$V_c$ (10)	$\delta V_c$ (11)
HD 142983	55046.729	S1/W1	496.428	-379.637	274.956	124.116	0.775	0.046	...	...
HD 148184	54627.787	S2/W2	126.666	-224.698	113.484	110.056	0.823	0.040	...	...
HD 148184	54627.799	S2/W2	139.956	-227.260	117.426	113.641	0.893	0.047	...	...
HD 148184	54627.807	S2/W2	152.452	-230.007	121.405	117.284	0.811	0.046	...	...
HD 148184	54628.787	S2/W2	128.750	-225.077	114.082	110.598	0.872	0.063	...	...
HD 148184	54628.799	S2/W2	145.465	-228.429	119.148	115.215	0.811	0.055	...	...
HD 148184	54628.810	S2/W2	160.231	-231.902	124.014	119.682	0.914	0.057	...	...
HD 148184	54628.822	S2/W2	174.203	-235.711	128.952	124.243	0.867	0.055	...	...
HD 148184	54628.834	S2/W2	187.099	-239.768	133.806	128.749	0.919	0.057	...	...
HD 148184	55013.786	S1/W2	221.156	-292.421	161.305	155.327	0.696	0.044	...	...
HD 148184	55013.806	S1/W2	241.808	-300.476	169.689	163.154	0.753	0.046	...	...
HD 164284	54627.825	S2/W2	89.106	-328.711	149.840	137.424	0.716	0.040	0.826	0.046
HD 164284	54627.833	S2/W2	102.037	-328.316	151.262	137.230	0.709	0.044	0.807	0.050
HD 164284	54627.845	S2/W2	114.585	-327.870	152.806	137.136	0.740	0.040	0.842	0.046
HD 164284	54627.853	S2/W2	126.037	-327.406	154.351	137.129	0.826	0.044	0.949	0.050
HD 164284	54627.861	S2/W2	137.571	-326.880	156.033	137.199	0.840	0.044	0.955	0.050
HD 164284	54627.868	S2/W2	149.041	-326.291	157.823	137.341	0.844	0.042	0.968	0.048
HD 164284	54627.876	S2/W2	159.587	-325.685	159.567	137.534	0.858	0.046	0.978	0.052
HD 164284	54627.888	S2/W2	171.767	-324.899	161.691	137.827	0.872	0.048	0.997	0.055
HD 164284	54627.896	S2/W2	181.990	-324.157	163.556	138.128	0.852	0.044	0.975	0.050
HD 164284	54627.907	S2/W2	194.160	-323.155	165.865	138.544	0.920	0.049	1.051	0.056
HD 164284	54627.915	S2/W2	203.831	-322.248	167.759	138.912	0.806	0.044	0.925	0.050
HD 164284	54627.923	S2/W2	212.586	-321.319	169.508	139.267	0.792	0.042	0.900	0.048
HD 164284	54627.935	S2/W2	220.166	-320.410	171.041	139.582	0.891	0.054	1.022	0.062
HD 166014	54973.941	E1/E2	117.932	88.141	64.776	63.092	0.865	0.026	0.943	0.029
HD 166014	54973.956	E1/E2	108.693	94.991	63.510	60.733	0.868	0.030	0.947	0.032
HD 166014	54973.968	E1/E2	104.262	97.711	62.867	59.522	0.899	0.025	0.980	0.027
HD 166014	54973.976	E1/E2	99.882	100.132	62.225	58.290	0.894	0.022	0.974	0.024
HD 166014	54973.987	E1/E2	92.572	103.694	61.156	56.174	0.892	0.029	0.973	0.031
HD 166014	54973.995	E1/E2	88.031	105.652	60.504	54.832	0.901	0.026	0.982	0.029
HD 166014	54974.003	E1/E2	82.702	107.736	59.755	53.238	0.911	0.030	0.993	0.033
HD 166014	55010.703	S1/E2	-352.074	-516.042	274.847	238.510	0.681	0.045	0.742	0.049
HD 166014	55010.711	S1/E2	-345.619	-522.711	275.699	237.513	0.699	0.044	0.762	0.048

Table 3—Continued

HD Number (1)	Date (HJD-2400000) (2)	Telescope Pair (3)	$u$ (cycles arcsec <sup>-1</sup> ) (4)	$v$ (cycles arcsec <sup>-1</sup> ) (5)	Baseline (m) (6)	Effective baseline (m) (7)	$V$ (8)	$\delta V$ (9)	$V_c$ (10)	$\delta V_c$ (11)
HD 166014	55010.718	S1/E2	-338.381	-529.463	276.454	236.262	0.780	0.051	0.850	0.056
HD 166014	55365.777	S1/W1	233.844	-555.002	264.970	115.293	0.887	0.027	0.967	0.029
HD 166014	55365.800	S1/W1	292.489	-537.299	269.148	120.120	0.796	0.031	0.867	0.034
HD 166014	55366.781	S1/W1	247.708	-551.302	265.911	115.971	0.793	0.041	0.864	0.044
HD 166014	55366.789	S1/W1	269.495	-544.901	267.454	117.620	0.836	0.049	0.911	0.053
HD 166014	55366.797	S1/W1	293.036	-537.107	269.189	120.189	0.941	0.061	1.026	0.066
HD 166014	55366.804	S1/W1	314.703	-529.032	270.823	123.257	0.940	0.056	1.025	0.061
HD 166014	55366.816	S1/W1	337.270	-519.570	272.530	127.139	0.902	0.058	0.983	0.064
HD 166014	55368.742	S1/E1	-462.476	-579.387	326.159	292.999	0.853	0.041	0.930	0.045
HD 166014	55368.754	S1/E1	-452.749	-591.114	327.587	291.717	0.764	0.032	0.832	0.035
HD 166014	55368.761	S1/E1	-441.205	-603.092	328.762	289.841	0.731	0.029	0.797	0.031
HD 166014	55368.773	S1/E1	-421.018	-620.687	329.975	285.966	0.772	0.033	0.841	0.036
HD 166014	55368.781	S1/E1	-408.099	-630.362	330.383	283.215	0.700	0.033	0.763	0.036
HD 166014	55368.793	S1/E1	-389.298	-642.828	330.641	278.950	0.832	0.046	0.907	0.050
HD 166014	55368.797	S1/E1	-377.650	-649.772	330.653	276.188	0.903	0.049	0.984	0.053
HD 166014	55368.804	S1/E1	-364.233	-657.154	330.564	272.917	0.758	0.038	0.827	0.042
HD 166014	55368.820	S1/E1	-334.985	-671.341	330.094	265.532	0.863	0.042	0.940	0.046
HD 166014	55381.695	S1/E1	-475.834	-559.216	323.048	293.996	0.771	0.049	0.841	0.053
HD 166014	55381.703	S1/E1	-468.553	-570.969	324.962	293.596	0.781	0.052	0.852	0.057
HD 166014	55381.711	S1/E1	-459.579	-583.074	326.638	292.653	0.771	0.056	0.840	0.061
HD 166014	55381.718	S1/E1	-450.679	-593.395	327.833	291.405	0.752	0.051	0.819	0.056
HD 166014	55381.726	S1/E1	-441.645	-602.666	328.725	289.918	0.725	0.048	0.790	0.053
HD 166014	55382.687	S1/E1	-479.906	-551.443	321.625	293.991	0.704	0.044	0.768	0.048
HD 166014	55382.691	S1/E1	-475.065	-560.569	323.283	293.975	0.793	0.048	0.864	0.052
HD 166014	55382.699	S1/E1	-469.400	-569.709	324.771	293.663	0.879	0.050	0.958	0.055
HD 166014	55382.707	S1/E1	-462.058	-579.931	326.231	292.951	0.808	0.051	0.880	0.056
HD 166014	55382.711	S1/E1	-454.688	-588.915	327.340	291.998	0.824	0.049	0.898	0.054
HD 166014	55383.711	S1/W1	184.316	-566.091	261.928	115.219	0.818	0.042	0.892	0.045
HD 166014	55383.718	S1/W1	204.183	-562.025	263.083	114.813	0.887	0.046	0.967	0.050
HD 166014	55405.655	W1/S1	-202.470	562.417	262.976	114.824	0.846	0.050	0.922	0.054
HD 166014	55405.667	W1/S1	-233.675	555.070	264.956	115.286	0.966	0.051	1.053	0.055
HD 166014	55405.694	W1/S1	-304.280	533.059	270.032	121.696	0.850	0.046	0.927	0.050
HD 166014	55405.702	W1/S1	-324.862	524.943	271.591	124.917	0.954	0.049	1.040	0.053

Table 3—Continued

HD Number (1)	Date (HJD-2400000) (2)	Telescope Pair (3)	$u$ (cycles arcsec <sup>-1</sup> ) (4)	$v$ (cycles arcsec <sup>-1</sup> ) (5)	Baseline (m) (6)	Effective baseline (m) (7)	$V$ (8)	$\delta V$ (9)	$V_c$ (10)	$\delta V_c$ (11)
HD 166014	55405.710	W1/S1	-343.167	516.929	272.970	128.262	0.876	0.047	0.955	0.051
HD 166014	55405.718	W1/S1	-361.824	507.871	274.339	132.118	0.826	0.046	0.900	0.050
HD 166014	55405.655	W1/S1	-202.470	562.417	262.976	114.824	0.846	0.050	0.922	0.054
HD 166014	55405.667	W1/S1	-233.675	555.070	264.956	115.286	0.966	0.051	1.053	0.055
HD 166014	55405.694	W1/S1	-304.280	533.059	270.032	121.696	0.850	0.046	0.927	0.050
HD 166014	55405.702	W1/S1	-324.862	524.943	271.591	124.917	0.954	0.049	1.040	0.053
HD 166014	55405.710	W1/S1	-343.167	516.929	272.970	128.262	0.876	0.047	0.955	0.051
HD 166014	55405.718	W1/S1	-361.824	507.871	274.339	132.118	0.826	0.046	0.900	0.050
HD 198183	55010.885	S1/E2	-248.823	-579.262	277.372	276.761	0.635	0.072	1.083	0.124
HD 198183	55010.897	S1/E2	-223.674	-590.906	277.979	276.831	0.668	0.073	1.091	0.121
HD 198183	55365.845	S1/W1	110.766	-603.531	269.966	251.306	0.664	0.027	1.029	0.041
HD 198183	55365.857	S1/W1	151.449	-596.899	270.935	249.108	0.704	0.026	1.069	0.040
HD 198183	55365.865	S1/W1	172.252	-592.632	271.526	248.034	0.632	0.026	1.047	0.042
HD 198183	55365.873	S1/W1	191.251	-588.185	272.116	247.082	0.514	0.020	0.832	0.031
HD 198183	55365.877	S1/W1	212.566	-582.540	272.826	246.042	0.572	0.022	0.983	0.034
HD 198183	55365.912	S1/W1	297.314	-552.170	275.912	242.113	0.732	0.025	1.030	0.043
HD 198183	55367.967	S1/E1	-237.700	-712.916	330.632	328.516	0.521	0.025	0.835	0.040
HD 198183	55367.978	S1/E1	-207.543	-722.002	330.518	327.446	0.641	0.025	1.048	0.041
HD 198183	55367.990	S1/E1	-176.748	-729.759	330.350	326.147	0.597	0.025	0.982	0.042
HD 198183	55368.002	S1/E1	-147.037	-735.907	330.172	324.735	0.610	0.028	1.045	0.047
HD 198183	55381.956	S1/E1	-162.820	-732.799	330.267	325.503	0.587	0.046	0.991	0.078
HD 198183	55381.983	S1/E1	-87.6450	-744.582	329.851	321.557	0.543	0.040	0.881	0.066
HD 198183	55381.995	S1/E1	-49.5940	-747.766	329.712	319.335	0.598	0.042	1.023	0.070
HD 198183	55382.842	S1/E1	-429.136	-600.319	324.662	324.178	0.590	0.034	1.004	0.059
HD 198183	55382.846	S1/E1	-418.669	-610.820	325.806	325.498	0.526	0.034	1.000	0.100
HD 198183	55382.854	S1/E1	-406.037	-622.303	326.916	326.762	0.611	0.035	1.000	0.100
HD 198183	55382.862	S1/E1	-393.004	-633.039	327.821	327.768	0.631	0.033	0.998	0.051
HD 198183	55382.874	S1/E1	-365.927	-652.508	329.141	329.133	0.600	0.032	1.000	0.100
HD 198183	55383.753	S1/W1	-23.4060	-610.649	268.860	259.400	0.599	0.021	0.987	0.033
HD 198183	55383.760	S1/W1	6.489	-610.952	268.812	257.503	0.542	0.019	0.816	0.028
HD 198183	55383.772	S1/W1	37.555	-610.131	268.943	255.581	0.674	0.020	1.024	0.031
HD 198183	55383.780	S1/W1	64.623	-608.465	269.208	253.956	0.621	0.023	0.886	0.035
HD 200120	55009.970	S1/E2	-88.246	-616.197	273.870	86.097	0.933	0.042	1.015	0.045

Table 3—Continued

HD Number (1)	Date (HJD−2400000) (2)	Telescope Pair (3)	$u$ (cycles arcsec <sup>−1</sup> ) (4)	$v$ (cycles arcsec <sup>−1</sup> ) (5)	Baseline (m) (6)	Effective baseline (m) (7)	$V$ (8)	$\delta V$ (9)	$V_c$ (10)	$\delta V_c$ (11)
HD 200120	55009.982	S1/E2	−57.199	−620.607	274.201	85.011	0.864	0.044	0.941	0.048
HD 200120	55009.993	S1/E2	−29.247	−622.938	274.372	85.704	0.880	0.050	0.959	0.054
HD 200120	55043.741	S1/E1	−471.532	−489.003	298.873	201.254	0.766	0.040	0.832	0.043
HD 200120	55043.748	S1/E1	−464.247	−505.268	301.887	198.479	0.771	0.045	0.837	0.049
HD 200120	55043.756	S1/E1	−455.980	−521.176	304.670	195.354	0.773	0.047	0.842	0.051
HD 200120	55043.764	S1/E1	−447.224	−535.966	307.115	192.074	0.805	0.048	0.871	0.052
HD 200120	55043.772	S1/E1	−437.289	−550.880	309.445	188.387	0.682	0.043	0.740	0.046
HD 200120	55043.780	S1/E1	−426.982	−564.750	311.492	184.603	0.751	0.041	0.816	0.045
HD 200120	55069.831	E1/E2	100.630	110.012	65.596	43.030	0.989	0.043	1.076	0.047
HD 200120	55069.843	E1/E2	94.069	115.029	65.377	40.448	0.993	0.051	1.081	0.055
HD 200120	55069.851	E1/E2	88.505	118.781	65.171	38.310	0.997	0.056	1.085	0.061
HD 200120	55069.858	E1/E2	82.816	122.213	64.952	36.175	0.953	0.053	1.038	0.057
HD 200120	55366.923	S1/W1	317.374	−546.760	278.143	174.911	0.968	0.038	1.050	0.042
HD 200120	55366.934	S1/W1	342.486	−530.269	277.729	183.497	0.938	0.036	1.020	0.039
HD 200120	55382.892	S1/E1	−347.147	−641.213	320.801	156.839	0.745	0.038	0.810	0.041
HD 200120	55382.900	S1/E1	−324.485	−656.784	322.303	149.544	0.731	0.035	0.795	0.038
HD 200120	55382.912	S1/E1	−302.793	−669.990	323.476	142.857	0.714	0.035	0.775	0.038
HD 200120	55382.919	S1/E1	−277.582	−683.543	324.585	135.499	0.764	0.037	0.831	0.040
HD 200120	55382.931	S1/E1	−245.074	−698.552	325.702	126.769	0.842	0.041	0.917	0.045
HD 202904	54688.926	S1/E1	−18.049	−747.138	328.809	127.427	0.872	0.045	...	...
HD 202904	54688.933	S1/E1	8.602	−747.284	328.799	135.631	0.766	0.039	...	...
HD 202904	54688.945	S1/E1	43.737	−746.215	328.870	146.820	0.768	0.042	...	...
HD 202904	54688.957	S1/E1	78.904	−743.691	329.033	158.310	0.759	0.046	...	...
HD 202904	54688.969	S1/E1	109.304	−740.306	329.238	168.389	0.807	0.049	...	...
HD 202904	54688.976	S1/E1	138.676	−735.936	329.483	178.197	0.644	0.040	...	...
HD 202904	54688.988	S1/E1	176.052	−728.726	329.836	190.705	0.607	0.038	...	...
HD 202904	54689.000	S1/E1	203.983	−722.046	330.107	200.028	0.674	0.042	...	...
HD 202904	54689.012	S1/E1	236.219	−712.834	330.392	210.711	0.726	0.048	...	...
HD 202904	55044.761	S1/E1	−462.100	−563.445	320.602	136.641	0.779	0.040	...	...
HD 202904	55044.769	S1/E1	−453.250	−576.138	322.517	132.771	0.818	0.049	...	...
HD 202904	55382.959	S1/E1	−212.399	−719.802	330.186	86.195	0.909	0.038	...	...
HD 202904	55382.967	S1/E1	−187.013	−726.241	329.943	88.507	0.821	0.034	...	...
HD 202904	55382.979	S1/E1	−154.719	−733.074	329.631	93.215	0.917	0.044	...	...



Table 3—Continued

HD Number (1)	Date (HJD−2400000) (2)	Telescope Pair (3)	$u$ (cycles arcsec <sup>−1</sup> ) (4)	$v$ (cycles arcsec <sup>−1</sup> ) (5)	Baseline (m) (6)	Effective baseline (m) (7)	$V$ (8)	$\delta V$ (9)	$V_c$ (10)	$\delta V_c$ (11)
HD 202904	55382.987	S1/E1	−128.678	−737.548	329.396	98.226	0.861	0.039	...	...
HD 203467	55044.891	S1/E1	−185.852	−654.232	299.227	255.314	0.879	0.048	...	...
HD 203467	55044.903	S1/E1	−155.004	−664.531	300.217	253.607	0.839	0.048	...	...
HD 203467	55044.919	S1/E1	−109.489	−676.022	301.301	251.097	0.885	0.055	...	...
HD 203467	55044.926	S1/E1	−85.855	−680.349	301.703	249.823	0.827	0.050	...	...
HD 203467	55044.934	S1/E1	−63.105	−683.499	301.993	248.628	0.832	0.042	...	...
HD 203467	55044.942	S1/E1	−41.188	−685.611	302.187	247.512	0.855	0.043	...	...
HD 203467	55044.954	S1/E1	4.236	−687.155	302.329	245.339	0.857	0.045	...	...
HD 203467	55043.887	S1/E1	−210.332	−644.501	298.275	256.648	0.887	0.068	...	...
HD 203467	55043.895	S1/E1	−189.240	−652.971	299.105	255.501	0.832	0.067	...	...
HD 203467	55043.903	S1/E1	−165.099	−661.393	299.918	254.167	0.711	0.052	...	...
HD 203467	55043.911	S1/E1	−143.541	−667.829	300.531	252.971	0.784	0.057	...	...
HD 203467	55043.919	S1/E1	−120.150	−673.710	301.084	251.680	0.829	0.058	...	...
HD 203467	55043.926	S1/E1	−95.132	−678.781	301.557	250.319	0.736	0.053	...	...
HD 203467	55043.934	S1/E1	−74.639	−682.025	301.858	249.229	0.746	0.050	...	...
HD 203467	55043.938	S1/E1	−52.206	−684.661	302.100	248.068	0.831	0.055	...	...
HD 203467	55043.946	S1/E1	−29.587	−686.367	302.257	246.938	0.693	0.045	...	...
HD 203467	55043.973	S1/E1	47.696	−685.077	302.138	243.468	0.731	0.042	...	...
HD 203467	55043.981	S1/E1	74.719	−682.014	301.857	242.422	0.767	0.047	...	...
HD 203467	55043.989	S1/E1	97.478	−678.358	301.518	241.614	0.905	0.054	...	...
HD 203467	55043.997	S1/E1	120.190	−673.701	301.084	240.878	0.864	0.060	...	...
HD 203467	55340.920	S2/W1	93.560	−548.997	245.010	196.078	0.855	0.042	...	...
HD 203467	55340.932	S2/W1	132.342	−540.130	244.655	195.480	0.895	0.044	...	...
HD 203467	55340.952	S2/W1	180.064	−524.571	243.999	195.365	0.934	0.046	...	...
HD 203467	55340.963	S2/W1	215.169	−509.503	243.321	195.725	0.903	0.045	...	...
HD 203467	55340.975	S2/W1	243.015	−495.085	242.633	196.279	0.889	0.049	...	...
HD 209409	54687.767	S1/E1	−428.715	−604.476	326.044	126.315	0.811	0.048	...	...
HD 209409	54688.779	S1/E1	−451.948	−559.568	316.460	136.914	0.759	0.043	...	...
HD 209409	54688.795	S1/E1	−433.490	−558.143	310.926	130.173	0.763	0.041	...	...
HD 209409	54688.806	S1/E1	−413.988	−556.905	305.301	123.146	0.734	0.036	...	...
HD 209409	54688.818	S1/E1	−392.844	−555.770	299.436	115.670	0.816	0.041	...	...
HD 209409	54688.838	S1/E1	−352.592	−554.012	288.922	101.995	0.826	0.049	...	...
HD 209409	55011.921	S1/W2	55.456	−363.928	161.963	80.066	0.936	0.062	...	...

Table 3—Continued

HD Number (1)	Date (HJD-2400000) (2)	Telescope Pair (3)	$u$ (cycles arcsec <sup>-1</sup> ) (4)	$v$ (cycles arcsec <sup>-1</sup> ) (5)	Baseline (m) (6)	Effective baseline (m) (7)	$V$ (8)	$\delta V$ (9)	$V_c$ (10)	$\delta V_c$ (11)
HD 209409	55011.929	S1/W2	68.713	-364.034	162.990	84.897	0.943	0.067	...	...
HD 209409	55011.937	S1/W2	81.916	-364.163	164.222	89.801	0.855	0.057	...	...
HD 209409	55011.949	S1/W2	107.182	-364.481	167.148	99.393	0.854	0.057	...	...
HD 209409	55011.956	S1/W2	119.283	-364.667	168.805	104.067	0.958	0.057	...	...
HD 209409	55011.964	S1/W2	130.852	-364.868	170.540	108.576	0.794	0.050	...	...
HD 209409	55012.914	S1/W2	49.312	-363.887	161.560	77.863	0.840	0.040	...	...
HD 209409	55013.890	S1/W2	7.902	-363.736	160.068	63.799	0.870	0.044	...	...
HD 209409	55013.925	S1/W2	70.078	-364.046	163.107	85.400	0.804	0.036	...	...
HD 209409	55013.929	S1/W2	80.944	-364.153	164.124	89.437	0.925	0.034	...	...
HD 209409	55013.937	S1/W2	92.515	-364.285	165.360	93.794	0.954	0.043	...	...
HD 209409	55413.904	S1/E2	-107.555	-489.067	220.303	58.038	0.869	0.030	...	...
HD 209409	55413.916	S1/E2	-84.546	-488.843	218.256	61.262	0.869	0.030	...	...
HD 209409	55413.923	S1/E2	-65.526	-488.701	216.925	64.905	0.963	0.033	...	...
HD 209409	55413.931	S1/E2	-41.632	-488.575	215.724	70.513	0.963	0.036	...	...
HD 209409	55413.955	S1/E2	9.457	-488.494	214.950	85.310	0.936	0.043	...	...
HD 209409	55414.838	S1/E2	-242.611	-491.727	241.230	69.816	0.945	0.031	...	...
HD 209409	55414.853	S1/E2	-217.468	-491.022	236.260	64.101	0.955	0.029	...	...
HD 209409	55414.861	S1/E2	-199.716	-490.591	233.031	60.842	0.950	0.028	...	...
HD 209409	55414.869	S1/E2	-178.886	-490.148	229.549	58.007	0.940	0.028	...	...
HD 209409	55414.880	S1/E2	-157.221	-489.753	226.293	56.358	0.931	0.026	...	...
HD 212076	55045.880	S1/W1	359.202	-456.312	255.499	255.368	0.967	0.043	...	...
HD 212076	55045.891	S1/W1	382.341	-450.810	260.068	259.829	0.935	0.039	...	...
HD 212076	55367.880	S1/E1	-490.121	-565.572	329.265	315.754	0.780	0.048	...	...
HD 212076	55367.892	S1/E1	-484.724	-573.431	330.348	316.900	0.873	0.050	...	...
HD 212076	55367.904	S1/E1	-477.105	-580.702	330.659	317.324	0.845	0.047	...	...
HD 212076	55367.916	S1/E1	-466.939	-587.908	330.315	317.148	0.921	0.048	...	...
HD 212076	55367.927	S1/E1	-454.366	-594.928	329.352	316.409	0.902	0.052	...	...
HD 212076	55367.939	S1/E1	-436.168	-603.074	327.452	314.849	0.991	0.056	...	...
HD 212076	55368.900	S1/E1	-479.483	-578.680	330.639	317.267	0.874	0.046	...	...
HD 212076	55368.920	S1/E1	-461.805	-590.962	329.972	316.896	0.900	0.048	...	...
HD 212076	55368.931	S1/E1	-443.510	-600.003	328.268	315.526	0.911	0.049	...	...
HD 217675	55044.819	S1/E1	-475.953	-505.723	305.541	290.158	0.743	0.043	0.950	0.055
HD 217675	55044.826	S1/E1	-468.254	-523.082	308.877	295.647	0.721	0.039	0.925	0.050

Table 3—Continued

HD Number (1)	Date (HJD-2400000) (2)	Telescope Pair (3)	$u$ (cycles arcsec <sup>-1</sup> ) (4)	$v$ (cycles arcsec <sup>-1</sup> ) (5)	Baseline (m) (6)	Effective baseline (m) (7)	$V$ (8)	$\delta V$ (9)	$V_c$ (10)	$\delta V_c$ (11)
HD 217675	55043.811	S1/E1	-483.744	-483.104	300.788	282.589	0.852	0.043	1.000	0.100
HD 217675	55043.826	S1/E1	-472.681	-513.528	307.073	292.661	0.817	0.042	1.045	0.054
HD 217675	55043.850	S1/E1	-445.976	-560.784	315.234	306.536	0.854	0.046	1.094	0.059
HD 217675	55043.858	S1/E1	-434.472	-576.193	317.495	310.540	0.892	0.049	1.000	0.100
HD 217675	55043.865	S1/E1	-421.916	-591.043	319.495	314.126	0.866	0.056	1.112	0.071
HD 217675	55043.873	S1/E1	-408.693	-604.988	321.215	317.227	0.805	0.056	1.033	0.072
HD 217675	55045.811	S1/W1	96.826	-618.224	275.311	228.533	0.728	0.045	0.943	0.058
HD 217675	55045.815	S1/W1	112.630	-615.927	275.479	224.681	0.702	0.046	0.888	0.059
HD 217675	55045.826	S1/W1	151.470	-608.704	275.974	214.586	0.669	0.039	0.864	0.050
HD 217675	55045.850	S1/W1	212.086	-592.603	276.918	196.908	0.724	0.036	0.935	0.047
HD 217675	55045.858	S1/W1	238.145	-583.671	277.346	188.508	0.657	0.034	0.867	0.043
HD 217675	55046.803	S1/W1	84.6040	-619.753	275.198	231.414	0.761	0.034	0.973	0.044
HD 217675	55046.815	S1/W1	118.710	-614.946	275.549	223.161	0.780	0.038	0.984	0.049
HD 217675	55046.827	S1/W1	151.743	-608.645	275.978	214.512	0.882	0.040	1.000	0.100
HD 217675	55046.834	S1/W1	182.281	-601.295	276.436	205.909	0.825	0.039	1.052	0.050
HD 217675	55046.858	S1/W1	241.580	-582.395	277.402	187.361	0.804	0.039	1.058	0.050
HD 217675	55046.866	S1/W1	269.911	-570.920	277.840	177.526	0.644	0.033	0.839	0.042
HD 217675	55366.956	S1/W1	183.999	-600.828	276.460	205.404	0.716	0.029	0.920	0.038
HD 217675	55366.964	S1/W1	209.194	-593.508	276.867	197.806	0.749	0.031	0.956	0.040
HD 217675	55366.980	S1/W1	242.014	-582.223	277.405	187.212	0.770	0.032	0.979	0.041
HD 217675	55383.926	S1/W1	223.567	-588.828	277.107	193.271	0.825	0.039	1.069	0.050
HD 217675	55383.934	S1/W1	248.237	-579.852	277.509	185.111	0.824	0.037	1.059	0.047
HD 217675	55383.950	S1/W1	288.692	-562.311	278.096	170.607	0.904	0.050	1.000	0.100
HD 217675	55383.965	S1/W1	329.888	-540.167	278.468	154.134	0.907	0.052	1.000	0.100
HD 217675	55383.973	S1/W1	348.011	-528.757	278.499	146.223	0.811	0.050	1.043	0.064
HD 217675	55383.985	S1/W1	367.622	-515.015	278.391	137.107	0.700	0.044	0.892	0.056
HD 217675	55383.993	S1/W1	384.824	-501.550	278.132	128.551	0.786	0.048	1.008	0.062
HD 217891	54687.821	S1/E1	-456.640	-578.466	324.245	322.770	0.741	0.049	...	...
HD 217891	54689.911	S1/E1	-265.340	-593.779	286.138	285.201	0.816	0.055	...	...
HD 217891	54689.923	S1/E1	-237.812	-594.869	281.859	280.178	0.741	0.051	...	...
HD 217891	54689.935	S1/E1	-208.736	-595.854	277.774	275.059	0.734	0.043	...	...
HD 217891	54689.993	S1/E1	-27.3410	-598.893	263.765	248.600	0.902	0.058	...	...
HD 217891	54690.009	S1/E1	14.6570	-598.929	263.586	244.092	0.891	0.057	...	...

Table 3—Continued

HD Number (1)	Date (HJD−2400000) (2)	Telescope Pair (3)	$u$ (cycles arcsec <sup>−1</sup> ) (4)	$v$ (cycles arcsec <sup>−1</sup> ) (5)	Baseline (m) (6)	Effective baseline (m) (7)	$V$ (8)	$\delta V$ (9)	$V_c$ (10)	$\delta V_c$ (11)
HD 217891	54690.907	S1/W1	406.283	−410.876	254.223	184.300	0.882	0.038	...	...
HD 217891	54690.919	S1/W1	429.165	−408.495	260.676	187.690	0.948	0.039	...	...
HD 217891	54691.927	S1/W1	441.134	−407.041	264.081	189.529	0.822	0.079	...	...
HD 217891	54691.943	S1/W1	460.388	−404.244	269.554	192.545	0.883	0.087	...	...
HD 217891	55011.982	S1/W2	90.2910	−393.355	177.562	154.737	0.783	0.044	...	...
HD 217891	55011.986	S1/W2	102.915	−393.067	178.764	154.193	0.814	0.050	...	...
HD 217891	55012.955	S1/W2	44.4740	−394.064	174.474	157.605	0.932	0.038	...	...
HD 217891	55012.963	S1/W2	60.8400	−393.869	175.343	156.422	0.972	0.037	...	...
HD 217891	55012.979	S1/W2	88.4290	−393.394	177.398	154.826	0.952	0.036	...	...
HD 217891	55012.986	S1/W2	55012.986	−393.089	178.675	154.228	0.908	0.037	...	...
HD 217891	55012.994	S1/W2	115.925	−392.726	180.155	153.746	0.919	0.034	...	...
HD 217891	55013.959	S1/W2	61.197	−393.864	175.365	156.398	0.898	0.044	...	...
HD 217891	55013.971	S1/W2	83.840	−393.486	177.005	155.057	0.971	0.041	...	...
HD 217891	55013.979	S1/W2	95.628	−393.238	178.053	154.494	0.941	0.046	...	...
HD 217891	55013.986	S1/W2	106.524	−392.977	179.135	154.058	0.864	0.038	...	...
HD 217891	55013.994	S1/W2	119.643	−392.619	180.580	153.640	0.894	0.042	...	...
HD 217891	55013.998	S1/W2	132.252	−392.228	182.112	153.349	0.821	0.038	...	...
HD 217891	55045.942	S1/W1	416.604	−409.857	257.121	185.806	0.909	0.036	...	...
HD 217891	55045.950	S1/W1	433.474	−407.991	261.901	188.348	0.935	0.036	...	...
HD 217891	55045.958	S1/W1	446.526	−406.324	265.617	190.369	0.877	0.034	...	...
HD 217891	55045.969	S1/W1	457.573	−404.699	268.757	192.102	0.919	0.035	...	...
HD 217891	55045.981	S1/W1	472.818	−401.951	273.033	194.488	0.744	0.033	...	...
HD 217891	55045.993	S1/W1	480.466	−400.193	275.110	195.646	0.889	0.047	...	...
HD 217891	55046.012	S1/W1	492.688	−395.930	278.084	197.241	0.860	0.044	...	...
HD 217891	55046.020	S1/W1	495.282	−394.131	278.481	197.390	0.808	0.042	...	...
HD 217891	55414.997	S1/E2	22.898	−527.803	232.421	214.139	0.851	0.043	...	...
HD 217891	55415.005	S1/E2	44.433	−527.677	232.969	212.205	0.947	0.051	...	...
HD 217891	55415.013	S1/E2	62.762	−527.505	233.709	210.730	0.880	0.052	...	...
HD 217891	55152.608	E1/W1	690.717	173.262	313.305	270.167	0.819	0.033	...	...
HD 217891	55152.616	E1/W1	690.649	175.406	313.507	270.612	0.783	0.036	...	...
HD 217891	55152.623	E1/W1	689.367	177.274	313.164	270.591	0.722	0.045	...	...
HD 217891	55153.592	E1/W1	687.498	169.694	311.552	268.309	0.815	0.036	...	...
HD 217891	55153.600	E1/W1	689.590	171.435	312.629	269.391	0.791	0.047	...	...

Table 3—Continued

HD Number (1)	Date (HJD−2400000) (2)	Telescope Pair (3)	$u$ (cycles arcsec <sup>−1</sup> ) (4)	$v$ (cycles arcsec <sup>−1</sup> ) (5)	Baseline (m) (6)	Effective baseline (m) (7)	$V$ (8)	$\delta V$ (9)	$V_c$ (10)	$\delta V_c$ (11)
HD 217891	55153.592	E1/W1	687.498	169.694	311.552	268.309	0.815	0.036	...	...
HD 217891	55153.600	E1/W1	689.590	171.435	312.629	269.391	0.791	0.047	...	...

Table 4. Binary Star Properties

HD Number	Number of Components	Speckle Obs. Ref.	Binary Designation	$P$ (y)	$a$ (mas)	$\Delta K$ (mag)	Corr.	Ref.
HD 004180	3	1	A,B	2.824	17	2.6	Y	2
			Ba,Bb	0.01:	0.4:	0:	Y	3
HD 005394	3	1	A,B	1800:	2070:	6.5:	N	4
			Aa,Ab	0.557	8.2:	3.5 – 5.5	N	5,6
HD 010516	2	1	A,B	0.347	4.9	3.1	Y	7
HD 022192	1	1	...	...	...	...	N	8
HD 023630	1	1	...	...	...	...	N	4
HD 023862	3	9	Aa,Ab	35:	150:	2.1:	Y	10
			Aa1,Aa2	0.597	8.8	1.0 – 5.0	Y	11
HD 025940	1	...	...	...	...	...	N	8
HD 037202	2	1	A,B	0.364	7.7	2.7 – 4.5	N	12
HD 058715	1	1	...	...	...	...	N	1
HD 109387	2	...	A,B	0.169	3.3	1.4 – 3.1	N	13
HD 138749	2	14	A,B	161:	582:	1.8	Y	15
HD 142926	2	1	A,B	0.126	2.7	1.0 – 2.5	N	16
HD 142983	1	...	...	...	...	...	N	17
HD 148184	2	...	A,B	0.0934	3.1	3.8 – 5.9	N	18
HD 164284	2	14	A,B	43:	103:	2.1	Y	19
HD 166014	2	14	...	...	...	2.5	Y	3
HD 198183	3	14	A,B	461	770	1.2	Y	20
			Aa,Ab	11.63	49	0.7:	Y	21
HD 200120	3	14	Aa,Ab	161:	208:	2.6	Y	22
			Aa1,Aa2	0.077	1.1	2.8 – 4.7	Y	23
HD 202904	1	1	...	...	...	...	N	24
HD 203467	1	...	...	...	...	...	N	25
HD 209409	1	1	...	...	...	...	N	26
HD 212076	1	1	...	...	...	...	N	27
HD 217675	4	14	A,B	117.4	295	2.2	Y	28
			Aa,Ab	5.6	61	2.1	Y	28
			Ba,Bb	0.090	1.9	0.0	Y	28
HD 217891	1	1	...	...	...	...	N	29

References. — 1. Mason et al. (1997); 2. Koubský et al. (2010); 3. Grundstrom (2007); 4. Roberts et al. (2007); 5. Harmanec et al. (2000); 6. Miroshnichenko et al. (2002); 7. Gies et al. (2007); 8. Delaa et al. (2011); 9. Mason et al. (1993); 10. Luthardt & Menchenkova (1994); 11. Nemravová et al. (2010); 12. Ruždjak et al. (2009); 13. Saad et al. (2005); 14. Mason et al. (2009); 15. Fabricius & Makarov (2000); 16. Koubský et al. (1997); 17. Rivinius et al. (2006); 18. Harmanec (1987); 19. Tokovinin et al. (2010); 20. Starikova (1982); 21. Balega & Balega (1988); 22. B. D. Mason, priv. communication; 23. Maintz et al. (2005); 24. Neiner et al. (2005); 25. Koubský et al. (2003); 26. Oudmaijer & Parr (2010); 27. Rivinius et al. (2003); 28. Zhuchkov et al. (2010); 29. Dachs et al. (1986).

Table 5. Adopted Binary Orbital Elements

HD Number	$P$ (d)	$e$	$T$ (HJD)	$\omega$ (deg)	$a$ (mas)	$i$ (deg)	$\Omega$ (deg)	$\Delta K_{\text{obs}}$ (mag)	Ref.
HD 004180	1031.550	0.00	2452792.200	180.0	17.00	115.0	267	2.6	Koubský et al. (2010)
HD 010516	126.673	0.00	2450091.770	180.0	4.90	72.5	117	3.1	Gies et al. (1998)
HD 023862	12615.000	0.90	2453629.000	115.0	150.47	138.0	357	2.1	This work
HD 138749	73048.440	0.50	2433000.000	30.0	581.61	98.0	21	1.8	This work
HD 164284	9861.539	0.40	2451150.000	165.0	103.23	52.0	180	2.1	This work
HD 198183	4272.603	0.52	2444797.000	253.5	48.70	135.1	119	0.7	Baize (1993), this work
HD 198183	168559.275	0.35	2378057.800	322.0	770.00	146.3	144	1.2	Baize (1983)
HD 200120	58973.320	0.26	2460416.414	265.5	207.60	145.8	205	2.6	B. Mason, priv. comm.
HD 217675	2059.966	0.22	2452859.405	55.0	61.00	152.0	318	2.1	Zhuchkov et al. (2010)
HD 217675	42879.434	0.37	2455050.859	144.2	295.00	109.6	7	2.2	Zhuchkov et al. (2010)

Table 6. SED fits of Be Stars

HD Number	$E(B - V)$ (mag)	$\delta E(B - V)$ (mag)	$\theta_s$ (mas)	$\delta\theta_s$ (mas)	$E^*(UV - K)$ (mag)	$\delta E^*(UV - K)$ (mag)	$c_p$	$\delta c_p$
HD 004180	0.118	0.008	0.333	0.009	0.070	0.016	0.938	0.014
HD 005394	0.096	0.008	0.446	0.012	1.442	0.230	0.265	0.057
HD 010516	0.162	0.010	0.235	0.008	0.936	0.283	0.422	0.111
HD 022192	0.099	0.008	0.307	0.008	0.533	0.264	0.612	0.150
HD 023630	0.014	0.008	0.638	0.019	0.662	0.234	0.544	0.118
HD 023862	0.017	0.008	0.229	0.006	0.547	0.023	0.604	0.013
HD 025940	0.104	0.008	0.329	0.009	0.671	0.312	0.539	0.157
HD 037202	0.044	0.009	0.445	0.015	0.785	0.280	0.485	0.127
HD 058715	0.001	0.008	0.664	0.020	0.175	0.264	0.851	0.209
HD 109387	0.022	0.008	0.385	0.011	0.435	0.036	0.670	0.022
HD 138749	0.000	0.008	0.296	0.008	0.198	0.019	0.833	0.014
HD 142926	0.012	0.008	0.183	0.005	0.202	0.015	0.830	0.011
HD 142983	0.000	0.007	0.172	0.004	1.329	0.020	0.294	0.005
HD 148184	0.354	0.010	0.201	0.007	2.008	0.280	0.157	0.041
HD 164284	0.089	0.008	0.179	0.005	0.328	0.027	0.739	0.018
HD 166014	0.000	0.007	0.521	0.013	0.066	0.354	0.941	0.312
HD 198183	0.000	0.007	0.199	0.005	0.314	0.029	0.749	0.020
HD 200120	0.000	0.007	0.149	0.004	1.446	0.348	0.264	0.086
HD 202904	0.113	0.008	0.295	0.009	0.053	0.404	0.952	0.363
HD 203467	0.156	0.010	0.197	0.007	0.948	0.031	0.418	0.012
HD 209409	0.015	0.008	0.268	0.007	0.472	0.016	0.647	0.010
HD 212076	0.059	0.008	0.189	0.005	0.782	0.017	0.487	0.008
HD 217675	0.046	0.008	0.396	0.010	0.003	0.458	0.997	0.443
HD 217891	0.001	0.008	0.259	0.008	0.330	0.020	0.738	0.014



Table 7. Gaussian Elliptical Fits of the Interferometric Visibilities

HD Number (1)	$r$ (2)	$\delta r^a$ (3)	$PA$ (deg) (4)	$\delta PA^a$ (deg) (5)	$c_p$ (6)	$\delta c_p^a$ (7)	$\theta_{\text{maj}}$ (mas) (8)	$\delta\theta_{\text{maj}}$ (mas) (9)	$\chi^2_\nu$ (10)	$c_p(\text{corr})$ (11)	$\delta c_p(\text{corr})$ (12)	$R_d/R_s$ (13)	$\delta R_d/R_s$ (14)	Res. (15)
HD 004180	0.583	0.101	101.4	13.8	0.500	0.000	1.027	0.173	3.03	0.558	0.019	3.243	0.493	Y
HD 005394	0.722	0.038	38.2	5.0	0.082	0.036	1.236	0.063	15.63	0.190	0.032	2.946	0.134	Y
HD 010516	0.100	0.000	135.5	3.5	0.682	0.017	2.441	0.198	8.18	0.700	0.016	10.437	0.838	Y
HD 022192	0.251	0.562	136.8	4.5	0.518	0.000	1.030	0.264	1.50	0.612	0.090	3.502	0.898	Y
HD 023630	1.000	0.000	00.0	0.0	0.448	0.297	0.091	0.000	5.85	1.000	0.000	1.010	0.000	N
HD 023862	0.438	0.000	159.0	0.0	0.500	0.000	0.364	0.220	3.33	0.715	0.057	1.879	2.315	M
HD 025940	0.866	0.000	108.0	0.0	0.412	0.000	0.597	0.245	2.55	0.539	0.009	2.072	0.676	Y
HD 037202	0.148	0.027	125.4	1.3	0.422	0.016	1.790	0.073	4.30	0.534	0.013	4.146	0.159	Y
HD 058715	0.783	0.000	139.5	0.0	0.717	0.000	0.777	0.181	2.77	0.851	0.132	1.539	0.194	Y
HD 109387	1.000	0.000	0.0	0.0	0.803	0.025	3.214	0.749	6.36	0.805	0.025	8.407	1.932	Y
HD 138749	0.200	0.000	177.0	0.0	0.500	0.000	0.261	0.177	2.06	0.907	0.056	1.332	0.470	N
HD 142926	0.270	0.082	98.4	5.7	0.822	0.000	1.329	0.714	0.51	0.830	0.005	7.330	3.824	M
HD 142983	0.405	0.000	50.0	0.0	0.242	0.000	0.836	0.164	0.75	0.294	0.005	4.963	0.936	Y
HD 148184	0.947	0.000	20.0	0.0	0.123	0.000	0.858	0.142	1.59	0.157	0.004	4.385	0.690	Y
HD 164284	0.685	0.000	18.0	0.0	0.728	0.000	0.892	0.187	2.92	0.739	0.005	5.082	1.025	M
HD 166014	0.435	0.279	67.8	32.5	0.250	0.000	0.337	0.105	1.88	0.941	0.069	1.191	0.108	M
HD 198183	0.826	0.000	30.0	0.0	0.133	0.000	0.163	0.198	4.91	0.749	0.177	1.292	0.779	N
HD 200120	0.310	0.000	95.0	0.0	0.143	0.000	0.554	0.190	4.67	0.264	0.023	3.852	1.219	M
HD 202904	0.258	0.129	108.8	2.9	0.541	0.370	1.211	0.786	1.75	0.604	0.319	4.225	2.544	Y
HD 203467	0.799	0.000	76.0	0.0	0.343	0.000	0.528	0.087	1.62	0.418	0.006	2.861	0.415	Y
HD 209409	0.249	0.059	107.5	2.2	0.617	0.000	1.525	0.642	1.80	0.647	0.006	5.776	2.374	Y
HD 212076	0.955	0.000	148.0	0.0	0.308	0.000	0.295	0.044	1.61	0.487	0.032	1.852	0.202	M
HD 217675	0.022	0.000	25.0	0.0	0.340	0.195	0.056	0.000	2.23	1.000	0.000	1.010	0.000	N
HD 217891	0.702	0.150	30.6	17.1	0.692	0.309	0.804	0.593	1.81	0.722	0.279	3.261	2.098	Y

<sup>a</sup>Uncertainty of zero indicates cases where the model parameter was fixed in advance of the fit.

Table 8. Other Interferometric Results

HD Number (1)	$r$ (2)	$\delta r$ (3)	$PA$ (deg) (4)	$\delta PA$ (deg) (5)	$\theta_{\text{maj}}$ (mas) (6)	$\delta\theta_{\text{maj}}$ (mas) (7)	Band (8)	Ref. (9)
HD 004180	1.00	...	...	...	1.90	0.10	H $\alpha$	1
HD 005394	0.70	0.02	19	2	3.47	0.02	H $\alpha$	2
HD 005394	0.58	0.03	31	1	3.59	0.04	H $\alpha$	3
HD 005394	0.74	0.05	19	5	0.76	0.05	$R$	4
HD 005394	0.75	0.05	12	9	0.82	0.08	$H$	4
HD 010516	0.46	0.04	118	5	2.67	0.20	H $\alpha$	2
HD 010516	0.27	0.01	119	1	2.89	0.09	H $\alpha$	3
HD 022192	0.47	0.11	147	11	3.26	0.23	H $\alpha$	2
HD 022192	0.34	0.10	96	2	4.00	0.20	H $\alpha$	5
HD 022192	< 0.61	...	158	10	111.00	16.00	15 GHz	6
HD 023630	0.95	0.22	19	...	2.65	0.14	H $\alpha$	2
HD 023630	0.75	0.05	45	9	2.08	0.18	H $\alpha$	7
HD 025940	0.89	0.13	68	...	2.77	0.56	H $\alpha$	2
HD 025940	0.77	0.10	115	33	2.10	0.20	H $\alpha$	5
HD 037202	0.28	0.02	122	4	4.53	0.52	H $\alpha$	2
HD 037202	0.31	0.07	118	4	3.14	0.21	H $\alpha$	8
HD 037202	0.24	0.14	123	6	1.57	0.28	$H$	9
HD 037202	...	...	126	2	...	...	Br $\gamma$	10
HD 058715	...	...	...	...	2.65	0.10	H $\alpha$	2
HD 058715	0.69	0.15	40	30	2.13	0.50	H $\alpha$	7
HD 058715	0.76	0.10	140	6	0.33	0.18	$H$	10
HD 109387	1.00	...	...	...	2.00	0.30	H $\alpha$	11
HD 142983	0.60	0.11	50	9	1.72	0.20	$H$	12
HD 142983	...	...	50	...	1.65	0.05	$K$	13
HD 148184	1.00	...	...	...	3.46	0.07	H $\alpha$	14
HD 202904	1.00	...	...	...	1.00	0.20	H $\alpha$	11
HD 217891	1.00	...	...	...	2.40	0.20	H $\alpha$	11

References. — 1. Koubský et al. (2010); 2. Quirrenbach et al. (1997); 3. Tycner et al. (2006); 4. Stee et al. (2012); 5. Delaa et al. (2011); 6. Dougherty & Taylor (1992); 7. Tycner et al. (2005); 8. Tycner et al. (2004); 9. Schaefer et al. (2010); 10. Kraus et al. (2012); 11. C. Tycner, priv. communication; 12. Štefl et al. (2012); 13. Pott et al. (2010); 14. Tycner et al. (2008).

Table 9. Linear Rotational and Critical Velocities

HD Number	$V \sin i$ (km s <sup>-1</sup> )	$V_{\text{crit}}$ (km s <sup>-1</sup> )	$V_{\text{rot}}$ (km s <sup>-1</sup> )	$V_{\text{rot}}/V_{\text{crit}}$	$\Omega_{\text{rot}}/\Omega_{\text{crit}}$
HD 004180	208±13	332±21	249±26	0.75±0.09	0.91±0.06
HD 005394	441±27	577±36	599±37	1.04±0.09	≈ 1
HD 010516	462±33	590±42	487± 6	0.82±0.06	0.96±0.03
HD 022192	295±15	397±20	310±70	0.78±0.18	0.93±0.11
HD 023630	149± 8	274±15	216±20	0.79±0.09	0.94±0.05
HD 025940	220±13	386±21	323±82	0.84±0.22	0.96±0.10
HD 037202	326± 7	466±13	333± 6	0.71±0.02	0.89±0.02
HD 058715	231±14	380±24	327±91	0.86±0.25	0.97±0.10
HD 142983	407±22	501±28	484±56	0.97±0.12	1.00±0.01
HD 202904	167±20	468±30	171± 7	0.37±0.03	0.52±0.04
HD 209409	282±20	391±27	288± 4	0.74±0.05	0.90±0.04
HD 217891	100± 6	367±24	135±44	0.37±0.12	0.53±0.16